POLYMER-MEDIATED ASSEMBLY OF MRI CONTRAST AGENTS AND THEIR USE IN IMAGING OF VASCULAR DEFECTS

BY

CARTNEY EATON SMITH

DISSERTATION

Submitted in partial fulfillment of the requirements
for the degree of Doctor of Philosophy in Chemical Engineering
in the Graduate College of the
University of Illinois at Urbana-Champaign, 2015

Urbana, Illinois

Doctoral Committee:

Associate Professor Hyunjoon Kong, Chair
Associate Professor Mary L. Kraft
Professor Hong Yang
Professor Steven C. Zimmerman

ABSTRACT

Defective, leaky vasculature is characteristic of a wide variety of diseases, including arthritis, cancer, and cardiovascular disease. The ability to locally highlight vascular defects via medical imaging may therefore provide a way to improve diagnosis and treatment of some of the most significant diseases worldwide. As magnetic resonance imaging (MRI) provides the highest spatial resolution and best soft tissue contrast among common imaging techniques, it remains an appealing approach to vascular imaging. MRI, however, has relatively low sensitivity to its contrast agents compared to other clinical modalities, which limits its use in targeted applications. To address this issue, this thesis investigates the use of polymer materials to control the size, morphology, spatial organization, and surface properties of MR imaging probes to improve their relaxivity and accumulation at sites of interest.

The first part of this thesis focuses on the design and development of gadolinium-based contrast agents. Chapter 2 describes the synthesis of a polymeric fastener to anchor gadolinium to the surface of a liposome through electrostatic and hydrophobic interactions. As a result, the probe provided greater contrast per dose than gadolinium chelates used clinically, and was able to beacon areas of vascular damage in *in vivo* models of ischemia. The strategy was then adapted to rapidly label stem cells for applications in cell tracking, as described in Chapter 3.

Secondly, methods to improve the *in vivo* performance of superparamagnetic iron oxide nanoparticle (SPION) contrast agents are investigated. Chapter 4 explores the use of hyperbranched polyglycerol (HPG) in assembling SPIONs in the form of spherical clusters. By controlling the cluster size and molecular architecture of the polymer coating, optimal relaxivity of the SPIONs was achieved for sensitive imaging. In Chapter 5, the SPION clusters are further improved with the incorporation of targeting ligands and by inducing a wormlike morphology.

This allowed for greater accumulation in areas of defective vasculature. Overall, this work contributes to a better understanding of contrast agent design and may serve to expedite efforts to improve the diagnosis and treatment of vascular diseases.

ACKNOWLEDGMENTS

First of all, I would like to thank my research advisor, Professor Hyunjoon Kong, for his encouragement and guidance throughout these past years, for supporting my curiosity, and for giving me the freedom to explore. I would also like to thank the members of the Kong Lab for their numerous contributions to this work and for the many insightful conversations. And thank you to the Zimmerman Lab, particularly Dr. Dawn Ernenwein, Brenda Andrade, and JuYeon Lee, for their significant contributions and collaboration on the polyglycerol projects. Those who made possible the animal experiments for this thesis also deserve special recognition: Dr. Artem Shkumatov, Dr. Molly Melhem, Professor Edward Roy, as well as Dr. Sanjay Misra and his group at Mayo Clinic. I would additionally like to extend my gratitude to Dr. Boris Odintsov, Dr. Ryan Larsen, and the Biomedical Imaging Center at the Beckman Institute for Advanced Science and Technology for their enthusiasm and expertise in MRI. I am also very grateful for the input and thoughtful suggestions from my committee members: Professor Steven Zimmerman, Professor Mary Kraft, and Professor Hong Yang.

I would also like to thank my family— Colby, Kathy, and Mikaela— and all of my friends, teachers, mentors, and Jet who encouraged me to work hard, pursue my passions, and take time to play. And I would especially like to thank Jess, who gave me the courage to go back to school and the strength to complete it.

The work described herein was made possible by funding from the National Institutes of Health Grant 1R01 HL109192, and Chemistry-Biology Interface Training Grant 5T32-GM070421, which I am honored to have been a part of.

TABLE OF CONTENTS

CHAPTER 1

INTRODUCTION

1.1 Cardiovascular Disease

According to the World Health Organization, cardiovascular disease (CVD) remains the leading cause of death worldwide. With aging populations, as well as increasing rates of risk factors such as obesity and air pollution levels, CVD will continue to represent a great challenge to human health. Furthermore, as CVD refers to the dysfunction of the heart or any of the numerous blood vessels throughout the body, it can manifest itself in a variety of ways, including stroke, aneurysm, myocardial infarction, chronic kidney disease, and limb ischemia. Most commonly, CVD develops from atherosclerosis, in which plaque builds up on arterial walls to restrict the flow of blood through the vessel.

An inflammatory process,[1,2] atherosclerosis is initiated by damage to the endothelial lining of a blood vessel, for example as a result of smoking, hypertension, or high levels of low-density lipoproteins (LDL). This induces inflammation, in which endothelial cells upregulate the expression of cellular adhesion molecules to bind leukocytes within the blood stream,[3] concomitant with increased vascular permeability as a result of the loss of endothelial tight junctions.[4,5] Plaque, consisting of cholesterol, lipids, dead cells, and calcified materials, then begins to build up below the endothelium. Given sufficient progression, the plaque can eventually reach a critical size at which point blood flow through the artery is significantly reduced. The effect is further exacerbated with the potential formation of a thrombus, which can ultimately occlude the blood vessel. Such blockage results in tissue ischemia, necrosis, and eventually loss of organ function and death. As such, it is of great importance to diagnose atherosclerotic conditions early during disease progression. Beyond the cost of human life, by most recent estimates the United States has spent over $300 billion in a single year on the treatment and diagnosis of cardiovascular disease.[6] There are therefore great needs to improve current methods of diagnosis and treatment of CVD.

Commonly used clinical diagnostic methods of CVD are generally limited to late stages of disease progression, or do not provide spatially localized diagnostic information.[7] For example, analysis of a patient's blood for certain factors may indicate whether the patient is at risk of suffering a cardiovascular event,[8] or may be able to indicate whether the patient has experienced a heart attack, but likely would not be able to pinpoint areas of vascular dysfunction. To visualize perfusion of blood through arteries, catheter angiography has been the gold standard. In recent years, computed tomography (CT) angiography has also emerged as a non-invasive alternative that also allows for assessment of arterial calcification. However, while advantageous in locating areas of vascular occlusion, such techniques are limited to arteries already displaying significant stenosis or late stage calcification.

A promising strategy to interrogate the status of damaged vasculature is to use targeted or bioresponsive contrast agents to locally highlight areas of interest. For example, magnetic resonance imaging (MRI) contrast agents can be modified to adhere to thrombi or atherosclerotic plaques in order to locally assess the molecular status of the disease, as well as determine whether the plaque is stable or prone to rupture.[9,10] Others have created MRI contrast agents that respond to the oxidative stress present in atherosclerotic lesions.[11] To probe the inflammatory state, such probes can be targeted to inflamed endothelial cells[12] or the macrophages present at sites of inflammation.[13,14] MRI in particular is being investigated for its use in MR angiography[15] due to its superior resolution and soft tissue contrast among other clinical imaging modalities.[16] Its limitless penetration depth and non-ionizing radiation also make it an attractive choice for the application. MRI, however, is marked by its low sensitivity to its imaging probes, necessitating high levels of accumulation at a target site in order to see any contrast effect.[17] Therefore, contrast agent formulation strategies that enhance sensitivity, as well as accumulation during early stages of inflammation, remain a promising area of investigation. Furthermore, as the leaky blood vessels characteristic of vascular inflammation are a hallmark of various other diseases, including chronic lung injuries,[18] rheumatoid arthritis,[19] and cancer,[20] such a probe could be broadly applicable in a wide range diagnostic applications.

1.2 Magnetic Resonance Imaging and Its Contrast Agents

MRI operates on principles of nuclear relaxation. In the presence of an externally applied magnetic field, unpaired nuclear spins produce a net alignment. Due to the abundance of hydrogen in the human body, most commonly in the form of water, its alignment and relaxation are the focus of most clinical MRI exams. In a typical MR sequence, an applied radio frequency (RF) pulse flips the proton alignment 90° or 180° out of plane with the magnetic field. Subsequent proton realignment after removal of the RF pulse produces signal, which is the basis for image generation. This longitudinal relaxation is termed a T_1 relaxation process (Figure 1.1a). Simultaneously, the proton undergoes precession about its axis. Initially, upon excitation with the RF pulse, the proton precessional rates are aligned. However, as they relax to their equilibrium state, the protons dephase as a result of local field inhomogeneities in what is termed T_2 relaxation (Figure 1.1b). Since T_1 and T_2 relaxation rates depend on the local tissue environment, MRI can be used to visually distinguish anatomical features in a scan. Additionally, to highlight particular areas of interest by enhancing or diminishing MR signal, contrast media that affects the relaxation of water protons can be used.

It is estimated that approximately 35% of all MR scans employ contrast media.[21] These take the form of either positive, T_1 contrast agents, or negative, T_2 contrast agents. The former is typically based on chelated gadolinium (Gd) complexes, as gadolinium is highly paramagnetic due to its seven unpaired electrons. This allows gadolinium to readily interact with water through a metal coordination bond that effectively reduces the T_1 relaxation time of the water protons (Figure 1.2a). This type of interaction, known as the inner sphere, represents the primary mode of gadolinium interaction with water to enhance the relaxation rate. Other, weaker, interactions arise from water hydrogen bonded to the chelate, termed second sphere coordination, or water experiencing the paramagnetic effects of gadolinium without coordination in what is termed the outer sphere.[22]

In the design of gadolinium-based contrast agents, recent efforts have focused on methods to enhance signal in areas of interest by improving targetability and molar relaxivity. For example, gadolinium chelates have been conjugated to polymer backbones or incorporated with nanoparticles containing binding motifs such as peptides, antibodies, or folic acid to bring gadolinium to tissues of interest.[23-26] In many such cases, the relaxivity is also increased due to the lengthening of the rotational correlation time upon conjugating the gadolinium chelate to a high molecular weight species, thus enhancing the time over which gadolinium interacts with a given water molecule.[27] Others have also focused on methods of changing relaxivity in the presence of stimuli, such as pH, calcium levels, or enzymatic activity, to probe the local tissue environment.[28-30] Overall, a common theme in the design of gadolinium probes for alteration of relaxivity is to develop ways of controlling the interaction with surrounding water, and this remains an active area of research.

The most commonly used T_2 contrast agents are superparamagnetic iron oxide nanoparticles (SPIONs), which consist of a metallic core and a hydrophilic coating that imparts biocompatibility and colloidal stability. Unlike gadolinium-based contrast agents that rely on direct coordination with water as the primary means of relaxation, SPIONs produce stronger paramagnetic effects to locally perturb the magnetic field (Figure 1.2b). This results in loss of signal as the protons' precessional motion quickly becomes dephased.

Due to their size, SPIONs lend themselves well to passive targeting of leaky vasculature through the enhanced permeability and retention (EPR) effect.[31-33] Additionally, SPIONs can be functionalized with active targeting moieties, either by direct surface conjugation through ligand exchange or by encapsulation with an adsorbing material.[34] As with gadolinium chelates, MRI is known to have low sensitivity to SPION contrast agents. Therefore relaxivity enhancement is an area of great interest. Current approaches focus on accomplishing this by controlling size,[35] composition,[36] or morphology[37,38] of the nanoparticles to heighten their saturation magnetization. Additionally, relaxivity can be enhanced by organizing SPIONs into controlled aggregate clusters.[39-41] This provides the basis for methods of stimulus-responsive contrast enhancement. For example, SPIONs have been functionalized to assemble in the presence of matrix metalloproteinase-2 (MMP-2)[42] or calcium ions[43] such that relaxivity is greatly enhanced in the presence of the analyte. In all cases, the behavior and performance of the SPION formulations with regards to relaxivity, targetability, and responsiveness is intrinsically related to the design of the nanoparticle coating material.

1.3 Project Overview

This thesis seeks to improve the diagnostic capability of commonly used MRI contrast agents and leverage them in the localized evaluation of vascular defects characteristic of cardiovascular disease. To do so, polymer systems are employed to control the size, morphology, spatial organization, and water accessibility of gadolinium and SPION nanocarriers to enhance both relaxivity and targetability. Chapter 2 introduces a strategy to coat nano- and microparticles post fabrication with chelated gadolinium using a polymeric fastener to augment the interaction between gadolinium and bulk water. This material is adopted in Chapter 3 as a cellular coating to efficiently label stem cells commonly used in cellular therapies for cardiovascular disease. Chapter 4 investigates the role of polymer molecular architecture in relaxivity optimization of controlled SPION clusters for sensitive imaging of tissue ischemia. Chapter 5 then explores the morphogenic properties of the SPION coating material to induce wormlike assemblies of SPION clusters for improved active targeting of inflammation. Overall, the results of this work will be broadly useful in nanocarrier design and will serve to elevate the diagnostic capability of MRI in the evaluation of CVD and other inflammatory diseases.

1.4 Figures

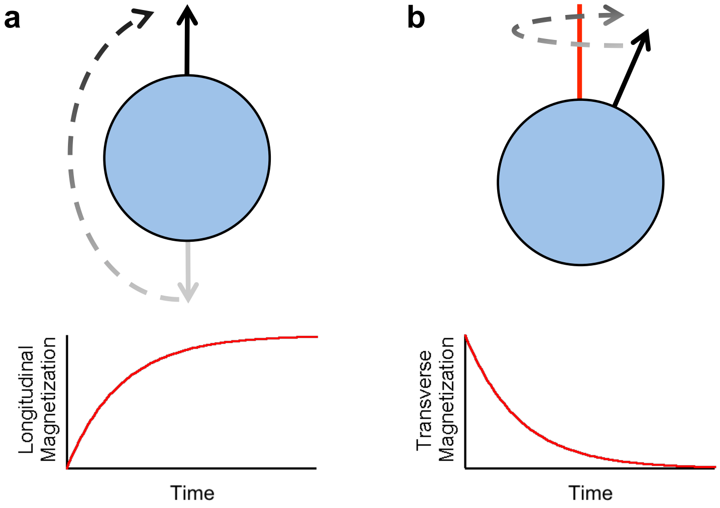

Figure 1.1 Nuclear relaxation processes. (a) T_1 longitudinal relaxation, in which the orientation of the nuclear spin returns to equilibrium orientation in a magnetic field after removal of an RF pulse. (b) T_2 transverse relaxation, in which the precession of the nuclear spins become dephased after an initial perturbation by an RF pulse.

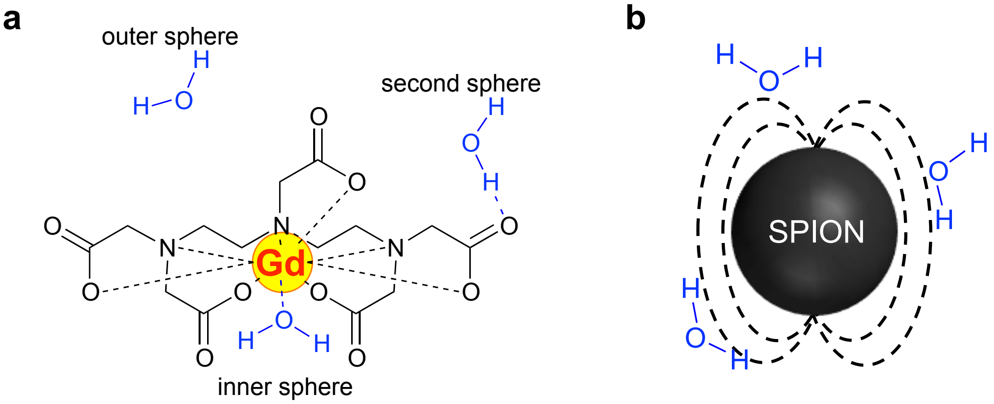

Figure 1.2 Commonly used MRI contrast agents. (a) Chelated gadolinium, a T_1 contrast agent, interacts primarily with water through direct coordination in the inner sphere. To a lesser extent, water experiences the relaxive properties of gadolinium in the second coordination sphere and outer sphere. (b) SPIONs, a class of T_2 contrast agent, affect the relaxation rates of water protons through paramagnetic interactions. Images are not drawn to scale.

1.5 References

1. Ross, R. Atherosclerosis — an Inflammatory Disease. *New Engl. J. Med.* **1999,** *340*, 115-126.

2. Libby, P.; Ridker, P. M.; Maseri, A. Inflammation and Atherosclerosis. *Circulation* **2002,** *105*, 1135-1143.

3. Ley, K.; Laudanna, C.; Cybulsky, M. I.; Nourshargh, S. Getting to the Site of Inflammation: The Leukocyte Adhesion Cascade Updated. *Nat. Rev. Immunol.* **2007,** *7*, 678-689.

4. Dejana, E.; Orsenigo, F.; Lampugnani, M. G. The Role of Adherens Junctions and VE-Cadherin in the Control of Vascular Permeability. *J. Cell Sci.* **2008,** *121*, 2115-2122.

5. Weis, S. M. Vascular Permeability in Cardiovascular Disease and Cancer. *Curr. Opin. Hematol.* **2008,** *15*, 243-9.

6. Mozaffarian, D.; Benjamin, E. J.; Go, A. S.; Arnett, D. K.; Blaha, M. J.; Cushman, M.; de Ferranti, S.; Després, J.-P.; Fullerton, H. J.; Howard, V. J.*, et al.* Heart Disease and Stroke Statistics—2015 Update: A Report from the American Heart Association. *Circulation* **2015,** *131*, e29-e322.

7. Sanz, J.; Fayad, Z. A. Imaging of Atherosclerotic Cardiovascular Disease. *Nature* **2008,** *451*, 953-957.

8. Ridker, P. M. High-Sensitivity C-Reactive Protein: Potential Adjunct for Global Risk Assessment in the Primary Prevention of Cardiovascular Disease. *Circulation* **2001,** *103*, 1813-1818.

9. Peters, D.; Kastantin, M.; Kotamraju, V. R.; Karmali, P. P.; Gujraty, K.; Tirrell, M.; Ruoslahti, E. Targeting Atherosclerosis by Using Modular, Multifunctional Micelles. *Proc. Natl. Acad. Sci.* **2009,** *106*, 9815–9819.

10. Chung, E. J.; Mlinar, L. B.; Nord, K.; Sugimoto, M. J.; Wonder, E.; Alenghat, F. J.; Fang, Y.; Tirrell, M. Monocyte-Targeting Supramolecular Micellar Assemblies: A Molecular Diagnostic Tool for Atherosclerosis. *Adv. Healthc. Mater.* **2015,** *4*, 367-376.

11. Ronald, J. A.; Chen, J. W.; Chen, Y.; Hamilton, A. M.; Rodriguez, E.; Reynolds, F.; Hegele, R. A.; Rogers, K. A.; Querol, M.; Bogdanov, A.*, et al.* Enzyme-Sensitive Magnetic Resonance Imaging Targeting Myeloperoxidase Identifies Active Inflammation in Experimental Rabbit Atherosclerotic Plaques. *Circulation* **2009,** *120*, 592-599.

12. Nahrendorf, M.; Jaffer, F. A.; Kelly, K. A.; Sosnovik, D. E.; Aikawa, E.; Libby, P.; Weissleder, R. Noninvasive Vascular Cell Adhesion Molecule-1 Imaging Identifies Inflammatory Activation of Cells in Atherosclerosis. *Circulation* **2006,** *114*, 1504-1511.

13. Trivedi, R. A.; Mallawarachi, C.; U-King-Im, J.-M.; Graves, M. J.; Horsley, J.; Goddard, M. J.; Brown, A.; Wang, L.; Kirkpatrick, P. J.; Brown, J., *et al.* Identifying Inflamed Carotid Plaques Using In Vivo USPIO-Enhanced MR Imaging to Label Plaque Macrophages. *Atertio. Thromb. Vasc. Biol.* **2006,** *26*, 1601-1606.

14. Tu, C.; Ng, T. S.; Sohi, H. K.; Palko, H. A.; House, A.; Jacobs, R. E.; Louie, A. Y. Receptor-Targeted Iron Oxide Nanoparticles for Molecular MR Imaging of Inflamed Atherosclerotic Plaques. *Biomaterials* **2011,** *32*, 7209-16.

15. Hartung, M. P.; Grist, T. M.; François, C. J. Magnetic Resonance Angiography: Current Status and Future Directions. *J. Cardiovasc. Magn. Reson.* **2011,** *13*, 19.

16. Massoud, T. F.; Gambhir, S. S. Molecular Imaging in Living Subjects: Seeing Fundamental Biological Processes in a New Light. *Genes Dev.* **2003,** *17*, 545-580.

17. Cheon, J.; Lee, J.-H. Synergistically Integrated Nanoparticles as Multimodal Probes for Nanobiotechnology. *Acc. Chem. Res.* **2008,** *41*, 1630-1640.

18. McDonald, D. M. Angiogenesis and Remodeling of Airway Vasculature in Chronic Inflammation. *Am. J. Respir. Crit. Care Med.* **2001,** *164*, S39-S45.

19. Khan, F.; Galarraga, B.; Belch, J. J. F. The Role of Endothelial Function and Its Assessment in Rheumatoid Arthritis. *Nat. Rev. Rheumatol.* **2010,** *6*, 253-261.

20. Coussens, L. M.; Werb, Z. Inflammation and Cancer. *Nature* **2002,** *420*, 860-867.

21. Major, J. L.; Meade, T. J. Bioresponsive, Cell-Penetrating, and Multimeric MR Contrast Agents. *Acc. Chem. Res.* **2009,** *42*, 893-903.

22. Caravan, P.; Farrar, C. T.; Frullano, L.; Uppal, R. Influence of Molecular Parameters and Increasing Magnetic Field Strength on Relaxivity of Gadolinium- and Manganese-Based T1 Contrast Agents. *Contrast Media Mol. Imaging* **2009,** *4*, 89-100.

23. Cheng, Z.; Thorek, D. L. J.; Tsourkas, A. Gadolinium-Conjugated Dendrimer Nanoclusters as a Tumor-Targeted T1 Magnetic Resonance Imaging Contrast Agent. *Angew. Chem. Int. Ed.* **2010,** *49*, 346-350.

24. Winter, P. M.; Morawski, A. M.; Caruthers, S. D.; Fuhrhop, R. W.; Zhang, H.; Williams, T. A.; Allen, J. S.; Lacy, E. K.; Robertson, J. D.; Lanza, G. M., *et al.* Molecular Imaging of Angiogenesis in Early-Stage Atherosclerosis with $\alpha_v\beta_3$-Integrin—Targeted Nanoparticles. *Circulation* **2003,** *108*, 2270-2274.

25. Li, W.; Su, B.; Meng, S.; Ju, L.; Yan, L.; Ding, Y.; Song, Y.; Zhou, W.; Li, H.; Tang, L., *et al.* RGD-Targeted Paramagnetic Liposomes for Early Detection of Tumor: In Vitro and in Vivo Studies. *Eur. J. Radiol.* **2011,** *80*, 598-606.

26. Liu, Y.; Chen, Z.; Liu, C.; Yu, D.; Lu, Z.; Zhang, N. Gadolinium-Loaded Polymeric Nanoparticles Modified with Anti-VEGF as Multifunctional MRI Contrast Agents for the Diagnosis of Liver Cancer. *Biomaterials* **2011,** *32*, 5167-5176.

27. Caravan, P. Strategies for Increasing the Sensitivity of Gadolinium Based MRI Contrast Agents. *Chem. Soc. Rev.* **2006,** *35*, 512-523.

28. Santra, S.; Jativa, S. D.; Kaittanis, C.; Normand, G.; Grimm, J.; Perez, J. M. Gadolinium-Encapsulating Iron Oxide Nanoprobe as Activatable NMR/MRI Contrast Agent. *ACS Nano* **2012,** *6*, 7281-7294.

29. Mishra, A.; Fousková, P.; Angelovski, G.; Balogh, E.; Mishra, A. K.; Logothetis, N. K.; Tóth, É. Facile Synthesis and Relaxation Properties of Novel Bispolyazamacrocyclic Gd^{3+} Complexes: An Attempt Towards Calcium-Sensitive MRI Contrast Agents. *Inorg. Chem.* **2008,** *47*, 1370-1381.

30. Louie, A. Y.; Huber, M. M.; Ahrens, E. T.; Rothbacher, U.; Moats, R.; Jacobs, R. E.; Fraser, S. E.; Meade, T. J. In Vivo Visualization of Gene Expression Using Magnetic Resonance Imaging. *Nat. Biotechnol.* **2000,** *18*, 321-325.

31. Kim, J.; Kim, H. S.; Lee, N.; Kim, T.; Kim, H.; Yu, T.; Song, I. C.; Moon, W. K.; Hyeon, T. Multifunctional Uniform Nanoparticles Composed of a Magnetite Nanocrystal Core and a Mesoporous Silica Shell for Magnetic Resonance and Fluorescence Imaging and for Drug Delivery. *Angew. Chem. Int. Ed.* **2008,** *47*, 8438-8441.

32. Larsen, E. K. U.; Nielsen, T.; Wittenborn, T.; Birkedal, H.; Vorup-Jensen, T.; Jakobsen, M. H.; Østergaard, L.; Horsman, M. R.; Besenbacher, F.; Howard, K. A.*, et al.* Size-Dependent Accumulation of PEGylated Silane-Coated Magnetic Iron Oxide Nanoparticles in Murine Tumors. *ACS Nano* **2009,** *3*, 1947-1951.

33. Chertok, B.; Moffat, B. A.; David, A. E.; Yu, F.; Bergemann, C.; Ross, B. D.; Yang, V. C. Iron Oxide Nanoparticles as a Drug Delivery Vehicle for MRI Monitored Magnetic Targeting of Brain Tumors. *Biomaterials* **2008,** *29*, 487-496.

34. Duan, H.; Kuang, M.; Wang, X.; Wang, Y. A.; Mao, H.; Nie, S. Reexamining the Effects of Particle Size and Surface Chemistry on the Magnetic Properties of Iron Oxide Nanocrystals: New Insights into Spin Disorder and Proton Relaxivity. *J. Phys. Chem. C* **2008,** *112*, 8127-8131.

35. Jun, Y.-w.; Huh, Y.-M.; Choi, J.-s.; Lee, J.-H.; Song, H.-T.; KimKim; Yoon, S.; Kim, K.-S.; Shin, J.-S.; Suh, J.-S.*, et al.* Nanoscale Size Effect of Magnetic Nanocrystals and Their Utilization for Cancer Diagnosis via Magnetic Resonance Imaging. *J. Am. Chem. Soc.* **2005,** *127*, 5732-5733.

36. Jang, J.-t.; Nah, H.; Lee, J.-H.; Moon, S. H.; Kim, M. G.; Cheon, J. Critical Enhancements of MRI Contrast and Hyperthermic Effects by Dopant-Controlled Magnetic Nanoparticles. *Angew. Chem. Int. Ed.* **2009,** *48*, 1234-1238.

37. Lee, N.; Choi, Y.; Lee, Y.; Park, M.; Moon, W. K.; Choi, S. H.; Hyeon, T. Water-Dispersible Ferrimagnetic Iron Oxide Nanocubes with Extremely High R_2 Relaxivity for Highly Sensitive in Vivo MRI of Tumors. *Nano Lett.* **2012,** *12*, 3127-3131.

38. Zhao, Z.; Zhou, Z.; Bao, J.; Wang, Z.; Hu, J.; Chi, X.; Ni, K.; Wang, R.; Chen, X.; Chen, Z.*, et al.* Octapod Iron Oxide Nanoparticles as High-Performance T2 Contrast Agents for Magnetic Resonance Imaging. *Nat. Commun.* **2013,** *4*, 2266.

39. Pöselt, E.; Kloust, H.; Tromsdorf, U.; Janschel, M.; Hahn, C.; Maßlo, C.; Weller, H. Relaxivity Optimization of a PEGylated Iron-Oxide-Based Negative Magnetic Resonance Contrast Agent for T_2-Weighted Spin-Echo Imaging. *ACS Nano* **2012,** *6*, 1619-1624.

40. Paquet, C.; de Haan, H. W.; Leek, D. M.; Lin, H.-Y.; Xiang, B.; Tian, G.; Kell, A.; Simard, B. Clusters of Superparamagnetic Iron Oxide Nanoparticles Encapsulated in a Hydrogel: A Particle Architecture Generating a Synergistic Enhancement of the T_2 Relaxation. *ACS Nano* **2011,** *5*, 3104-3112.

41. Clay, N.; Baek, K.; Shkumatov, A.; Lai, M.-H.; Smith, C. E.; Rich, M.; Kong, H. Flow-Mediated Stem Cell Labeling with Superparamagnetic Iron Oxide Nanoparticle Clusters. *ACS Appl. Mater. Interfaces* **2013,** *5*, 10266-10273.

42. Harris, T. J.; von Maltzahn, G.; Derfus, A. M.; Ruoslahti, E.; Bhatia, S. N. Proteolytic Actuation of Nanoparticle Self-Assembly. *Angew. Chem. Int. Ed.* **2006,** *45*, 3161-3165.

43. Atanasijevic, T.; Shusteff, M.; Fam, P.; Jasanoff, A. Calcium-Sensitive MRI Contrast Agents Based on Superparamagnetic Iron Oxide Nanoparticles and Calmodulin. *Proc. Natl. Acad. Sci. U. S. A.* **2006,** *103*, 14707-14712.

CHAPTER 2

A POLYMERIC FASTENER CAN EASILY FUNCTIONALIZE LIPOSOME SURFACES WITH GADOLINIUM FOR ENHANCED MAGNETIC RESONANCE IMAGING

Acknowledgments

This chapter is adapted with permission from Smith, C. E.; Shkumatov, A.; Withers, S. G.; Yang, B.; Glockner, J. F.; Misra, S.; Roy, E. J.; Wong, C.-H.; Zimmerman, S. C.; Kong, H. A Polymeric Fastener Can Easily Functionalize Liposome Surfaces with Gadolinium for Enhanced Magnetic Resonance Imaging. *ACS Nano, 7*, 9599-9610. Copyright 2013 American Chemical Society. I would like to acknowledge the contributions of AS, SGW, BY, JFG, and SM for performing the animal studies, including the MR images of Figure 2.17 produced at Mayo Clinic. Additionally, EJR performed the tissue sectioning and assisted with the acquisition of the images shown in Figure 2.18, and CHW provided input into performing the ITC measurements. SCZ and HK provided scientific input and assisted in the preparation of the manuscript. I would also like to thank Boris Odintsov and Ryan Larsen at the Beckman Institute for Advanced Science and Technology for assistance with MR imaging. Finally, gadolinium content analysis was performed by the School of Chemical Sciences Microanalysis Laboratory.

2.1 Introduction

Although the clinical use of nanoparticles for the diagnosis or treatment of disease has been under development since the 1960s, a new generation of particles seeks to combine multiple functionalities within a single construct.[1-4] This strategy provides a promising way of noninvasively monitoring biodistribution of therapeutics, while simultaneously treating and tracking disease progression. Additionally, numerous imaging agents may be combined to allow for orthogonal methods of diagnosis in a single dosing.[5-7] Such a method of co-administration is often accomplished by co-encapsulation of multiple components during the fabrication of nano- or microparticles.[8-11] These encapsulation approaches, however, may influence functionality of imaging contrast agents. For example, encapsulating a magnetic resonance imaging (MRI) contrast agent into a particle's interior may limit its interaction with water in surrounding tissues and significantly reduce its relaxivity.[12] Additionally, co-encapsulation of imaging probes and drug molecules may result in undesirable interactions between the two components. Some studies have reported that contrast agents, such as gadolinium chelates, can form noncovalent associations with various proteins, which would have deleterious effects on the efficacy of biomacromolecular therapies.[13-15]

Therefore, efforts are increasingly made to localize imaging contrast agents on particle surfaces. One popular approach is chemical conjugation of micelle-forming molecules or surfactants with contrast agents or their ligands.[16-18] However, these methods may interfere with particle formation and reduce the loading efficiency of drug molecules. Other approaches have therefore focused on chemically modifying the particle surface postfabrication,[19,20] but the accompanying chemical reaction and purification steps raise concerns about the retention and bioactivity of molecules loaded within the carriers.[21] Therefore, there is still a need to exploit an advanced approach that decouples the control of particle assembly from contrast agent loading on the surface, while circumventing concerns regarding additional chemical surface modification steps.

Previously, several biological studies discovered that many biomolecules and pathogens utilize an electrostatic and hydrophobic association to stably associate with a host cell. For example, transmembrane proteins present positively charged amino acid residues and hydrophobic alkyl chains to facilitate association with lipid molecules of a cell membrane.[22-24] Additionally, various viruses associate with cell membranes through similar electrostatic and hydrophobic associations to facilitate intracellular invasion.[25-27] This study presents a strategy to harness these biological interactions in the design of carriers coated with MRI contrast agents using a polymeric fastener. A fastener is defined as a functional unit that physically joins two objects together. In this way, we propose a method to join gadolinium, an MRI contrast agent, with 1,2-dipalmitoyl-*sn*-glycero-3-phosphocholine (DPPC) liposomes as a model carrier. Chitosan conjugated with octadecyl chains and diethylenetriaminepentaacetic acid (DTPA), termed DTPA-chitosan-g-C_{18}, was synthesized as a polymeric fastener to immobilize chelated gadolinium on the liposome surface *via* electrostatic and hydrophobic assembly (Figure 2.1). We examined the role of chitosan structure in liposomal surface loading and subsequent enhancement of MRI contrast, as well as the thermodynamics of association between chitosan and liposome using isothermal titration calorimetry (ITC). Outcomes were compared to traditional methods of gadolinium loading, such as encapsulation of gadolinium into the liposome, which have been developed to enhance retention *in vivo*.[28] Overall, the results of this study enable decoupled control of particle assembly and gadolinium loading, offering considerable potential to improve bioimaging quality, as well as to advance the methods used for assembly of multifunctional nano- and microcarriers.

2.2 Results

2.2.1 Synthesis and characterization of DTPA-chitosan-g-C_{18}

Chitosan capable of binding with both liposome and gadolinium was synthesized by chemically conjugating a controlled number of hydrophobically associating octadecyl chains and gadolinium-binding DTPA to the polymer backbone. The modification of chitosan was performed through a two-step process as depicted in Figure 2.2a. First, chitosan, consisting of 95.5% deacetylated glucosamine subunits, was conjugated with octadecyl chains through the reaction between the amine groups of chitosan and carbodiimide-activated stearic acid.[29] According to the 2,4,6-trinitrobenzene sulfonic acid (TNBS) assay, the degree of substitution of octadecyl chains linked to a chitosan molecule (DS_{C18}) was varied from 0 to 2.3 to 4.2% by altering the molar ratio between stearic acid and glucosamine (see Table 2.1). The resulting alkyl-substituted chitosan, termed as chitosan-g-C_{18}, remained soluble in water at pH 4.7.

Next, the chitosan-g-C_{18}, as well as unmodified chitosan, was further conjugated with DTPA through the carbodiimide-mediated reaction between amine groups of chitosan and carboxylates of DTPA.[30] The resulting DTPA-chitosan-g-C_{18} was readily dissolved in physiologically relevant and neutral media. Chitosan coupled with DTPA successfully chelated gadolinium, as demonstrated by the retention of yellow color of xylenol orange added to the mixture of DTPA-chitosan-g-C_{18} and $GdCl_3$ (Figure 2.2b). Note that xylenol orange presents a pink color upon complexation with free gadolinium ions in solution. The active association between DTPA grafted to chitosan and gadolinium was also verified by examining the ratio of absorbance peak heights at 573 and 433 nm[31] (Figure 2.2c). In the presence of DTPA-chitosan or DTPA-chitosan-g-C_{18}, this ratio did not change as compared to the pure xylenol orange solution. However, without the chelate, there was a dramatic change in the absorbance spectrum, with a 3-

fold increase in the ratio of absorbances at 573 and 433 nm. As confirmed by the xylenol orange assay, we could tune the degree of substitution of DTPA to chitosan with the molar ratio between 1-ethyl-3-(3-dimethylaminopropyl)carbodiimide (EDC) and glucosamine unit of chitosan. In this study, the molar ratio between DTPA and EDC was kept constant at 5:1, to circumvent the potential cross-linking reaction between DTPA conjugated to the chitosan molecules. This degree of DTPA substitution was kept constant at approximately 15% for all conditions (Table 2.1).

2.2.2 Modification of the liposome surface using DTPA-chitosan-g-C_{18}

Liposomes coated with DTPA-chitosan or DTPA-chitosan-g-C_{18} were prepared by mixing premade liposomes and chitosan molecules in aqueous media. Liposomes with an average diameter of 4.6 ± 2 μm, characterized with phase contrast microscopic images, were first formed by film hydration, and then mixed with DTPA-chitosan or DTPA-chitosan-g-C_{18} with DS_{C18} varied from 2.3 to 4.2% (Figure 2.3 and Figure 2.4). The liposome surface was fully saturated with modified chitosan by mixing the two components at a 4:1 molar ratio between glucosamine unit and exposed lipid. To examine the resulting liposome-chitosan association, DTPA-chitosan and DTPA-chitosan-g-C_{18} were labeled with the amine-reactive rhodamine-B isothiocyanate (Figure 2.5). Within 10 min, the liposome showed positive red fluorescence on its surface, according to cross-sectional images captured with a confocal microscope (Figure 2.6a). The ring-like appearance of Figure 2.6a-(i) is in direct contrast to the confocal image of a liposome encapsulating fluorescent DTPA-chitosan-g-C_{18}, formed by hydration of lipids in the presence of the modified chitosan (Figure 2.6a-(ii)). This visually indicated the surface localization of the chitosan fastener on preformed liposomes. By quantitatively measuring the fluorescence intensity of liposomes after centrifugation, as well as the free chitosan in the supernatant, we found that the number of chitosan molecules bound with the liposome surface was indeed independent of DS_{C18}. These results therefore demonstrate that both DTPA-chitosan and DTPA-chitosan-g-C_{18} readily adsorb onto the liposome surface (Figure 2.6b). The chitosan associated with liposome remained stable for at least 24 h even after transfer of the liposome particles to chitosan-free phosphate buffered saline (PBS).

However, according to the thermodynamic analysis conducted using ITC, the octadecyl chains grafted to chitosan significantly augmented the association of the chitosan molecules with liposome surface (Figure 2.7). In this analysis, liposomes were formed by film hydration of DPPC lipids and titrated with solutions of DTPA-chitosan or DTPA-chitosan-g-C_{18} with varied DS_{C18}. Similar to the fluorescence assay presented in Figure 2.6b, the number of glucosamine units of chitosan bound to the liposome at saturation (*N*) was approximately equal to the number of lipids in the outer leaflet, independent of DS_{C18} (Table 2.2). In contrast, the equilibrium binding constant, *K*, increased with increasing DS_{C18}. The binding constant is defined as[32]

$$K = \frac{\Theta}{(1-\Theta)C_{free}} \tag{2.1}$$

where C_{free} is the concentration of unbound glucosamine repeat unit, and Θ is the fraction of exposed lipids bound by modified chitosan. C_{free} is further expanded and related to the total chitosan concentration and saturation binding stoichiometry, *N*:

$$C_{free} = C_{total} - N\Theta L \tag{2.2}$$

where *L* is the concentration of lipids in the outer leaflet of the liposome and assumed to be half of the total lipid concentration. Accordingly, the change in Gibbs free energy (ΔG) of the liposome-chitosan mixture, calculated from *K* using Eq. (2.3), presented negative values for all conditions.

$$\Delta G = -RT\ln\left(K\right) \tag{2.3}$$

These negative values of ΔG indicate that the association of chitosan with liposome is thermodynamically favorable. Interestingly, Δ*G* decreased linearly with DS_{C18} (Figure 2.8).

Δ*G* was further related to the additive contributions of Δ*G* for the octadecyl chain (ΔG_{C18}) and Δ*G* for other glucosamine units ($\Delta G_{glucosamine}$), through Eq. (2.4):

$$\begin{aligned}\Delta G &= DS_{C_{18}}\left(\Delta G_{C_{18}}\right)+\left(1-DS_{C_{18}}\right)\left(\Delta G_{glucosamine}\right)\\ &= \Delta G_{glucosamine}+\left(\Delta G_{C_{18}}-\Delta G_{glucosamine}\right)DS_{C_{18}}\end{aligned} \tag{2.4}$$

The ΔG_{C18} calculated from the slope and *y*-intercept of the linear regression curve in Figure 2.8 is approximately -10.8 kcal/mol. Note that the free energy for transfer of a hydrocarbon chain into a micelle or bilayer has previously been reported as approximately -0.7 kcal per mol per methylene group.[33] Therefore, it is suggested that most methylene units of the octadecyl chain grafted to chitosan are inserted into the liposome bilayer *via* hydrophobic assembly, thus further stabilizing DTPA-chitosan-g-C_{18} on the liposome surface.

Changes in enthalpy, (Δ*H*), were calculated by relating it to the total heat of the solution (*Q*) measured with ITC, as shown in Eq. (2.5)

$$Q = N\Theta V_0 L\Delta H \tag{2.5}$$

where V_0 is the total volume of the sample cell. In all cases, Δ*H* was positive, which suggests that the association between liposome and chitosan was endothermic for all conditions. This result is similar to previous studies for the association of unmodified chitosan with zwitterionic lipids.[34]

Additionally, the change in entropy (ΔS), calculated from ΔH and ΔG using Eq. (2.6) also presented positive values for all conditions.

$$\Delta S = \frac{\Delta H - \Delta G}{T} \tag{2.6}$$

Interestingly, ΔS increased with DS_{C18} of DTPA-chitosan-g-C_{18} (Table 2.2).

Taken together, we interpret that the increase in entropy is responsible for the thermodynamically favorable association between liposome and modified chitosan molecules. The positive ΔS is likely due to the release of counterions and water molecules bound with chitosan and liposome surfaces, as electrostatic interactions are established between charged chitosan subunits and exposed lipids. It is also likely that the octadecyl chains grafted to chitosan molecules confer an additional increase in ΔS with increasing DS_{C18} of DTPA-chitosan-g-C_{18} due to desolvation upon insertion into the bilayer. These different association mechanisms and thermodynamic contributions between DTPA-chitosan and DTPA-chitosan-g-C_{18} significantly influenced the amount of gadolinium loaded on the liposome surface, as will be demonstrated in the subsequent section.

2.2.3 Loading gadolinium on a liposome surface

As expected, liposomes associated with either DTPA-chitosan or DTPA-chitosan-g-C_{18} of varying DS_{C18} could immobilize gadolinium on their surfaces. In this study, coated liposome particles were mixed with $GdCl_3$ to saturate the conjugated DTPA (Figure 2.9a). Complete chelation was verified by the xylenol orange assay. Liposomes coated by DTPA-modified chitosan were able to associate with gadolinium and produce the same spectrum as pure xylenol orange solution (Figure 2.9b). Conversely, in the absence of chitosan, bare liposomes mixed with gadolinium showed a three-fold increase in the ratio of absorbances at 573 and 433 nm. These results clearly confirm that gadolinium is stably immobilized on the liposome surface through the adsorption of DTPA-chitosan or DTPA-chitosan-g-C_{18}.

Interestingly, however, the amount of gadolinium immobilized on the liposome surface was significantly dependent on whether the DTPA-chitosan was modified by octadecyl chains. According to the quantitative fluorescence assay to determine the number of rhodamine-labeled chitosan molecules remaining on the liposome surface after addition of $GdCl_3$, complexation of gadolinium with DTPA triggered 30% of the DTPA-chitosan to desorb from the liposome surface (Figure 2.9c). In contrast, DTPA-chitosan-g-C_{18} showed minimal desorption. Therefore, as a result, the gadolinium surface loading was approximately 1.4 times larger with DTPA-chitosan-g-C_{18}. These results suggest that the gadolinium bound to DTPA-chitosan destabilize the electrostatic association between chitosan molecules and liposome surface. In contrast, octadecyl chains of the DTPA-chitosan-g-C_{18}, which hydrophobically associated with alkyl chains of lipid molecules, likely act as an anchor to mitigate the tendency of gadolinium to electrostatically separate chitosan from the liposome surface.

2.2.4 Evaluation of gadolinium-loaded liposome contrast capability

The ability of gadolinium-loaded liposomes to enhance MRI contrast was evaluated using a 3 T clinical MRI scanner. MR phantom images were acquired using an inversion recovery turbo spin echo (IR-TSE) pulse sequence to evaluate spin-lattice relaxation time (T_1). Molar relaxivity was then determined by linear regression of the longitudinal relaxation rate ($R_1 = 1/T_1$) *versus* gadolinium concentration. Gadolinium loaded on the liposome modified by DTPA-chitosan-g-C_{18} significantly enhanced MR signal, compared to the liposome modified with DTPA-chitosan (Figure 2.10a). At a given liposome concentration, R_1 of the suspension was increased with DTPA-chitosan-g-C_{18}. However, the molar relaxivity of immobilized gadolinium was nearly the same across samples, regardless of DS_{C18} (Figure 2.10b and Figure 2.11). Therefore, we interpret that the enhancement of R_1 attained with DTPA-chitosan-g-C_{18} is due solely to the higher loading of gadolinium on the liposome surface, noting that 30% of the DTPA-chitosan was desorbed upon exposure to $GdCl_3$ as shown in Figure 2.9c.

Additionally, at a given gadolinium concentration, the gadolinium-loaded liposomes assembled through sequential addition of DTPA-chitosan-g-C_{18} and $GdCl_3$ to preformed vesicles enhanced MR signal more significantly than gadolinium encapsulated *in situ* during liposome formation. In the analysis shown in Figure 2.12a, the gadolinium concentration was kept constant at 70 μM for both conditions according to ICP-OES analysis. Noting that the amount of gadolinium per liposome was greater in the case of loading both in the interior and on the surface as compared to surface loading only, the number of liposomes per MR phantom sample was greater for liposomes loading gadolinium on their surfaces. Interestingly, the longitudinal relaxation rate (R_1) and the corresponding signal intensity of the phantom made with gadolinium localized on the outer leaflet were significantly greater than that made by encapsulation. This can be attributed to the greater total number of gadolinium ions anchored to the liposome surface. As such, the molar relaxivity of surface-bound gadolinium was twice that of gadolinium incorporated *via in situ* encapsulation (Figure 2.12b).

This boost in relaxivity, and subsequent MR signal enhancement, are likely derived from enhanced contact with free water in surrounding media, in contrast to the limited interaction available to gadolinium within the liposome interior. Therefore, these results systematically rationalize the necessity to load gadolinium exclusively on particle surfaces for enhancing MR images. Furthermore, the relaxivity was enhanced beyond that of the clinically used unconjugated DTPA-gadolinium complex with a molar relaxivity of 4.85 $mM^{-1}s^{-1}$ (Figure 2.11).

2.2.5 Stability analysis of gadolinium-loaded liposomes in serum-supplemented media

We further analyzed the stability of the association between DTPA-chitosan-g-C_{18} and liposome surfaces by incubating the liposome particles in media supplemented with 10% human serum at 37 °C, which is conventionally used to assess structural stability of nanoparticle formulations. Stability was monitored over the course of an hour to match the *in vivo* incubation period presented in the following sections. According to measurements of fluorescence intensity from liposomes after centrifugation to remove free chitosan molecules, more than 60% of the initially adsorbed DTPA-chitosan-g-C_{18} remained on the liposome surface (Figure 2.13). We interpret that the desorption of chitosan from liposomes may result in part from the intrinsic instability of liposome particles in circulation, as characterized by an increase in liposome permeability and structural disintegration.[35,36] We therefore propose that further optimization of the liposome itself to enhance stability in future studies would minimize the loss of DTPA-chitosan-g-C_{18} from the liposome surface. Additionally, the liposomes did not aggregate over the course of one-hour incubation according to optical images, and the average diameter changed minimally (Figure 2.14). However, there was an observable reduction in the number of liposomes following incubation in the serum-supplemented media.

Despite detachment, DTPA-chitosan-g-C_{18} was able to retain its association with gadolinium in the presence of serum. The resulting complex of gadolinium and DTPA-chitosan-g-C_{18} was minimally toxic to cells, as evaluated with an MTT assay widely used to evaluate cytotoxicity. Endothelial cells incubated with gadolinium loaded on the liposome surface, as well as those incubated with gadolinium bound to free DTPA-chitosan-g-C_{18}, retained their metabolic activity, similar to untreated cells (Figure 2.15). In contrast, half of the cells incubated with unchelated gadolinium over 24 h were no longer metabolically active.

2.2.6 In vivo performance of gadolinium-loaded liposomes

To evaluate the capability of the gadolinium-coated liposomes to highlight target tissues of interest *in vivo*, two separate animal experiments were conducted using murine models with occlusive blood flow in femoral or renal arteries. First, an ischemic injury was induced in the left hindlimb of male BALB/c mice using a suture to occlude the femoral artery.[37] Such a model is often used to study peripheral vascular diseases that result in reduced or blocked blood flow to limbs, and ultimately limb infarction if not diagnosed and treated early. These vascular defects are caused by vascular occlusion, rupture, or leakage, characteristic of atherosclerosis, vascular leak syndrome, and other cardiovascular diseases.[38,39] Through the tail vein, mice were either injected with gadolinium loaded on liposome surfaces using DTPA-chitosan-g-C_{18} (DS_{C18} = 4.2%), or with unconjugated DTPA-gadolinium, as a control. The dosage of gadolinium was kept constant at 0.04 mmol/kg.

One hour after injection, mice were imaged with a 14.1 T MR scanner to examine whether the injected liposome particles could enhance imaging of the occluded artery. Based on serum stability studies, we expected gadolinium would sufficiently remain on the liposome surfaces over the course of the experiment. In comparison to a mouse that received the ischemic injury but no injection of gadolinium, both the liposome-bound and free gadolinium chelates provided signal enhancement in the hindlimbs (Figure 2.16). However, only in the case of gadolinium loaded on the liposome surface, the occluded artery was illustrated by greater area and intensity of the highlighted region than that of the uninjured right hindlimb. We therefore suggest that the liposomes were better able to accumulate in the occluded area than free DTPA-gadolinium. In this way, the gadolinium adsorbed to the liposome surface could locally enhance the relaxation rate in the extravascular tissue and subsequently provide contrast. Such discrimination between ischemic and nonischemic limbs was not observed with the free DTPA-gadolinium, which emphasized the advantage of binding gadolinium to the liposome surface in the diagnosis of peripheral vascular diseases.

To further underscore the applicability of gadolinium-adsorbed liposomes *in vivo*, the system was administered in a rat model of renal ischemic injury. MR imaging is commonly used to diagnose renal diseases based on changes in anatomical structure, however, the use of gadolinium-based contrast agents may be limited due to lack of corticomedullary differentiation.[40] A major reason for this is the rapid transport of small gadolinium chelates from cortex to medulla during renal excretion.

First, renal arteries were clamped for 45 min to induce an ischemic state in the kidney. Saline, gadolinium in the form of free DTPA chelate, or gadolinium anchored to liposomes was injected into the left kidney through the renal artery. Five minutes after injection, kidneys displayed enhanced signal compared to the saline-injected control (Figure 2.17). However, in the case of the kidney injected with free DTPA chelate, medulla was not as readily delineated from cortex, as expected. The contrast agent appeared unevenly distributed throughout the kidney. Conversely, the gadolinium-loaded liposomes were localized within the cortex and were able to clearly differentiate cortex from medulla, as confirmed by near-infrared (NIR) fluorescence images of liposomes labeled with CellVue NIR815 dye (Figure 2.18).

2.3 Discussion

These results clearly underscore the utility of DTPA-chitosan-g-C_{18} in imbuing a liposome with MRI contrast capabilities due to (1) the higher loading of gadolinium on the liposome surface provided by hydrophobic stabilization and (2) enhanced molar relaxivity through surface localization. We envision that the contrast enhancement provided by this fabrication strategy can be further improved by modifying the chemical structure of DTPA-chitosan-g-C_{18}. For example, coating of the liposome surface with chitosan-g-C_{18} substituted with a greater amount of DTPA would significantly increase gadolinium loading on the liposome and heighten the liposome's ability to increase MR contrast.

Additionally, this process facilitates separation of secondary imaging contrast agents or drug molecules from gadolinium by incorporating them inside the liposome, so as to circumvent potential interaction between gadolinium and other functional molecules. Moreover, we propose that this process has benefits beyond MRI. For example, chitosan-g-C_{18} could be modified with peptides capable of binding with target pathological tissues. This strategy represents another way in which the efficiency of the functional unit is improved when localized on the liposome surface. Furthermore, though chitosan has been shown to demonstrate stealth properties in some cases,[41,42] the chitosan fastener may be further modified with poly(ethylene glycol) to reduce potential opsonization and enhance *in vivo* retention. Separately, the liposome composition and particle size may be optimized for the particular application. Overall, our process of coating liposomes postfabrication with the chitosan fastener should be advantageous to decoupling the particle assembly from the particle surface modification for independent tunability of functional units.

2.4 Conclusion

Overall, this study demonstrates a simple, yet unreported method to functionalize liposome surfaces with gadolinium, an MRI contrast agent, using DTPA-chitosan-g-C_{18}. Upon mixing premade liposomes with the DTPA-chitosan-g-C_{18} fastener, octadecyl chains were inserted into the lipid membrane *via* hydrophobic association, as confirmed by ITC. Subsequently, the octadecyl chains minimized desorption of chitosan molecules from the liposome triggered by chelation of gadolinium with DTPA. Therefore, liposomes loaded with gadolinium on their surfaces *via* DTPA-chitosan-g-C_{18} displayed a greater capacity to enhance MR contrast than liposomes modified by alkyl-free DTPA-chitosan. Additionally, this sequential assembly process to localize gadolinium on the exterior of the liposome greatly enhanced the molar relaxivity of gadolinium and subsequently MRI contrast, as compared to methods that incorporate gadolinium inside the liposome. Using *in vivo* models, we were also able to demonstrate the utility of the gadolinium-loaded liposomes in detecting and imaging ischemic sites. Taken together, this assembly strategy using a chitosan fastener will be broadly useful not only for functionalizing liposome surfaces with a wide array of imaging, targeting, and therapeutic modalities, and but also for spatially organizing them.

2.5 Materials and Methods

2.5.1 Synthesis of DTPA-chitosan-g-C_{18}

Chitosan (Sigma-Aldrich) was dissolved in a 50 mM aqueous HCl solution heated to 70 °C. Additional HCl was added to adjust the pH to 4.7 after chitosan was completely dissolved. Separately, varying amounts of stearic acid (Sigma-Aldrich)—2% or 5% with respect to glucosamine repeat unit of chitosan— were dissolved in ethanol at 70 °C. After dissolution of stearic acid, the solution was brought to room temperature and 1-ethyl-3- (3-dimethylaminopropyl) carbodiimide (EDC, Sigma-Aldrich) was added at a molar ratio of 5:1 EDC to stearic acid. The stearic acid/EDC solution was then added to the dissolved chitosan and reacted at 70 °C. The volume ratio between ethanol and HCl solution was kept constant at 1:2 for all conditions. After 24 h, the temperature was gradually reduced to room temperature, and the mixture continued to stir for another 24 h.

Then, ethanol was removed by precipitation in NaOH and the chitosan-g-C_{18} was resuspended in HCl. Briefly, 50 mM NaOH was added to the solution of chitosan-g-C_{18}, followed by centrifugation for 10 min at 4000 rpm. The supernatant was removed, and the precipitate was redissolved in 50 mM HCl aqueous solution at 70 °C. This precipitation/dissolution process was repeated twice to ensure removal of ethanol.

Next, diethylenetriaminepentaacetic acid (DTPA, Sigma-Aldrich) was dissolved in deionized water. Tetramethylethylenediamine (TEMED, Sigma-Aldrich) was added to the DTPA solution to adjust the pH of the mixture to 4.7. The DTPA solution was then further mixed with EDC dissolved in 50 mM HCl aqueous solution. The molar ratio between DTPA and EDC was kept constant at 5:1, to minimize cross-linking between glucosamine units of chitosan and the multiple carboxylate groups of DTPA. The DTPA/EDC mixture was finally added to the chitosan or chitosan-g-C_{18} solutions and allowed to react for 24 h at 70 °C, followed by another 24 h at room temperature. The resulting DTPA-chitosan and DTPA-chitosan-g-C_{18} were purified by dialysis (MWCO 6000-8000 regenerated cellulose tubing, Fisher Scientific) against 0.1 M NaCl for two days. The product was then further dialyzed in deionized water for one day. The purified product was then lyophilized, and kept in powder form before use.

2.5.2 Characterization of DTPA-chitosan and DTPA-chitosan-g-C_{18}

The degree of substitution of octadecyl chains to chitosan was determined by a 2,4,6-trinitrobenzene sulfonic acid (TNBS, Sigma-Aldrich) assay, which quantifies the amount of unreacted amines on chitosan. Briefly, modified chitosan samples were dissolved in an 0.1 M acetate buffer at pH 5.0 and mixed with 0.1% (w/v) TNBS at 37 °C. After incubation for 5 h, the absorbance of each mixture was measured at 335 nm with a microplate reader (Tecan Infinite 200 PRO, Tecan AG, Switzerland).

The degree of substitution of DTPA grafted to chitosan was quantified by the xylenol orange assay. A $GdCl_3$ ($GdCl_3 \bullet 6H_2O$, Sigma-Aldrich) solution was added incrementally to a solution of DTPA-chitosan or DTPA-chitosan-g-C_{18}. After each addition, an aliquot was mixed with xylenol orange tetrasodium salt (Sigma Aldrich) in acetate buffer (50 mM, pH 5.80) to determine whether any gadolinium remained unchelated, as indicated by a change in the ratio of the absorbances at 573 and 433 nm. The amount of gadolinium required to cause a change in the absorbance ratio was used to calculate the DS of DTPA.

2.5.3 Liposome preparation

Liposomes were prepared by a film hydration method followed by sonication. 1,2-Dipalmitoyl-*sn*-glycero-3-phosphocholine (Avanti Polar Lipids) was dissolved in chloroform (Fisher Scientific) and placed in a round-bottom flask. Chloroform was removed by rotary evaporation to yield an evenly distributed film. The film was then hydrated with deionized water at 50 °C, which is above the transition temperature of DPPC. The lipid concentration was kept constant at 1 mg/mL. Following hydration, liposome suspension was placed on an ice bath and sonicated for 15 min. For microscopy, liposomes were imaged with a Leica D-LUX 3 CCD camera mounted to a Leica DMIL inverted microscope (Leica Microsystems, Wetzlar, Germany). For experiments involving *in situ* encapsulation of gadolinium and DTPA-chitosan-g-C_{18} in the liposome, DTPA-chitosan-g-C_{18} was first complexed with $GdCl_3$. The lipid film, formed as described above, was then hydrated with the aqueous mixture of gadolinium and DTPA-chitosan-g-C_{18}.

2.5.4 Analysis of chitosan on the liposome surface

To quantitate the association between modified chitosans and liposomes, chitosan molecules were first labeled with rhodamine. DTPA-chitosan or DTPA-chitosan-g-C_{18} were dissolved in neutral deionized water and reacted overnight with rhodamine-B isothiocyanate (Sigma-Aldrich), in which the isothiocyanate functional moiety reacted with the primary amine groups of the chitosan backbone (Figure 2.5). Then, chitosan solutions were dialyzed against 0.1 M NaCl solution followed by deionized water to remove any unreacted rhodamine. Finally, the labeled chitosan molecules were lyophilized and kept dried until use. The rhodamine-labeled chitosans were adsorbed to preformed liposomes by stirring them together at room temperature for 10 min or 12 h, followed by centrifugation at 4000 rpm for 10 min. The supernatant, containing excess chitosan molecules, was then removed, and the pelleted liposomes were resuspended in deionized water. Concentrations of rhodamine-labeled chitosan in supernatant and resuspended liposome were analyzed by exciting the samples at 535 nm and measuring fluorescence intensity at 595 nm using a microplate reader (Tecan Infinite 200 PRO, Tecan AG, Switzerland). A standard curve was developed by serial dilution of the chitosan/liposome solution prior to centrifugation. For analysis, four replicates were prepared for each condition. Statistical significance between each sample set was determined from a two-tailed, unpaired

Student's *t* test in Microsoft Excel, in which differences were considered significant for $p < 0.05$. Additionally, chitosan adsorption onto liposomes was visualized using a laser scanning confocal microscope (LSM 700, Carl Zeiss Microimaging, GmbH, Germany).

2.5.5 Loading and analysis of gadolinium on the liposome surface

A 7.56 mM $GdCl_3$ solution was added to the aqueous suspension of liposomes modified by DTPA-chitosan or DTPA-chitosan-g-C_{18} at a 1:1 ratio of gadolinium to DTPA. Complete chelation was verified by xylenol orange assay. To quantify the amount of modified chitosan adsorbed to the liposome after gadolinium addition, fluorescently labeled DTPA-chitosan and DTPA-chitosan-g-C_{18} were used as described in the previous section. After incubation with gadolinium for 12 h, samples were centrifuged for 10 min at 4000 rpm. The concentrations of chitosan in both supernatant and resuspended liposomes were determined using the Tecan Infinite 200 PRO microplate reader as described. Again, four replicates were made per condition and analyzed for significance using a two-tailed, unpaired Student's *t* test.

2.5.6 Thermodynamic analysis of association between chitosan and liposome by isothermal titration calorimetry

Isothermal titration calorimetry (ITC) analysis was performed at 25 °C with a MicroCal VP-ITC calorimeter (MicroCal, Northampton, MA). The 1.45 mL sample cell was filled with an aqueous liposome suspension at a total lipid concentration of 0.4 mM. The cell was titrated with 28 injections of 10 μL chitosan solution (5 mM glucosamine unit concentration). Each injection was performed over 17.1 s with a delay of 300 s between injections while stirring at 310 rpm. Data analysis was performed with Origin 5.0 software from MicroCal to yield thermodynamic binding parameters such as the binding constant, change in enthalpy, and change in entropy by fitting data to a single-site binding model.[32] The first data point was not included in the analysis.

2.5.7 T_1 Relaxivity measurements

Measurements and imaging of MRI phantoms were performed with a head coil on a 3 T Siemens Magnetom Allegra MR scanner (Siemens AG, Erlangen, Germany). Images were produced with an inversion recovery turbo spin echo (IR-TSE) pulse sequence. The sequence used a repetition time (*TR*) of 2500 ms and an echo time (*TE*) of 10 ms. The inversion time (*TI*) was varied from 100 to 1700 ms to determine T_1 by nonlinear least-squares curve fitting to Eq. (2.7):

$$S(TI) = S_0[1-(1-k)e^{-TI/T_1}] \tag{2.7}$$

where $S(TI)$ is the signal intensity measured by ImageJ software, S_0 is the signal at thermal equilibrium, and k is a constant related to the flip angle and magnetization of the system.[43] Relaxation rate, R_1 was then calculated as the inverse of relaxation time ($1/T_1$).

Longitudinal relaxivity, r_1, was found by linear regression of the plot of R_1 *versus* gadolinium concentration according to Eq. (2.8):

$$1/T_1 = 1/T_{1,water} + r_1[Gd] \tag{2.8}$$

where $T_{1,\text{water}}$ is the longitudinal relaxation time of gadolinium-free media and $[Gd]$ is the total gadolinium concentration within a sample. For these measurements, gadolinium concentration was determined by inductively coupled plasma optical emission spectroscopy (ICP-OES, Perkin-Elmer Optima 2000 DV, Norwalk, CT) after digestion of samples in a concentrated nitric acid solution.

2.5.8. Serum stability of chitosan-coated liposomes

Liposomes coated with rhodamine-labeled DTPA-chitosan-g-C_{18} with DS_{C18} = 4.2% were incubated in PBS supplemented with 10% type AB human serum off the clot (PAA Laboratories Inc.) at 37 °C. At each time point, liposomes were centrifuged at 4000 rpm for 10 min and resuspended to determine the amount of modified chitosan remaining on the liposome surface by analysis of fluorescence intensity. Images of the liposomes were also captured with a Zeiss Axiovert 200M microscope (Carl Zeiss, Oberkochen, Germany).

2.5.9. MTT assay for cellular viability

C166 endothelial cells were seeded on a 96-well plate at $5\text{x}10^3$ cells per well. Cells were incubated for 24 h with unchelated gadolinium, or with gadolinium chelated by DTPA-chitosan-g-C_{18} (DS_{C18} = 4.2%) that was either adsorbed to liposomes or free in solution. In each case, gadolinium was kept at a 100 μM concentration, matching that of the highest level used for relaxivity determination of coated liposomes (blue curves in Figure 2.11). MTT reagent ((3-(4,5-dimethylthiazol-2-yl)-2,5-diphenyltetrazolium bromide, ATCC) was added to the cell culture media, and its reduction to formazan dye by metabolically active cells was evaluated by measuring absorbance at 570 nm (Tecan Infinite 200 PRO, Tecan AG, Switzerland).

2.5.10 Assessment of gadolinium-loaded liposome using a hindlimb ischemia model

The surgery to induce hindlimb ischemia was performed in accordance with the protocol approved by the Illinois Institutional Animal Care and Use Committee. The mice used were male BALB/c mice (Jackson Laboratories, ME) weighing approximately 30 g. Prior to surgery, mice were anesthetized with an intraperitoneal injection of a xylazine (10 mg/kg) and ketamine hydrochloride (100 mg/kg) cocktail. Hair was removed from the left hindlimb and a small incision was made on the upper thigh to expose the femoral artery and vein. The artery and vein were then ligated with 5-0 Ethilon sutures (Johnson & Johnson, NJ) to prevent blood flow to the limb. For mice receiving injection, 0.04 mmol/kg of gadolinium was then administered *via* tail vein.

Mice were imaged 1 h after injection with a 14.1 T Varian microimager consisting of a Unity/Inova 600 MHz NMR spectrometer (Varian, CA) equipped with a custom-made adjustable radio frequency coil.[44] T_1-weighted Coronal images of the mouse hindlimbs were acquired using a spin-echo multislice (SEMS) pulse sequence with the following parameters: slice thickness, 0.5 mm; TR, 350 ms; TE, 10 ms; matrix size, 256 × 256.

2.5.11 Evaluation of gadolinium-loaded liposome using a renal ischemia model

Procedures to induce renal ischemia were carried out according to the protocol approved by the Mayo Clinic Institutional Animal Care and Use Committee. The rats used were Sprague-Dawley rats (Jackson Laboratories, ME) weighing 300-400 g. Rats were anesthetized *via* intraperitoneal injection of xylazine (20 mg/kg) and ketamine hydrochloride (200 mg/kg). Anesthesia was maintained with intraperitoneal pentobarbital (20-40 mg/kg). An abdominal incision was then made and the renal arteries were clamped bilaterally for 45 min. Kidneys were then injected *via* the renal artery with gadolinium-DTPA, liposomes loaded with gadolinium *via* DTPA-chitosan-g-C_{18} (DS_{C18} = 4.2%), or saline. Kidneys injected with contrast agent received gadolinium doses of 0.3 μmol. Five minutes after injection, kidneys were removed for MR imaging.

Images were acquired with a 3 T Siemens MR scanner (AG, Erlangen, Germany). A three-dimensional spoiled gradient recalled (3D SPGR) sequence produced T_1-weighted images using the following parameters: slice thickness, 2 mm; *TR*, 7.3 ms; *TE*, 3.2 ms; flip angle, 15°; matrix size 352 × 224.

The coated liposomes used in this experiment were also fluorescently labeled with CellVue NIR815 dye and were formed by hydration of a lipid film with a solution of NIR815, followed by removal of unincorporated dye by centrifugation. Imaging of frozen tissue sections cut at 30 μm was performed with a LI-COR Odyssey scanner (LI-COR Biosciences, Lincoln, NE) and analyzed with 680 and 780 excitation channels.

2.6 Figures and Tables

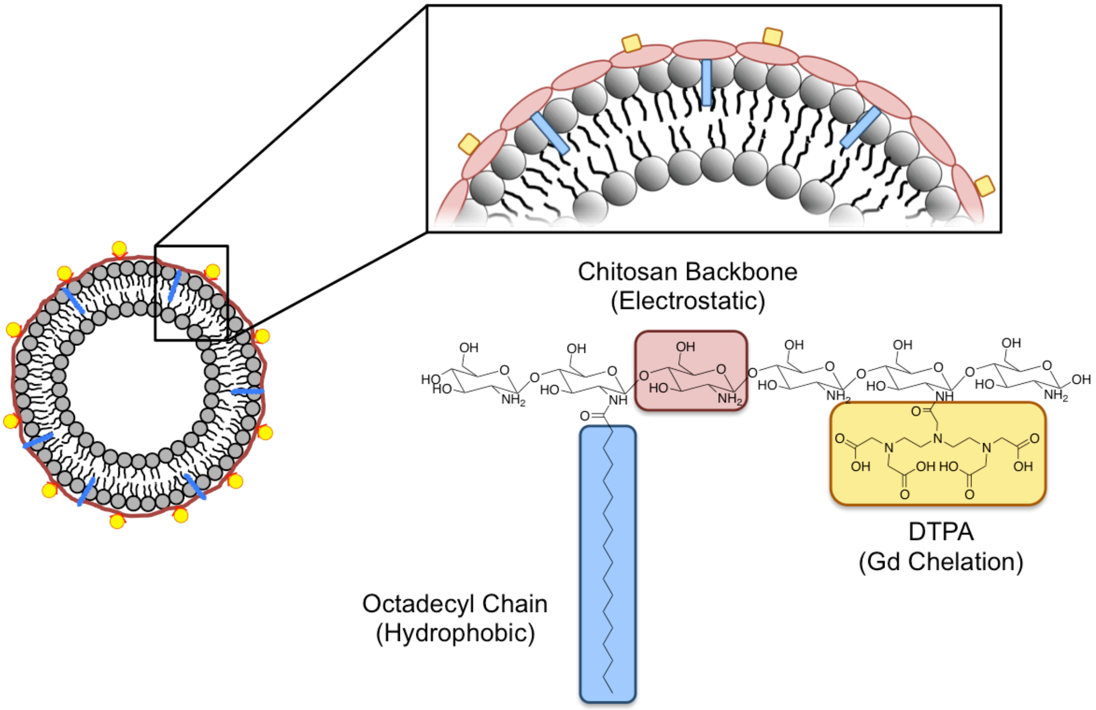

Figure 2.1 Schematic diagram of association between a pre-formed liposome and DTPA-chitosan-g-C_{18}.

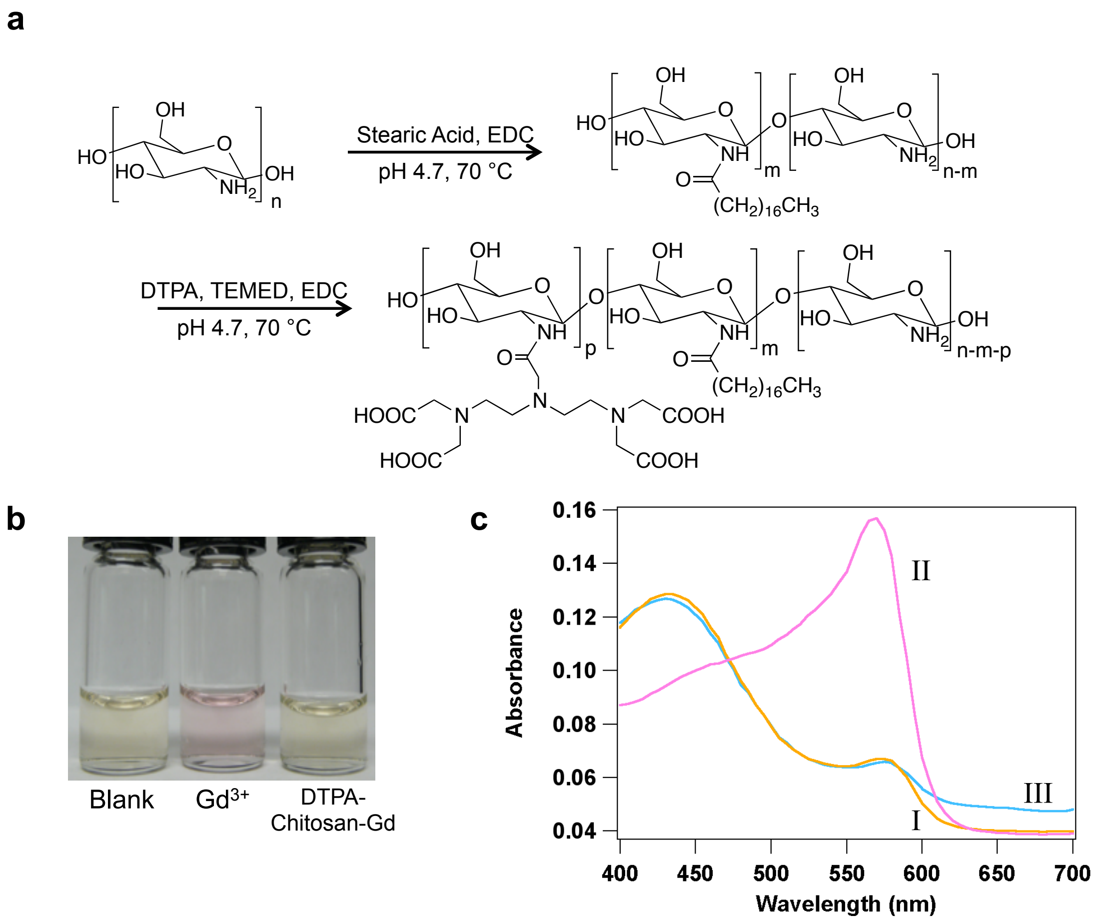

Figure 2.2 Synthesis and characterization of DTPA-chitosan-g-C_{18}. (a) Synthesis of DTPA-chitosan-g-C_{18} formed by the sequential reaction of stearic acid and DTPA with glucosamine units of chitosan. (b) Color of xylenol orange in media without any $GdCl_3$ (first vial), media with free $GdCl_3$ (second vial), and a mixture of $GdCl_3$ chelated by DTPA-chitosan (third vial). (c) The UV absorbance spectra of xylenol orange in media without $GdCl_3$ (I), media with free $GdCl_3$ (II), and the mixture of $GdCl_3$ chelated by DTPA-chitosan-g-C_{18} (III).

Table 2.1 Characterization of degree of substitution of octadecyl chains (DS_{C18}) and DTPA (DS_{DTPA}) to chitosan using TNBS and xylenol orange assays.

stoichiometric DS_{C18} (mol %)	DS_{C18} (mol %)	DS_{DTPA} (mol %)
0	-	15.3
2	2.3	15.9
5	4.2	15.4

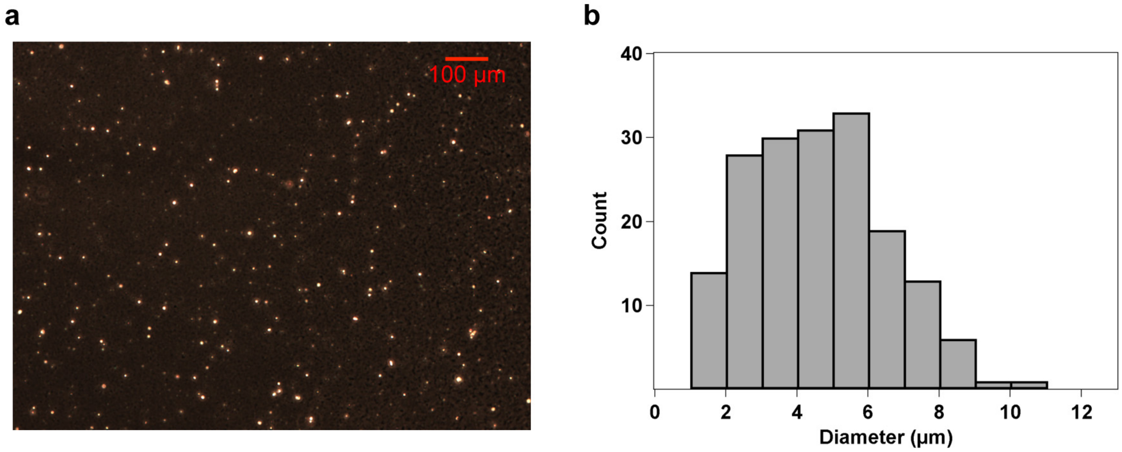

Figure 2.3 Size analysis of liposome particles. (a) Phase contrast microscope image taken with a Leica D-LUX 3 CCD camera. (b) Size distribution of liposomes was characterized by ImageJ software from microscope images. The average diameter of 176 particles was 4.6 ± 2 μm.

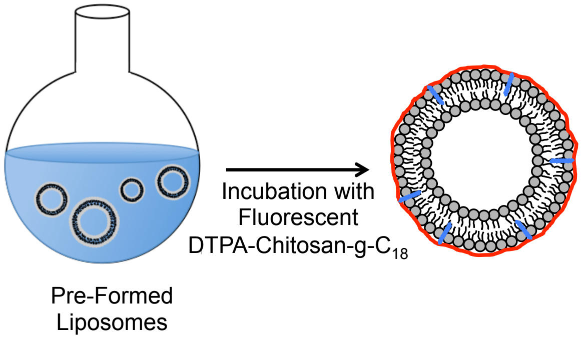

Figure 2.4 Schematic depiction of the process to coat the outer liposome leaflet.

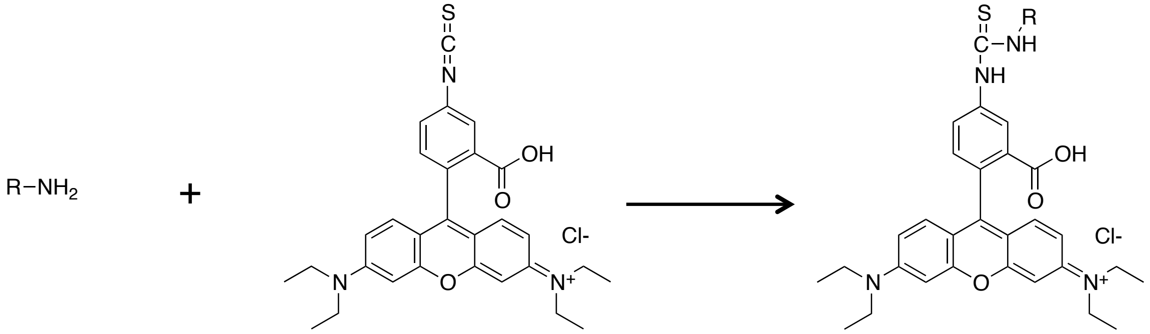

Figure 2.5 Fluorescent labeling of modified chitosan with rhodamine B isothiocyanate. *R* represents the chitosan backbone. The reaction took place in water at room temperature.

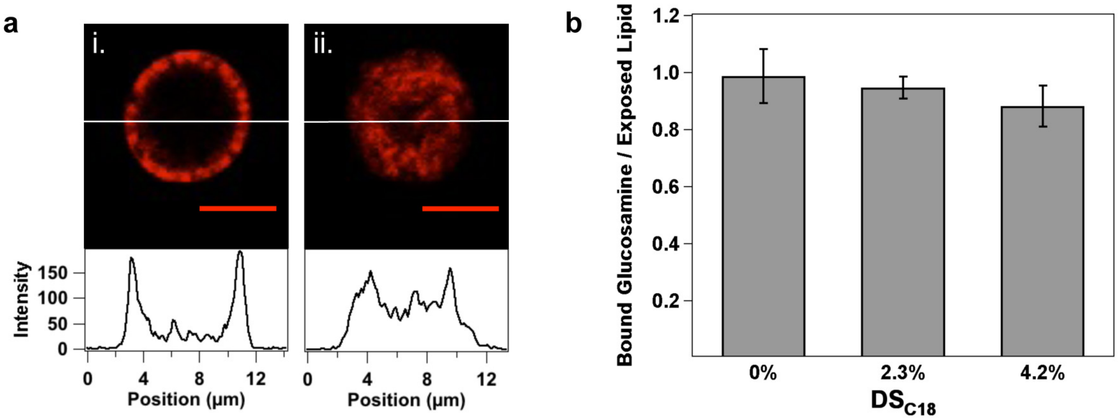

Figure 2.6 Fluorescence analysis of liposomes associated with DTPA-chitosan-g-C_{18}. (a) A confocal microscopic image of rhodamine-labeled DTPA-chitosan-g-C_{18} anchored to the liposome surface (i), and encapsulated within the liposome (ii). Scale bars represent 5 μm, and intensity profiles are shown across the liposome diameter as indicated. (b) With excess DTPA-chitosan or DTPA-chitosan-g-C_{18}, liposomes were coated at a 1:1 ratio of glucosamine unit to exposed lipid. Therefore, the number of chitosan subunits bound to a liposome was independent of the degree of substitution of octadecyl chains (DS_{C18}).

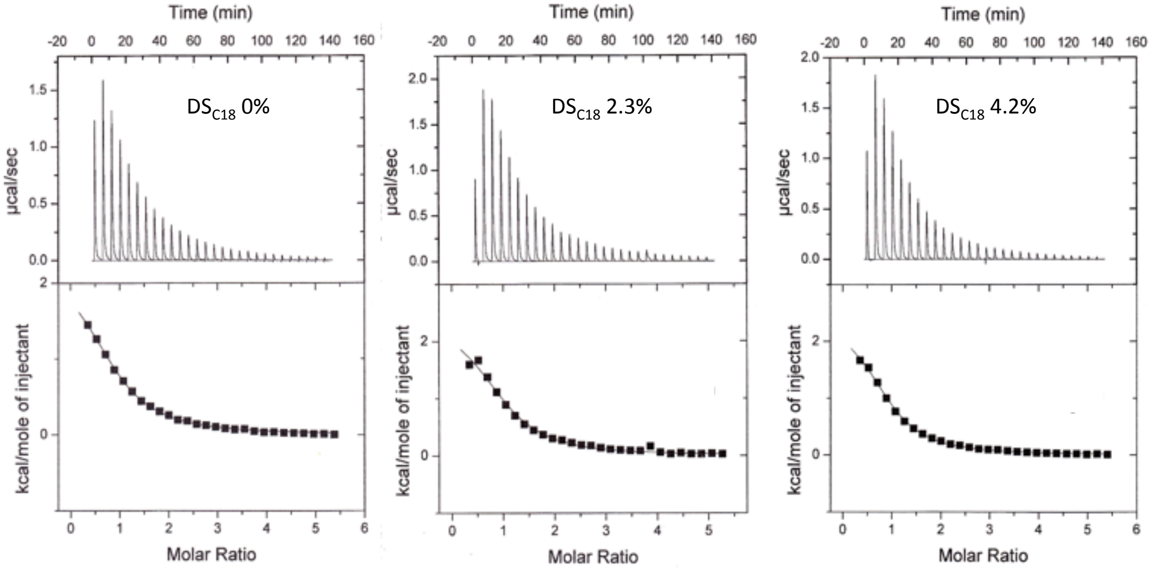

Figure 2.7 Thermograms of DTPA-chitosan (left), and DTPA-chitosan-g-C_{18} with DS_{C18} = 2.3% (middle) and 4.2% (right). The top row represents raw heat flow data, while the bottom row is data fit to a single-site binding model.

Table 2.2 Thermodynamic parameters derived from ITC analysis of chitosan-liposome binding. Values are given per mole of glucosamine unit and error values are the standard deviations of the fit parameters.

DS of C_{18} (mol %)	N	K 10^4 M^{-1}	ΔH kcal/mol	ΔG kcal/mol	ΔS cal/mol•K
0	0.88 ± 0.02	1.55 ± 0.08	2.31 ± 0.07	-5.71	26.9
2.3	0.98 ± 0.05	1.91 ± 0.27	2.43 ± 0.17	-5.83	27.7
4.2	0.89 ± 0.02	2.22 ± 0.12	2.43 ± 0.06	-5.92	28.0

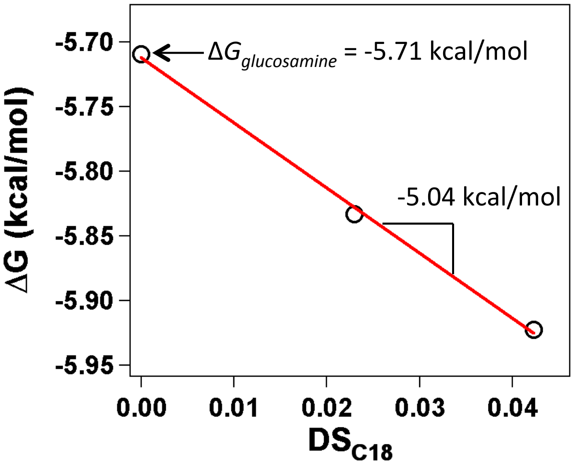

Figure 2.8 Linear regression of change in Gibbs free energy during the association (ΔG) *versus* DS_{C18}. The *y*-intercept represents the ΔG for a glucosamine unit ($\Delta G_{glucosamine}$), and the slope is equal to the difference between ΔG for octadecyl chains (ΔG_{C18}) and $\Delta G_{glucosamine}$.

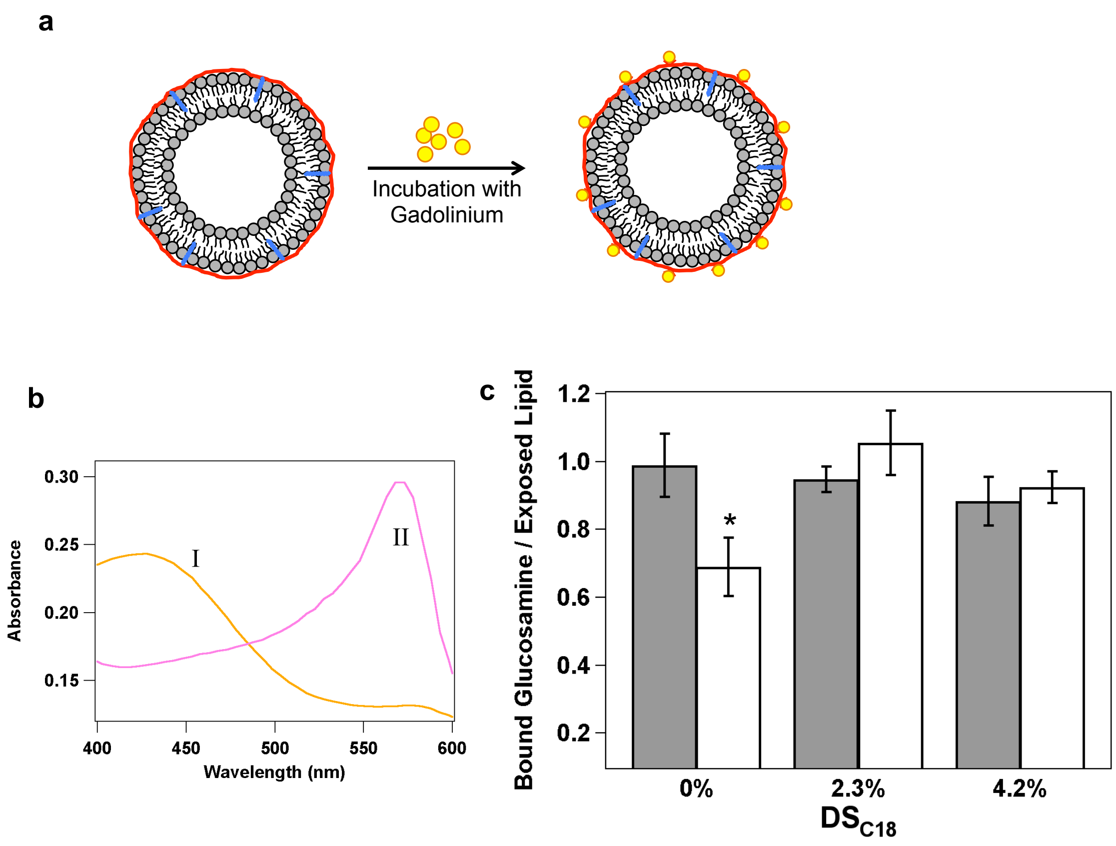

Figure 2.9 Gadolinium loading on the liposome surface *via* DTPA-chitosan or DTPA-chitosan-g-C_{18}. (a) Schematic depicting gadolinium chelation by chitosan-coated liposomes. (b) The xylenol orange absorbance spectra of the mixture of $GdCl_3$ and liposome coated by DTPA-chitosan or DTPA-chitosan-g-C_{18} (I) and the mixture of $GdCl_3$ and uncoated liposome (II). (c) Analysis of DTPA-chitosan or DTPA-chitosan-g-C_{18} bound to a liposome with (open bars) and without (shaded bars) addition of $GdCl_3$ in the liposome suspension. Asterisk (*) represents statistical significance of the difference in the amount of DTPA-chitosan adsorbed to liposomes in the presence and absence of $GdCl_3$ (*$p < 0.05$).

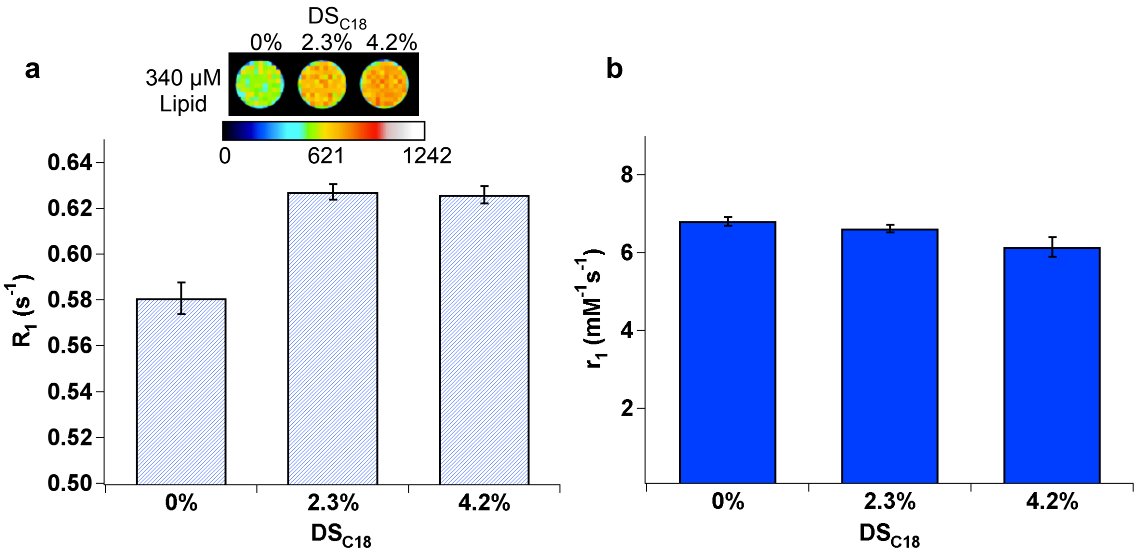

Figure 2.10 Effects of DS$_{C18}$ of DTPA-chitosan-g-C$_{18}$ on the liposome's ability to enhance MRI contrast. (a) Pseudocolored MR phantom image and longitudinal relaxation rate (R_1) of the gadolinium-loaded liposome (TI = 1000 ms). MR contrast and R_1 were further increased with liposomes coated by DTPA-chitosan-g-C$_{18}$. The scale bar represents MR signal intensity. (b) The independence of molar relaxivity (r_1) on DS$_{C18}$. Error bars represent standard deviation of the fit parameter.

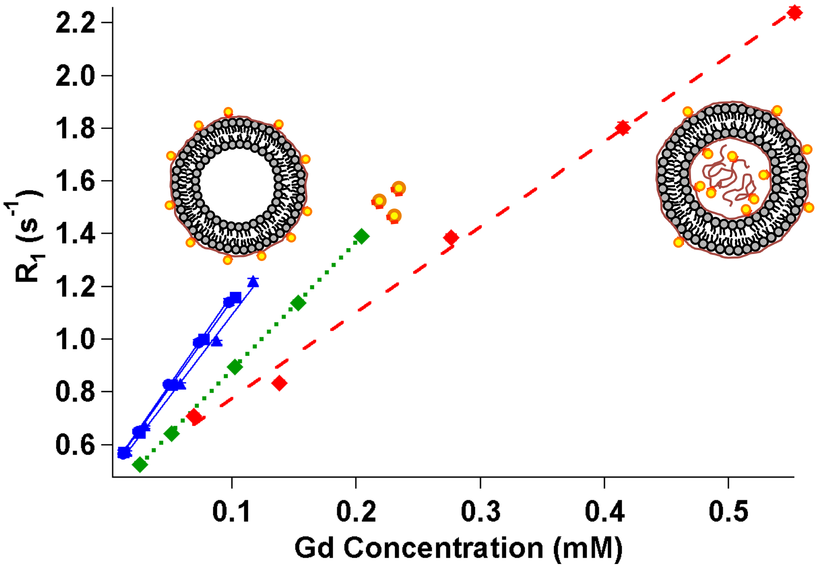

Figure 2.11 Relaxivity plot for Gd-containing liposome particles. Relaxivities shown in Figure 2.10 are determined from the slopes of the blue solid curves. The red dashed curve was used to determine the molar relaxivity of DTPA-chitosan-g-C_{18} encapsulated and adsorbed to the liposome. The green dotted curve represents unmodified DTPA-Gd.

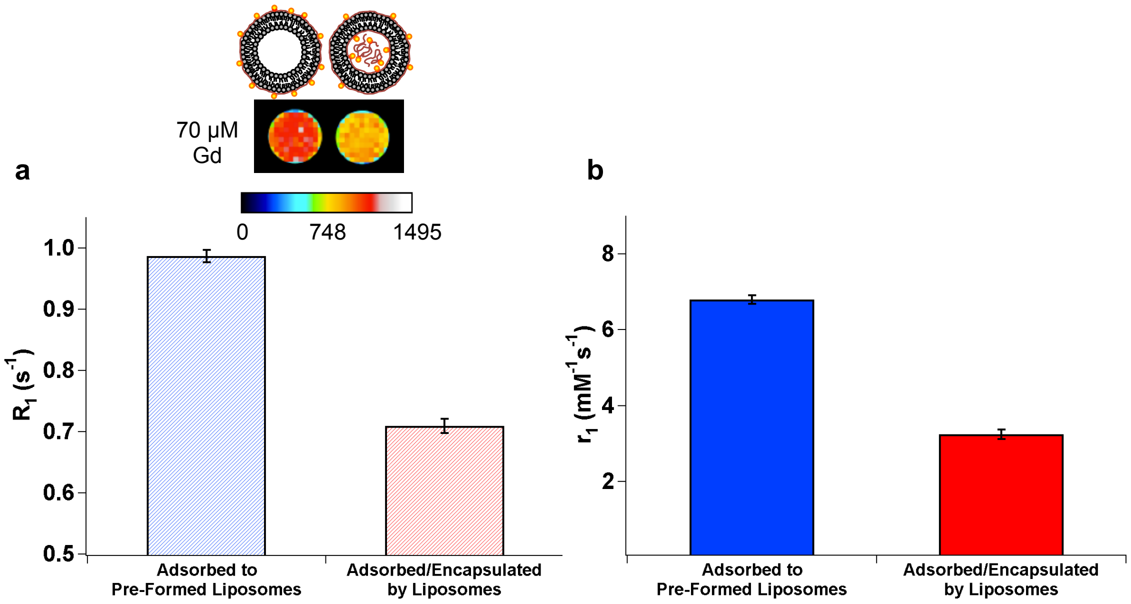

Figure 2.12 Effects of gadolinium loading strategy on MR signal and molar relaxivity of gadolinium. (a) Pseudocolored MR phantom image and longitudinal relaxation rate (R_1) of liposomes bound with gadolinium exclusively on the outer leaflet (left liposome in the MR image) and on both outer leaflet and interior of the liposome (right liposome in the MR image), (TI = 1000 ms). The total gadolinium concentration in the phantom samples was kept constant at 70 µM. (b) Molar relaxivities (r_1) of the liposomes bound with gadolinium on the outer leaflet (blue bar) and liposomes with gadolinium adsorbed on the exterior and encapsulated (red bar). Error bars represent standard deviation of the fit parameter.

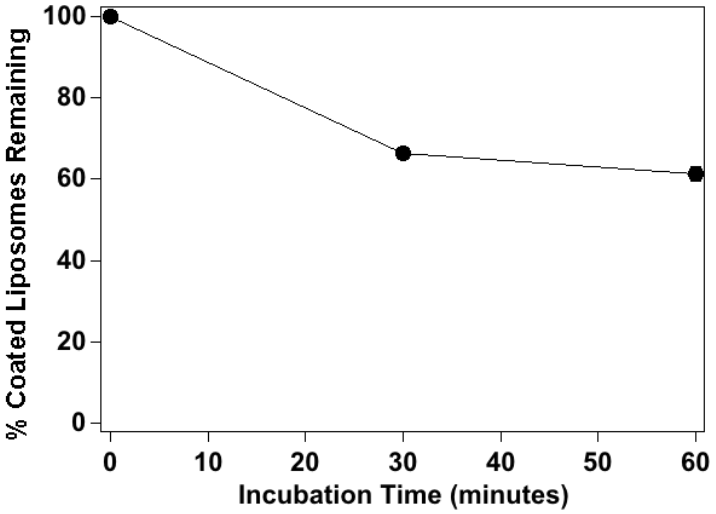

Figure 2.13 Analysis of association between DTPA-chitosan-g-C_{18} and liposomes in the presence of human serum. Data is shown as the average of two replicates per time point, with error bars obscured by data point markers.

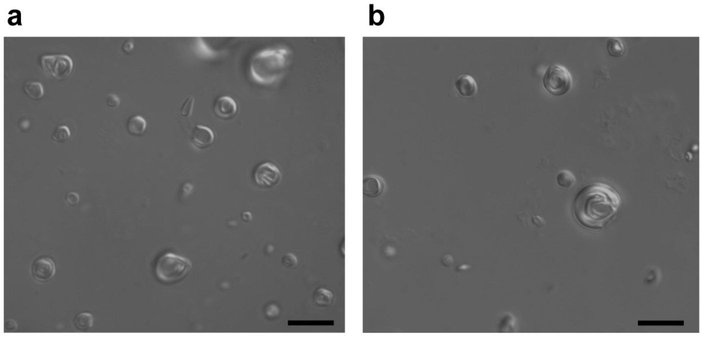

Figure 2.14 Microscopic images of liposomes coated by DTPA-chitosan-g-C_{18} (DS_{C18} = 4.2%). Images were taken with a Zeiss Axiovert 200M microscope before (a) and after (b) 1 h incubation in PBS supplemented with 10% serum. Scale bars represent 10 μm. The average diameters of liposomes before and after one-hour incubation in serum-supplemented PBS were 4.3 ± 2 and 3.7 ± 2 μm respectively. 272 and 175 particles were measured for the conditions.

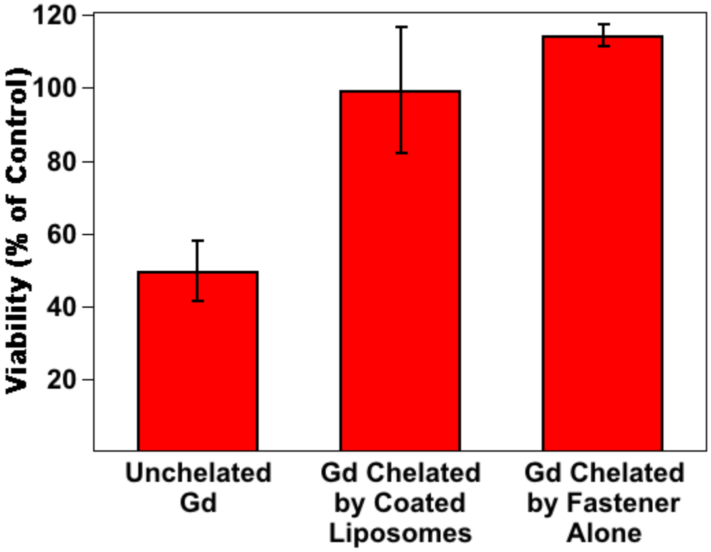

Figure 2.15 Cellular viability analyzed with an MTT assay for cellular metabolic activity. The level of viability was quantified by normalizing the absorbance values after incubation with MTT reagent to that of cells cultured without addition of gadolinium. Error bars represent standard deviation of three replicates.

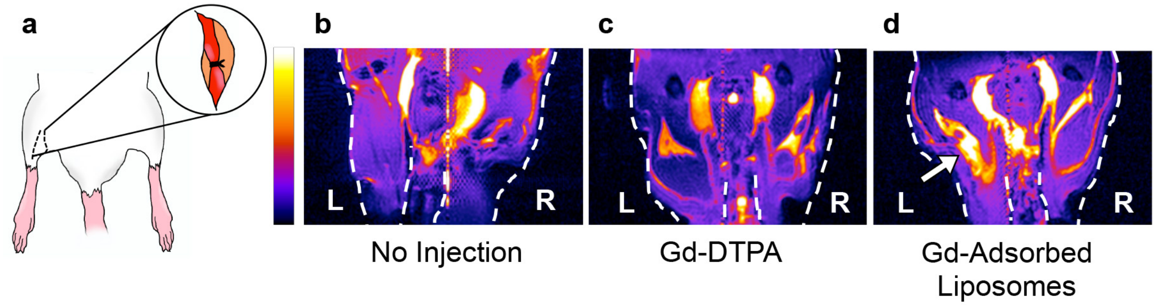

Figure 2.16 Evaluation of gadolinium contrast agents with a murine model of hindlimb ischemia. (a) The femoral artery of the left hindlimb was ligated to prevent blood flow. (b-d) MR images of left and right hindlimbs of (b) a mouse that did not receive gadolinium, (c) a mouse that was injected with DPTA-gadolinium chelates, and (d) a mouse injected with gadolinium loaded on liposome surfaces. The arrow in (d) indicates significant accumulation of liposomes loaded with gadolinium. The color scale bar is proportional to MR signal intensity, and images are presented at the same grayscale levels.

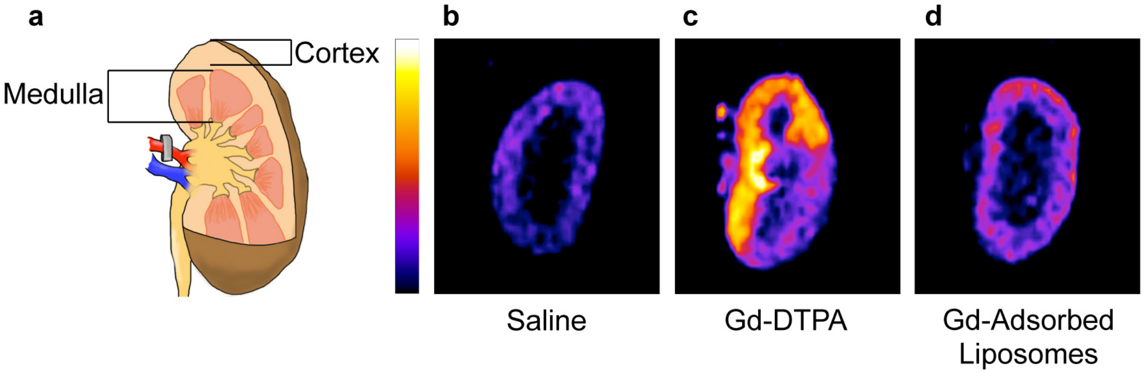

Figure 2.17 Analysis of gadolinium-loaded liposomes in a rat model of renal ischemia. (a) Renal arteries were occluded prior to injection of contrast agent. (b-d) MR images of coronal sections of kidneys injected with (b) saline, (c) free gadolinium-DTPA, and (d) liposomes surface-loaded with gadolinium. Images are pseudocolored and shown on the same grayscale.

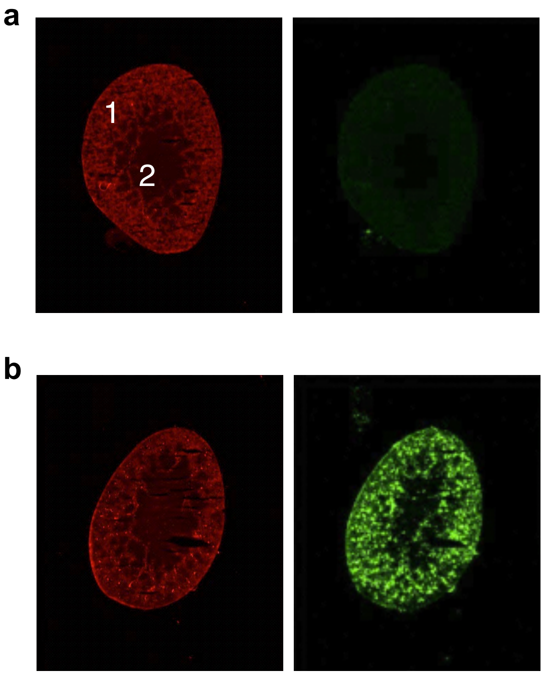

Figure 2.18 Tissue sections of Sprague Dawley rat kidneys injected with (a) saline, and (b) liposomes labeled with CellVue NIR815 dye. The 680 excitation channel is shown in red and displays tissue autofluorescence. Cortex (marked as **1**) is easily distinguished from medulla (marked as **2**). The 780 excitation channel, shown in green, demonstrates localization of fluorescently labeled liposomes within the cortex.

2.7 References

1. Jokerst, J. V.; Gambhir, S. S. Molecular Imaging with Theranostic Nanoparticles. *Acc. Chem. Res.* **2011,** *44*, 1050-1060.

2. Shi, J.; Xiao, Z.; Kamaly, N.; Farokhzad, O. C. Self-Assembled Targeted Nanoparticles: Evolution of Technologies and Bench to Bedside Translation. *Acc. Chem. Res.* **2011,** *44*, 1123-1134.

3. Gianella, A.; Jarzyna, P. A.; Mani, V.; Ramachandran, S.; Calcagno, C.; Tang, J.; Kann, B.; Dijk, W. J. R.; Thijssen, V. L.; Griffioen, A. W., *et al.* Multifunctional Nanoemulsion Platform for Imaging Guided Therapy Evaluated in Experimental Cancer. *ACS Nano* **2011,** *5*, 4422-4433.

4. Lavik, E.; von Recum, H. The Role of Nanomaterials in Translational Medicine. *ACS Nano* **2011,** *5*, 3419-3424.

5. Weissleder, R.; Pittet, M. J. Imaging in the Era of Molecular Oncology. *Nature* **2008,** *452*, 580-589.

6. Louie, A. Multimodality Imaging Probes: Design and Challenges. *Chem. Rev.* **2010,** *110*, 3146-3195.

7. Kobayashi, H.; Koyama, Y.; Barrett, T.; Hama, Y.; Regino, C. A. S.; Shin, I. S.; Jang, B.-S.; Le, N.; Paik, C. H.; Choyke, P. L., *et al.* Multimodal Nanoprobes for Radionuclide and Five-Color Near-Infrared Optical Lymphatic Imaging. *ACS Nano* **2007,** *1*, 258-264.

8. Abraham, S. A.; Edwards, K.; Karlsson, G.; MacIntosh, S.; Mayer, L. D.; McKenzie, C.; Bally, M. B. Formation of Transition Metal-Doxorubicin Complexes inside Liposomes. *Biochim. Biophys. Acta* **2002,** *1565*, 41-54.

9. Kim, B.-S.; Taton, T. A. Multicomponent Nanoparticles via Self-Assembly with Cross-Linked Block Copolymer Surfactants. *Langmuir* **2006,** *23*, 2198-2202.

10. Onuki, Y.; Jacobs, I.; Artemov, D.; Kato, Y. Noninvasive Visualization of in Vivo Release and Intratumoral Distribution of Surrogate MR Contrast Agent Using the Dual MR Contrast Technique. *Biomaterials* **2010,** *31*, 7132-7138.

11. Na, K.; Lee, S. A.; Jung, S. H.; Shin, B. C. Gadolinium-Based Cancer Therapeutic Liposomes for Chemotherapeutics and Diagnostics. *Colloids Surf., B* **2011,** *84*, 82-87.

12. Ghaghada, K.; Hawley, C.; Kawaji, K.; Annapragada, A.; Mukundan Jr, S. T1 Relaxivity of Core-Encapsulated Gadolinium Liposomal Contrast Agents— Effect of Liposome Size and Internal Gadolinium Concentration. *Acad. Radiol.* **2008,** *15*, 1259-1263.

13. Kong, H. J.; Mooney, D. J. Microenvironmental Regulation of Biomacromolecular Therapies. *Nat. Rev. Drug. Discovery* **2007,** *6*, 455-463.

14. Henrotte, V.; Laurent, S.; Gabelica, V.; Elst, L. V.; Depauw, E.; Muller, R. N. Investigation of Non-Covalent Interactions between Paramagnetic Complexes and Human Serum Albumin by Electrospray Mass Spectrometry. *Rapid Commun. Mass Spectrom.* **2004,** *18*, 1919-1924.

15. Wang, Y.; Spiller, M.; Caravan, P. Evidence for Weak Protein Binding of Commercial Extracellular Gadolinium Contrast Agents. *Magn. Reson. Med.* **2010,** *63*, 609-616.

16. Mulder, W. J. M.; Strijkers, G. J.; Griffioen, A. W.; van Bloois, L.; Molema, G.; Storm, G.; Koning, G. A.; Nicolay, K. A Liposomal System for Contrast-Enhanced Magnetic Resonance Imaging of Molecular Targets. *Bioconjugate Chem.* **2004,** *15*, 799-806.

17. Accardo, A.; Tesauro, D.; Roscigno, P.; Gianolio, E.; Paduano, L.; D'Errico, G.; Pedone, C.; Morelli, G. Physicochemical Properties of Mixed Micellar Aggregates Containing CCK Peptides and Gd Complexes Designed as Tumor Specific Contrast Agents in MRI. *J. Am. Chem. Soc.* **2004,** *126*, 3097-3107.

18. Gong, P.; Chen, Z.; Chen, Y.; Wang, W.; Wang, X.; Hu, A. High-Relaxivity MRI Contrast Agents Prepared from Miniemulsion Polymerization Using Gadolinium(III)-Based Metallosurfactants. *Chem. Commun.* **2011,** *47*, 4240-4242.

19. Ratzinger, G.; Agrawal, P.; Körner, W.; Lonkai, J.; Sanders, H. M. H. F.; Terreno, E.; Wirth, M.; Strijkers, G. J.; Nicolay, K.; Gabor, F. Surface Modification of PLGA Nanospheres with Gd-DTPA and Gd-DOTA for High-Relaxivity MRI Contrast Agents. *Biomaterials* **2010,** *31*, 8716-8723.

20. Liu, L.; Law, W.-C.; Yong, K.-T.; Roy, I.; Ding, H.; Erogbogbo, F.; Zhang, X.; Prasad, P. N. Multimodal Imaging Probes Based on Gd-DOTA Conjugated Quantum Dot Nanomicelles. *Analyst* **2011,** *136*, 1881-1886.

21. Kamaly, N.; Xiao, Z.; Valencia, P. M.; Radovic-Moreno, A. F.; Farokhzad, O. C. Targeted Polymeric Therapeutic Nanoparticles: Design, Development and Clinical Translation. *Chem. Soc. Rev.* **2012,** *41*, 2971-3010.

22. Singer, S. J.; Nicolson, G. L. The Fluid Mosaic Model of the Structure of Cell Membranes. *Science* **1972,** *175*, 720-731.

23. White, S. H. Membrane Protein Insertion: The Biology-Physics Nexus. *J. Cell Biol.* **2007,** *177*, 363-369.

24. Paulick, M. G.; Bertozzi, C. R. The Glycosylphosphatidylinositol Anchor: A Complex Membrane-Anchoring Structure for Proteins. *Biochemistry* **2008,** *47*, 6991-7000.

25. Guy-Caffey, J. K.; Webster, R. E. The Membrane Domain of a Bacteriophage Assembly Protein. Transmembrane-Directed Proteolysis of a Membrane-Spanning Fusion Protein. *J. Biol. Chem.* **1993,** *268*, 5488-5495.

26. Gallusser, A.; Kuhn, A. Initial Steps in Protein Membrane Insertion. Bacteriophage M13 Procoat Protein Binds to the Membrane Surface by Electrostatic Interaction. *EMBO J.* **1990,** *9*, 2723-2729.

27. Kuhn, A.; Kreil, G.; Wickner, W. Both Hydrophobic Domains of M13 Procoat Are Required to Initiate Membrane Insertion. *EMBO J.* **1986,** *5*, 3681-3685.

28. Ayyagari, A. L.; Zhang, X.; Ghaghada, K. B.; Annapragada, A.; Hu, X.; Bellamkonda, R. V. Long-Circulating Liposomal Contrast Agents for Magnetic Resonance Imaging. *Magn. Reson. Med.* **2006,** *55*, 1023-1029.

29. Yuan, H.; Lu, L.-J.; Du, Y.-Z.; Hu, F.-Q. Stearic Acid-g-Chitosan Polymeric Micelle for Oral Drug Delivery: In Vitro Transport and in Vivo Absorption. *Mol. Pharmaceutics* **2010,** *8*, 225-238.

30. Darras, V.; Nelea, M.; Winnik, F. M.; Buschmann, M. D. Chitosan Modified with Gadolinium Diethylenetriaminepentaacetic Acid for Magnetic Resonance Imaging of DNA/Chitosan Nanoparticles. *Carbohydr. Polym.* **2010,** *80*, 1137-1146.

31. Barge, A.; Cravotto, G.; Gianolio, E.; Fedeli, F. How to Determine Free Gd and Free Ligand in Solution of Gd Chelates. A Technical Note. *Contrast Media Mol. Imaging* **2006,** *1*, 184-188.

32. ITC Data Analysis in Origin. *Tutorial Guide*, 5th ed.; MicroCal LLC: Northampton, MA, 1998.

33. Israelachvili, J. N. Thermodynamic Principles of Self-Assembly. In *Intermolecular and Surface Forces*, 3rd ed.; Academic Press: San Diego, CA, 2011; pp 503-534.

34. Quemeneur, F.; Rinaudo, M.; Maret, G.; Pepin-Donat, B. Decoration of Lipid Vesicles by Polyelectrolytes: Mechanism and Structure. *Soft Matter* **2010,** *6*, 4471-4481.

35. Taira, M. C.; Chiaramoni, N. S.; Pecuch, K. M.; Alonso-Romanowski, S. Stability of Liposomal Formulations in Physiological Conditions for Oral Drug Delivery. *Drug Deliv.* **2004,** *11*, 123-128.

36. Kirby, C.; Clarke, J.; Gregoriadis, G. Effect of the Cholesterol Content of Small Unilamellar Liposomes on Their Stability in Vivo and in Vitro. *Biochem. J.* **1980,** *186*, 591-598.

37. Limbourg, A.; Korff, T.; Napp, L. C.; Schaper, W.; Drexler, H.; Limbourg, F. P. Evaluation of Postnatal Arteriogenesis and Angiogenesis in a Mouse Model of Hind-Limb Ischemia. *Nat. Protocols* **2009,** *4*, 1737-1748.

38. Niiyama, H.; Huang, N. F.; Rollins, M. D.; Cooke, J. P. Murine Model of Hindlimb Ischemia. *J. Visualized Exp.* **2009**, 1035.

39. Hong, G.; Lee, J. C.; Robinson, J. T.; Raaz, U.; Xie, L.; Huang, N. F.; Cooke, J. P.; Dai, H. Multifunctional In Vivo Vascular Imaging Using Near-Infrared II Fluorescence. *Nat. Med.* **2012,** *18*, 1841-1846.

40. Dagher, P. C.; Herget-Rosenthal, S.; Ruehm, S. G.; Jo, S.-K.; Star, R. A.; Agarwal, R.; Molitoris, B. A. Newly Developed Techniques to Study and Diagnose Acute Renal Failure. *J. Am. Soc. Nephrol.* **2003,** *14*, 2188-2198.

41. Sarmento, B.; Mazzaglia, D.; Bonferoni, M. C.; Neto, A. P.; do Céu Monteiro, M.; Seabra, V. Effect of Chitosan Coating in Overcoming the Phagocytosis of Insulin Loaded Solid Lipid Nanoparticles by Mononuclear Phagocyte System. *Carbohydr. Polym.* **2011,** *84*, 919-925.

42. Amoozgar, Z.; Park, J.; Lin, Q.; Yeo, Y. Low Molecular-Weight Chitosan as a pH-Sensitive Stealth Coating for Tumor-Specific Drug Delivery. *Mol. Pharmaceutics* **2012,** *9*, 1262-1270.

43. Rohrer, M.; Bauer, H.; Mintorovitch, J.; Requardt, M.; Weinmann, H. J. Comparison of Magnetic Properties of MRI Contrast Media Solutions at Different Magnetic Field Strengths. *Invest. Radiol.* **2005,** *40*, 715-724.

44. Odintsov, B. Tunable Radiofrequency Coil. U.S. Patent US 8,049,502 B2, November 1, 2011.

CHAPTER 3

GADOLINIUM LABELING VIA A POLYMERIC FASTENER FOR MRI CELL TRACKING

Acknowledgments

I would like to acknowledge the contributions of Brenda Andrade, who provided the amine-functionalized HPG, and Minkyung Lee for assisting with the acquisition of the confocal microscopy images in Figures 3.1 and 3.2. I would also like to thank Ryan Larsen at the Beckman Institute for Advanced Science and Technology for assistance in using the MR scanner. Gadolinium content analysis was performed by the School of Chemical Sciences Microanalysis Laboratory.

3.1 Introduction

Cellular therapies have become increasingly used in the treatment of various disorders, including cardiovascular disease,[1-3] cancer,[4,5] metabolic disorders,[6,7] and neurological diseases,[8-10] which are still difficult to treat with currently available drug molecules. For example, islet cells isolated from the pancreas endogenously secrete insulin used to treat diabetic patients.[11] Stem cells from bone marrow or adipose tissue secrete anti-inflammatory factors, angiogenic growth factors, and neurotrophic factors over an extended period of time, and can differentiate into cells that form specific tissues of interest.[12-14] Success in such cellular therapies greatly relies on the ability to monitor transplanted or mobilized cells using non-invasive imaging tools.

In this way, labeling of cells has emerged as a promising way to evaluate cellular phenotype, engraftment, and therapeutic outcomes *in vivo*.[15] Additionally, cells can be labeled for diagnostic applications, such as the tagging of leukocytes to non-invasively locate areas of infection.[16,17] While many approaches have been traditionally performed with radionuclides for imaging by positron emission tomography (PET), contrast agents for magnetic resonance imaging (MRI) have become an area of interest due to the high spatial resolution and non-ionizing radiation of MRI.[18]

Superparamagnetic iron oxide nanoparticles (SPIONs) lend themselves well to such applications as a negative contrast agent, since they can be readily formulated for labeling by cellular uptake.[19] SPIONs, however, tend to exaggerate target areas as a result of susceptibility artifacts, and their negative contrast can be difficult to distinguish from void space in images.[20] Alternatively, gadolinium-based contrast agents can be used to provide positive contrast that is easy to distinguish from background features. Unlike SPIONs, however, gadolinium is not readily taken up into the cell. Therefore, chelates for gadolinium are typically administered within nanoparticle systems that can undergo cellular uptake, or with transfection agents to allow the chelate to cross the cell membrane.[21-24] In either case, the labeling procedure takes from 4-24 hours to accomplish, and may raise concerns of cytotoxicity. Furthermore, the molar relaxivity is greatly diminished upon uptake, as the interaction between the internalized contrast agent and water protons in surrounding fluid is reduced.[25]

We therefore hypothesized that a coating material that could immobilize gadolinium on a cell surface would present a simple strategy to rapidly label cells as well as reduce effects that weaken relaxivity. Previously, we demonstrated a chitosan-based polymeric fastener could coat the surface of a liposome as a method of post-fabrication modification to introduce gadolinium on the outer leaflet.[26,27] As the liposomal bilayer is structurally similar to the morphology of a cell, this study investigates approaches to similarly label a cell with a fastener that can chelate gadolinium and anchor itself to the lipid bilayer via hydrophobic alkyl chains (Figure 3.1a). Here we investigate two types of backbones for the fastener and discuss the advantages and challenges of each. First, chitosan was used in combination with polyethylene glycol (PEG) grafts. Secondly, hyperbranched polyglycerol (HPG) was then explored for its ability to present gadolinium away from the cell surface. Mouse D1 bone marrow stromal cells (BMSCs) were chosen as a model cell to demonstrate the feasibility of the approach, since BMSCs have been used previously in stem cell therapies, including the treatment of cardiovascular disease.[28-30] Overall, we believe the strategy of using a polymeric fastener to coat the cell will be advantageous in improving the quality of cell tracking by MRI.

3.2 Results

3.2.1 Coating of cells with DTPA-chitosan-g-C_{18}

Chitosan was modified with the gadolinium chelate, diethylenetriaminepentaacetic acid (DTPA) as well as octadecyl chains as previously described to create the polymeric fastener, DTPA-chitosan-g-C_{18}.[26] The degree of substitution of DTPA (DS_{DTPA}) was found to be 17.8%, while that of the alkyl chains (DS_{C18}) was 5.7% according to xylenol orange and a 2,4,6-trinitrobenzene sulfonic acid (TNBS) assays. Prior to cell labeling, DTPA-chitosan-g-C_{18} was loaded with an amount of gadolinium to occupy the DTPA binding sites. Additionally, BMSCs were suspended in media free of serum proteins that could potentially interfere with the labeling by binding with the modified chitosan. Rapid labeling of BMSCs was then achieved simply by mixing the cells in suspension with gadolinium-loaded DTPA-chitosan-g-C_{18}, followed by centrifugation to remove free fastener that remained unadsorbed to the cell. Successful immobilization of chitosan on the cell surface was confirmed with confocal microscopy, which indicated surface localization of rhodamine-labeled fastener after coating (Figure 3.1b).

To ensure that the adsorption of the modified chitosan on the cell surface did not result in cytotoxicity, an MTT assay for cellular metabolic activity was used. BMSCs were coated with DTPA-chitosan-g-C_{18} by incubating them in chitosan solutions at concentrations up to 2 mg/mL, containing 1.4 mM gadolinium. Cells were then placed in culture media and incubated for 24 h. As a result, there was no significant change in metabolic activity across any of the concentrations tested, compared to BMSCs cultured without the fastener (Figure 3.1c). Additionally, the chitosan fastener remained associated with the cells with minimal desorption for 24 h after loading, and continued to present itself on the cell's surface (Figure 3.2).

3.2.2. Magnetic resonance contrast capability of gadolinium-coated BMSCs

For MR imaging, coated cells were immobilized in a 1% agar gel to prevent their sedimentation during image acquisition. T_1 molar relaxivity was then determined for the chitosan fastener both in solution and adsorbed to the cell surface. Surprisingly, adsorption to the cell resulted in more than a 75% reduction in relaxivity (Figure 3.3). The result is not an inherent effect of chitosan immobilization, as DTPA-chitosan-g-C_{18} in an agar gel without cells had a comparable relaxivity value to that of the chitosan in solution (Figure 3.4). Additionally, as previously reported, when the fastener was used to coat liposomes, such a reduction in relaxivity was not observed.[26] The diminished relaxivity is therefore likely due to reduced interaction between gadolinium and surrounding water molecules. This could be due to the cell surface fostering a relatively hydrophobic environment. Additionally, and more dramatically, the water-binding site of gadolinium that accounts most strongly for the T_1 effects could be occupied through coordination with the various proteins and carbohydrates found on the cell. To investigate the former and promote hydrophilic interactions, DTPA-chitosan-g-C_{18} was further derivatized with PEG.

3.2.3. Relaxivity of PEGylated DTPA-chitosan-g-C_{18}

PEGylation was achieved by reaction of DTPA-chitosan-g-C_{18} with N-hydroxysuccinimide-terminated PEG (PEG-NHS) (Figure 3.5). Different lengths of PEG chain were investigated: PEG_4, PEG_{24}, and PEG_{100} with 4, 24, and approximately 100 ethylene glycol repeat units per chain. All had a similar degree of substitution (DS_{PEG}) on the chitosan backbone as determined by TNBS assay (Table 3.1). The solution of gadolinium-loaded fastener with the shortest PEG chain resulted in improved relaxivity (Figure 3.6a). However, with increasing length of PEG, relaxivity was reduced. The observation is similar to other studies in which longer PEG chains diminished relaxivity by limiting the access of water to gadolinium.[31] Consequently, when labeling BMSCs, the same trend in relaxivity with length of PEG chain was observed.

While PEGylation did not resolve the reduction in relaxivity upon adsorption to the cell, it did allow for signal enhancement at a reduced dose of gadolinium. The non-PEGylated DTPA-chitosan-g-C_{18} was able to load 42 pg/cell of gadolinium. Upon PEGylation, this value was reduced to 27 and 31 pg/cell for the fastener conjugated with PEG_4 and PEG_{24} respectively. The ability of the high molecular weight PEG_{100} to load gadolinium on the cell was undetermined, as the unadsorbed chitosan modified with this PEG had low colloidal stability and could not be purified from the coated BMSCs. Despite the reduced loading, PEG_4-DTPA-chitosan-g-C_{18} was able to produce contrast per cell equivalent to the non-PEGylated chitosan (Figure 3.6b). This was due to its higher molar relaxivity. The reduced loading of gadolinium via PEG_{24}-DTPA-chitosan-g-C_{18} combined with lower relaxivity, however, resulted in lower signal for any given cellular concentration.

To quantitatively compare the ability of each fastener to imbue the BMSCs with contrast capability, it is also important to consider the cell-based relaxivity normalized to concentration of cells rather than gadolinium concentration (Figure 3.6c). This takes into account both gadolinium loading and relaxation effects. Again, PEG_{24}-DTPA-chitosan-g-C_{18} had dramatically lower cell-based relaxivity than the other fasteners. While PEG_4-DTPA-chitosan-g-C_{18} was slightly less efficient at beaconing cells according to the cellular relaxivity, the phantom images produced were comparable to those of cells coated by non-PEGylated fastener, and therefore may still be advantageous due to the lower level of administered gadolinium required to produce the contrast.

Interestingly, even BMSCs fixed with paraformaldehyde prior to coating produced the same relaxivity reduction as live cells, and had the same cell-based relaxivity when coated by PEG_4-DTPA-chitosan-g-C_{18} (Figure 3.7). To resolve the cellular adsorption-induced relaxivity reduction, it may therefore be strategic to space the gadolinium away from the cell surface. Hyperbranched polyglycerol was investigated for its ability to achieve this spatial organization.

3.2.4. Synthesis and characterization of DTPA-HPG-g-C_{18}

HPG has been used in several other biomedical applications for its biocompatibility,[32] hydrophilicity, extended circulation time,[33] and furthermore, its ability to present ligands away from the cell surface as a result of its globular nature.[34] To form the HPG fastener, HPG with a molecular weight of approximately 4 kDa was functionalized with terminal primary amines to present reactive groups for conjugation of DTPA and C_{18} chains, as well as provide a basis for electrostatic interaction, similar to chitosan (Figure 3.8). In this way, DTPA-HPG-g-C_{18} could anchor to the cell surface via the alkyl chains while spacing the DTPA and gadolinium away from the cell (Figure 3.9a).

The relaxivity of DTPA-HPG-g-C_{18} in solution was similar to that of DTPA-chitosan-g-C_{18} (Figure 3.9b). However, upon adsorption to BMSCs, the relaxivity was reduced by only 35%, to 4.48 $mM^{-1}s^{-1}$. In this way, the HPG backbone was able to greatly improve the molar relaxivity. To the best of our knowledge, this is among the highest reported relaxivity values for gadolinium-based cell labeling techniques. Despite the marked improvement, however, the loading of gadolinium per cell was considerably low, at 2 pg/cell. For this reason, the cell-based relaxivity was the lowest of all of the fasteners tested, and the contrast in MR phantom images could barely be detected (Figure 3.10). For this reason, the HPG-based fastener was ultimately not advantageous in cell labeling with gadolinium. The reason for the low gadolinium loading is likely due to a reduction in both loading of gadolinium per fastener and loading of fastener per cell. For DTPA-chitosan-g-C_{18} or PEG_4-DTPA-chitosan-g-C_{18}, 1 mg of polymer could chelate approximately 0.7 μmol of gadolinium, while an equivalent amount of DTPA-HPG-g-C_{18} was only able to incorporate 0.2 μmol. This disparity, however, cannot completely account for the differences in the amount of gadolinium retained per cell. Therefore, the ability of the HPG fastener to adsorb to the cell must be improved in order to match the performance of the modified chitosan.

3.3 Discussion

The polymeric fastener approach labels cells with gadolinium much more rapidly than other techniques that rely on cellular uptake via nanoparticle or transfection. By simply mixing the fastener with the cells, labeling is achieved within 10 minutes with no further culturing or incubation needed, and cells can be used immediately. The amount of gadolinium loaded per cell and molar relaxivities are comparable to the highest values reported by others.[22] However, before further use, additional evaluation is needed to ensure proper cellular function. For example, in the case of therapeutic cells, such as BMSCs, the fastener must not interfere with the cells' ability to produce therapeutic proteins or differentiate, depending on the intended use. For targeted applications, it will be important to verify that coating the cell does not disrupt its adhesion to target sites, or it may be necessary to additionally include adhesion ligands on the fastener.

Other improvements to the fastener may result in higher loading and relaxivity in future studies. For example, using a higher molecular weight HPG as the fastener backbone would allow for increased alkylation and DTPA per molecule, as well as more unreacted amine groups to provide greater electrostatic interaction between fastener and cell. The larger HPG would also space more gadolinium farther from the cell surface, which could result in higher relaxivity than reported. Such improvements may allow the modified HPG to become more effective than the DTPA-chitosan-g-C_{18}, even at lower doses of gadolinium and would therefore represent great improvements in gadolinium cell labeling for MR tracking.

3.4 Conclusion

This study demonstrates the use of a polymeric fastener to rapidly and efficiently label BMSCs for applications in cell tracking. DTPA-chitosan-g-C_{18} was adsorbed to the cell surface within 10 min, and demonstrated no adverse effects to cellular metabolic activity over a wide range of concentrations. Further modification of the chitosan fastener with a low molecular weight PEG graft allowed for similar contrast levels at lower doses of gadolinium and may therefore be advantageous in imaging applications. While the relaxivity was, surprisingly, reduced upon adsorption to the cell, a fastener than can space gadolinium away from the cell may mitigate such effects by minimizing interactions that reduce access of water to the gadolinium-DTPA chelate. Overall, the labeling strategy will be broadly useful for tagging a wide variety of cell types for improved therapeutic and diagnostic cellular applications.

3.5 Materials and Methods

3.5.1 Synthesis and characterization of chitosan fasteners

All materials were purchased from Sigma-Aldrich unless otherwise noted. DTPA-chitosan-g-C_{18} was synthesized and characterized using the methods previously described in detail.[26] Briefly, the conjugation of C_{18} chains to the chitosan backbone was mediated by 1-ethyl-3-(3-dimethylaminopropyl) carbodiimide (EDC). EDC was then used in the subsequent attachment of DTPA. The degrees of substitution of C_{18} and DTPA were then determined by 2,4,6-trinitrobenzene sulfonic acid (TNBS) and xylenol orange assay respectively.

For chitosan fasteners containing PEG grafts, DTPA-chitosan-g-C_{18} was first dissolved in phosphate buffered saline (PBS). Then, amine-reactive N-hydroxysuccinimide (NHS) ester of PEG was added in the form of methyl-PEG_4-NHS, methyl-PEG_{24}-NHS (Fisher Scientific), or methyl-PEG-succinimidyl valerate (MW 5,000, Laysan Bio Inc.) to conjugate PEG chains of varying length. The reaction proceeded for 24 h at room temperature, followed by purification by dialysis dialysis (MWCO 6000-8000, Fisher Scientific) and lyophilization. The degree of substitution of PEG was then determined by TNBS assay to measure how many amines of the chitosan backbone were reacted with PEG-NHS.

3.5.2 Synthesis and characterization of DTPA-HPG-g-C_{18}

HPG was formed by polymerization of glycidol based on methods described previously,[35] and aminated. C_{18} chains and DTPA were then conjugated to create the HPG fastener. Briefly, HPG-amine was dissolved in a 2:1 PBS:ethanol mixture, followed by addition of EDC, sulfo-NHS (Fisher Scientific), and stearic acid at a 5:2:1 molar ratio. The reaction took place over 24 h while stirring at 70 ºC. Following reaction, dialysis was performed again for 1 day to remove unreacted material. DTPA was then added with EDC and sulfo-NHS at a 25:5:2 molar ratio. Purification proceeded by dialysis for 4 days, and the product was lyophilized. Successful chelation of gadolinium by DTPA-HPG-g-C_{18} was confirmed by xylenol orange assay.

3.5.3 Cell labeling by polymeric fastener

Mouse D1 bone marrow stromal cells (ATCC) were cultured in Dulbecco's Modified Eagle Media (DMEM, Corning) supplemented with 10% fetal bovine serum (FBS, Thermo Scientific) and 1% penicillin/streptomycin (Gibco). All cells used were at passage 28 or lower. Prior to coating, cells were resuspended in PBS. Separately, chitosan or HPG fastener was dissolved in PBS, and DTPA binding sites were saturated with a solution of gadolinium chloride ($GdCl_3$). The cell suspension was then mixed with an excess of fastener and incubated at 37 ºC for 10 min. Free, unadsorbed fastener was then removed by centrifugation at 200 ×g for 5 min to pellet the cells, and cells were resuspended in cell culture media.

3.5.4 Cell staining and confocal microscopy

For visualization, DTPA-chitosan-g-C18 was fluorescently labeled by reaction with rhodamine B isothiocyanate, followed by dialysis and lyophilization. The rhodamine-labeled chitosan was mixed with BMSCs as described, and coated cells were plated in culture media on a glass-bottomed dish. After 3 or 24 h, cells were washed with PBS and fixed with 4% paraformaldehyde for 10 min. They were then washed again and permeabilized with 0.5% Triton X-100 for 5 min, followed by another wash and overnight incubation at 4 ºC with 1% bovine serum albumin (BSA) blocking solution. Finally, cells were washed again and nuclei were stained with 4',6-diamidino- 2-phenylindole dihydrochloride (DAPI, Invitrogen). Imaging was then performed with a laser scanning confocal microscope (LSM 700, Carl Zeiss Microimaging, GmbH, Germany).

3.5.5 MTT assay for cellular metabolic activity

BMSCs were labeled by incubation with gadolinium-loaded fastener at concentrations up to 2 mg/mL, and then seeded with cell culture media in a 96-well plate at a density of 5×10^3 cells per well. After 24 h, (3-(4,5-dimethylthiazol-2-yl)-2,5-diphenyltetrazolium bromide (MTT, ATCC) was added and its reduction to formazan dye was used to assess metabolic activity. Following incubation with MTT reagent, cells were lysed with the addition of MTT detergent, and absorbance was measured at 570 nm with a microplate reader (Tecan Infinite 200 PRO).

3.5.6 Assessment of DTPA-chitosan-g-C_{18} desorption

To determine the degree to which DTPA-chitosan-g-C_{18} remained with the cell during incubation, BMSCs were coated with gadolinium-loaded fastener and seeded at 4×10^5 cells per well in a 12-well plate. At 3 and 24 h time points, the cell media was sampled, centrifuged, and digested with nitric acid for analysis of gadolinium content by inductively couple plasma optical emission spectroscopy (ICP-OES, Perkin-Elmer Optima 2000 DV, Norwalk, CT) to measure how much had desorbed from the cell. Gadolinium concentration was compared to the total amount associated with the seeded cells by analyzing the initial full cell media without purification by centrifugation. Additionally, an initial time point was taken immediately after cell coating to determine background gadolinium levels, which were subtracted from all other values.

3.5.7 Magnetic resonance imaging of fasteners and labeled cells

For relaxivity characterization and MR imaging, a concentration series of gadolinium-containing fasteners in deionized water was prepared by serial dilution in borosilicate cell culture tubes, which were then placed in an agar gel prior imaging to hold the samples and reduce imaging artifacts. For analysis of labeled cells, BMSCs were coated with an excess of fastener followed by purification to remove free chelate. Coated cells were then mixed 1:1 by volume with a 2% agar solution to prevent sedimentation and stored at 37 ºC. Imaging was performed within 1-2 h after cell labeling. In the case of imaging of fixed cells, BMSCs were suspended in 4% paraformaldehyde, washed with PBS, and then labeled with PEG$_4$-DTPA-chitosan-g-C$_{18}$ for imaging.

Imaging was performed on a 3 T Siemens Magnetom Trio clinical scanner (Siemens AG, Erlangen, Germany) with an inversion recovery turbo spin echo (IR-TSE) sequence. Images were acquired with a slice thickness was 3.0 mm, repetition time (TR) of 2500 ms, echo time (TE) of 18.0 ms, and inversion time (TI) ranging from 100 to 1700 ms. For each TI, signal intensity was measured with ImageJ software and used to determine T_1 relaxation by nonlinear least-squares curve fitting. Finally, relaxivity was determined by linear regression of relaxation rate ($1/T_1$) plotted against gadolinium concentration for each sample. Gadolinium content was measured by ICP-OES after digestion in nitric acid, and was also used to determine gadolinium loading per cell. Additionally, cell-based relaxivity was reported by linear regression of relaxation rate versus cell concentration rather than gadolinium concentration.

3.6 Figures and Tables

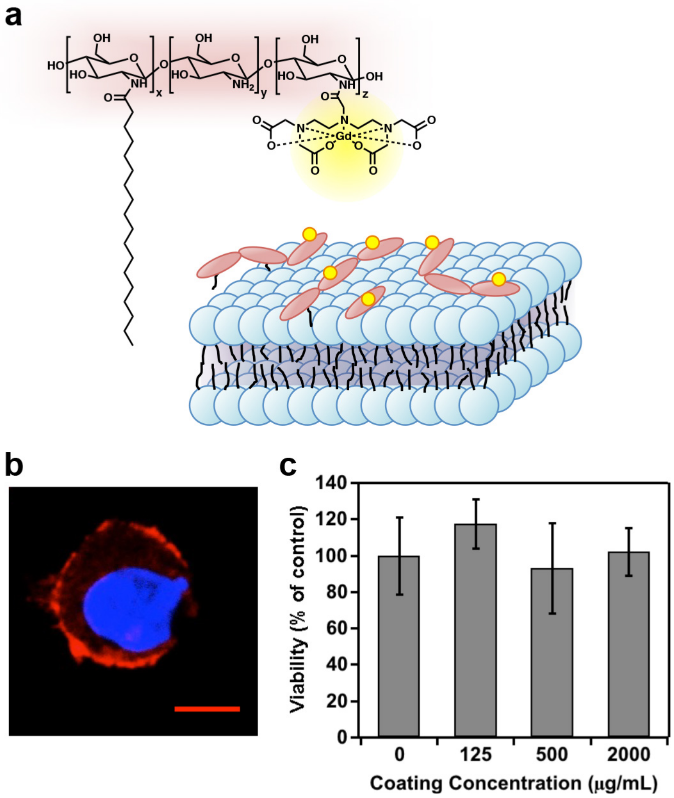

Figure 3.1 DTPA-chitosan-g-C_{18} as a polymeric fastener for cell labeling. (a) Scheme depicting DTPA-chitosan-g-C_{18} and its adsorption to the lipid bilayer. (b) Confocal microscopic image of the rhodamine-labeled, modified chitosan (red), anchored to the cell surface 3 h after labeling. The cell nucleus is highlighted with DAPI staining (blue). The scale bar represents 5 μm. (c) MTT assay for metabolic activity of BMSCs coated with DTPA-chitosan-g-C_{18} at various concentrations and incubated for 24 h. Absorbance values are normalized those of cells incubated without chitosan after blank subtraction. Error bars are the standard deviation of 3 replicates.

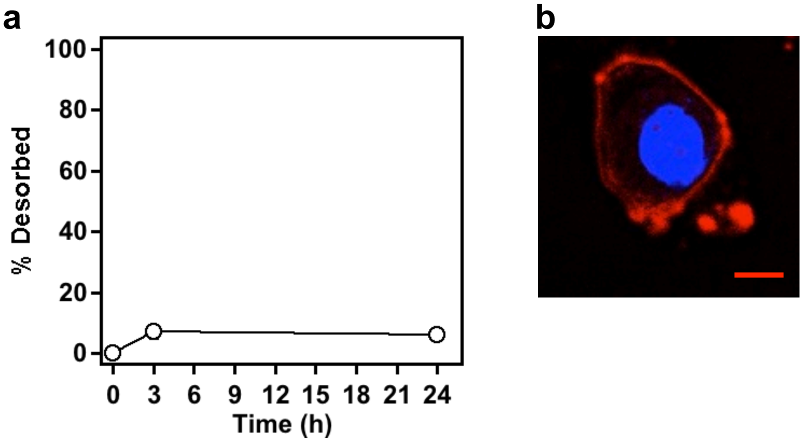

Figure 3.2 Stability of DTPA-chitosan-g-C_{18} during incubation. (a) Less than 10% of the initially adsorbed gadolinium-loaded fastener was desorbed from the cell over 24 h, as determined from the average of 3 replicates. Error bars are obscured by data point markers. (b) Labeled cells continued to display modified chitosan (red) on the surface after 24 h. The cell nucleus was stained with DAPI (blue). The scale bar represents 5 μm.

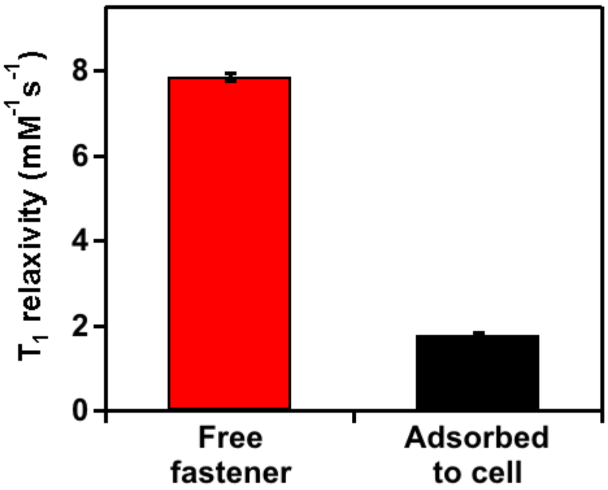

Figure 3.3 T_1 molar relaxivity of DTPA-chitosan-g-C_{18} free in solution and adsorbed to BMSCs. Error bars represent standard deviation of the fit parameter.

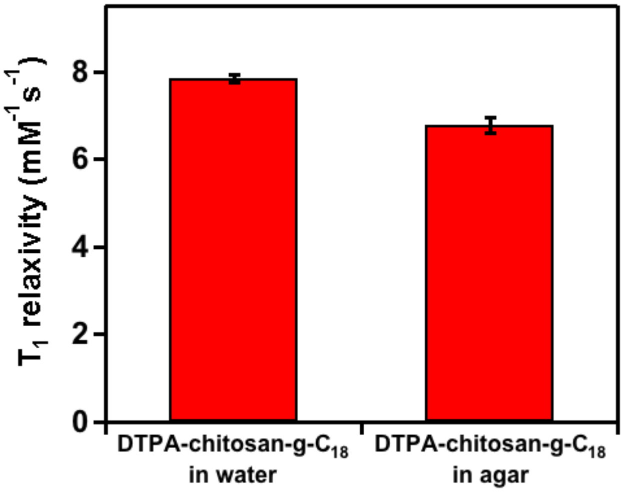

Figure 3.4 The relaxivity of gadolinium-loaded fastener was similar both in solution and immobilized in an agar gel. Error bars are the standard deviation of the fit parameter.

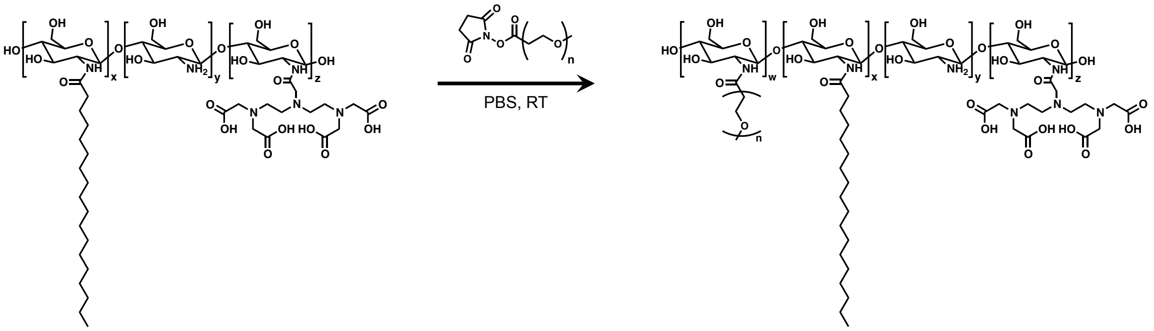

Figure 3.5 Modification of the chitosan fastener with PEG grafts of varying length.

Table 3.1 Degree of substitution of the PEG grafts (DS_{PEG}) conjugated to chitosan backbones as determined by TNBS assay.

PEG graft	DS_{PEG} (mol %)
PEG_4	15.3
PEG_{24}	19.6
PEG_{100}	13.7

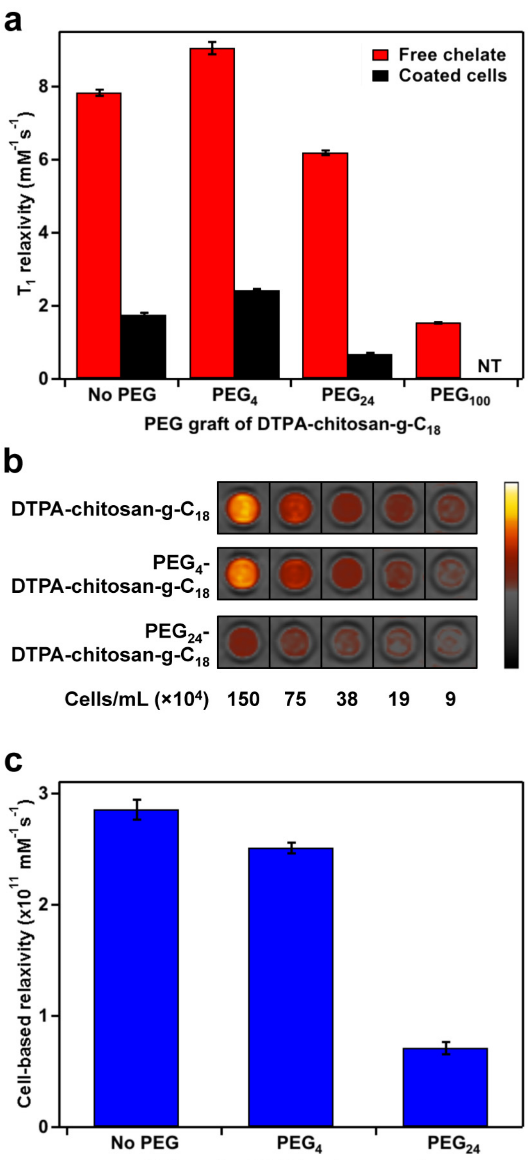

Figure 3.6 Relaxivity characterization of PEGylated chitosan fastener. (a) Molar relaxivity of modified chitosans loaded with gadolinium free in solution (red) and adsorbed to cells (black). NT designates the sample not tested, as free PEG$_{100}$-DTPA-chitosan-g-C$_{18}$ could not be purified from coated cells. (b) MR images of the chitosan fasteners at various cell concentrations (TI = 1000 ms). Pseudocoloring is proportional to signal intensity. (c) Relaxivities of chitosan fasteners normalized to cell concentration instead of gadolinium concentration. Error bars in all figures represent the standard deviation of the fit parameter.

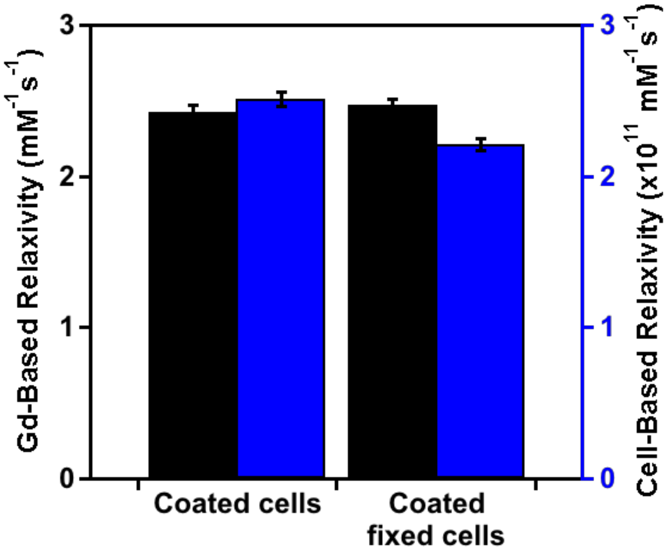

Figure 3.7 Cells fixed in formalin buffer prior to labeling produced similar Gd-based (shown in black) and cell-based (shown in blue) relaxivities as live cells after coating with PEG$_4$-DTPA-chitosan-g-C$_{18}$. Error bars are the standard deviation of the fit parameter.

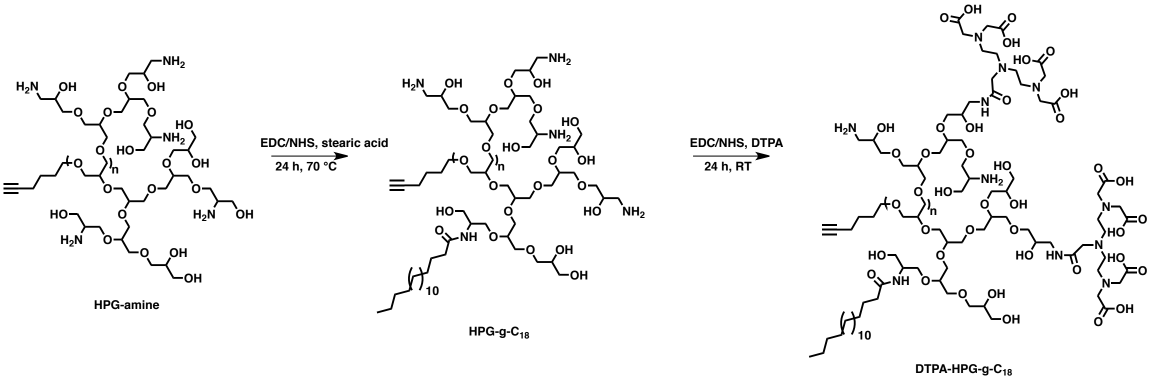

Figure 3.8 Synthesis of DTPA-HPG-g-C$_{18}$.

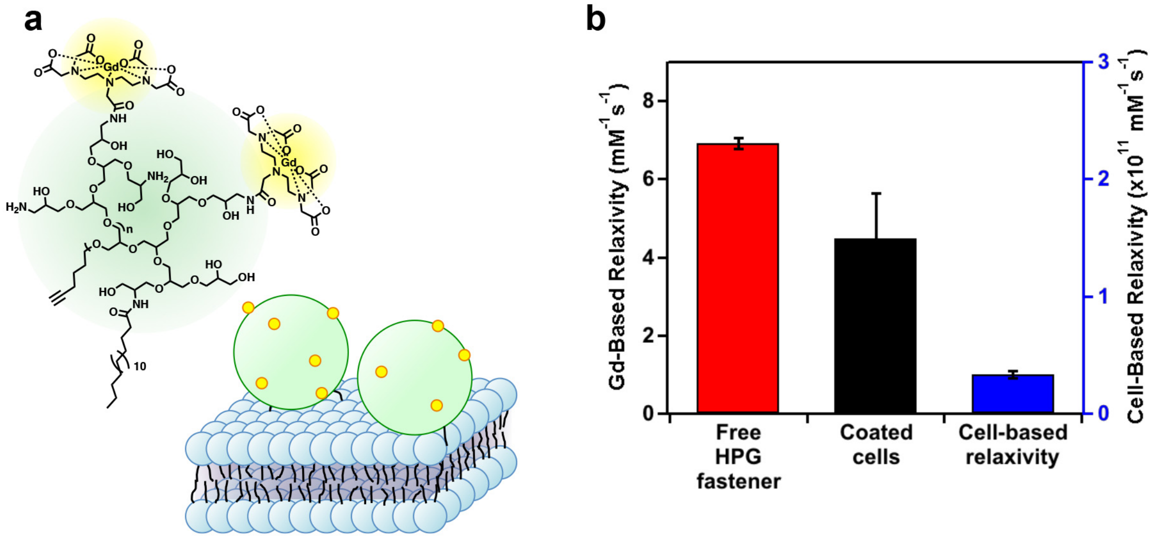

Figure 3.9 DTPA-HPG-g-C_{18} as a polymeric fastener for cell labeling. (a) Scheme depicting DTPA-HPG-g-C_{18} labeling the cell membrane. (b) Molar relaxivity of gadolinium-loaded HPG fastener free in solution (red) and adsorbed to BMSCs (black). The cell-based relaxivity (blue) was lower than that of the chitosan fasteners. Error bars represent standard deviation of the fit parameter.

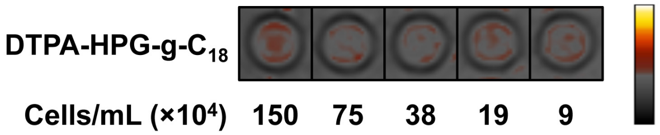

Figure 3.10 MR images of cells labeled by DTPA-HPG-g-C_{18} (TI = 1000 ms). Pseudocoloring is shown on the same scale as Figure 3.6b.

3.7 References

1. Segers, V. F. M.; Lee, R. T. Stem-Cell Therapy for Cardiac Disease. *Nature* **2008,** *451*, 937-942.

2. Strauer, B. E.; Brehm, M.; Zeus, T.; Kostering, M.; Hernandez, A.; Sorg, R. V.; Kogler, G.; Wernet, P. Repair of Infarcted Myocardium by Autologous Intracoronary Mononuclear Bone Marrow Cell Transplantation in Humans. *Circulation* **2002,** *106*, 1913-1918.

3. Nakagami, H.; Maeda, K.; Morishita, R.; Iguchi, S.; Nishikawa, T.; Takami, Y.; Kikuchi, Y.; Saito, Y.; Tamai, K.; Ogihara, T.*, et al.* Novel Autologous Cell Therapy in Ischemic Limb Disease through Growth Factor Secretion by Cultured Adipose Tissue-Derived Stromal Cells. *Atertio. Thromb. Vasc. Biol.* **2005,** *25*, 2542-2547.

4. Yee, C.; Thompson, J. A.; Byrd, D.; Riddell, S. R.; Roche, P.; Celis, E.; Greenberg, P. D. Adoptive T Cell Therapy Using Antigen-Specific $CD8^+$ T Cell Clones for the Treatment of Patients with Metastatic Melanoma: *In Vivo* Persistence, Migration, and Antitumor Effect of Transferred T Cells. *Proc. Natl. Acad. Sci.* **2002,** *99*, 16168-16173.

5. Leen, A. M.; Rooney, C. M.; Foster, A. E. Improving T Cell Therapy for Cancer. *Annu. Rev. Immunol.* **2007,** *25*, 243-265.

6. Hussain, M. A.; Theise, N. D. Stem-Cell Therapy for Diabetes Mellitus. *The Lancet* **2004,** *364*, 203-205.

7. Lagasse, E.; Connors, H.; Al-Dhalimy, M.; Reitsma, M.; Dohse, M.; Osborne, L.; Wang, X.; Finegold, M.; Weissman, I. L.; Grompe, M. Purified Hematopoietic Stem Cells Can Differentiate into Hepatocytes in Vivo. *Nat. Med.* **2000,** *6*, 1229-1234.

8. Rossi, F.; Cattaneo, E. Neural Stem Cell Therapy for Neurological Diseases: Dreams and Reality. *Nat. Rev. Neurosci.* **2002,** *3*, 401-409.

9. Lindvall, O.; Kokaia, Z. Stem Cells for the Treatment of Neurological Disorders. *Nature* **2006,** *441*, 1094-1096.

10. Lee, J.-P.; Jeyakumar, M.; Gonzalez, R.; Takahashi, H.; Lee, P.-J.; Baek, R. C.; Clark, D.; Rose, H.; Fu, G.; Clarke, J.*, et al.* Stem Cells Act through Multiple Mechanisms to Benefit Mice with Neurodegenerative Metabolic Disease. *Nat. Med.* **2007,** *13*, 439-447.

11. Ryan, E. A.; Paty, B. W.; Senior, P. A.; Bigam, D.; Alfadhli, E.; Kneteman, N. M.; Lakey, J. R. T.; Shapiro, A. M. J. Five-Year Follow-up after Clinical Islet Transplantation. *Diabetes* **2005,** *54*, 2060-2069.

12. Prockop, D. J.; Youn Oh, J. Mesenchymal Stem/Stromal Cells (MSCs): Role as Guardians of Inflammation. *Mol. Ther.* **2012,** *20*, 14-20.

13. Rehman, J.; Traktuev, D.; Li, J.; Merfeld-Clauss, S.; Temm-Grove, C. J.; Bovenkerk, J. E.; Pell, C. L.; Johnstone, B. H.; Considine, R. V.; March, K. L. Secretion of Angiogenic and Antiapoptotic Factors by Human Adipose Stromal Cells. *Circulation* **2004,** *109*, 1292-1298.

14. García, R.; Aguiar, J.; Alberti, E.; de la Cuétara, K.; Pavón, N. Bone Marrow Stromal Cells Produce Nerve Growth Factor and Glial Cell Line-Derived Neurotrophic Factors. *Biochem. Biophys. Res. Commun.* **2004,** *316*, 753-754.

15. Naumova, A. V.; Modo, M.; Moore, A.; Murry, C. E.; Frank, J. A. Clinical Imaging in Regenerative Medicine. *Nat. Biotechnol.* **2014,** *32*, 804-818.

16. Palestro, C. J.; Love, C.; Bhargava, K. K. Labeled Leukocyte Imaging: Current Status and Future Directions. *Q. J. Nucl. Med. Mol. Imaging* **2009,** *53*, 105-123.

17. Dumarey, N.; Egrise, D.; Blocklet, D.; Stallenberg, B.; Remmelink, M.; del Marmol, V.; Van Simaeys, G.; Jacobs, F.; Goldman, S. Imaging Infection with ^{18}F-FDG-Labeled Leukocyte PET/CT: Initial Experience in 21 Patients. *J. Nucl. Med.* **2006,** *47*, 625-632.

18. Massoud, T. F.; Gambhir, S. S. Molecular Imaging in Living Subjects: Seeing Fundamental Biological Processes in a New Light. *Genes Dev.* **2003,** *17*, 545-580.

19. Bulte, J. W.; Kraitchman, D. L. Monitoring Cell Therapy Using Iron Oxide MR Contrast Agents. *Curr Pharm Biotechnol* **2004,** *5*, 567-584.

20. Na, H. B.; Song, I. C.; Hyeon, T. Inorganic Nanoparticles for MRI Contrast Agents. *Adv. Mater.* **2009,** *21*, 2133-2148.

21. Tang, A. M.; Ananta, J. S.; Zhao, H.; Cisneros, B. T.; Lam, E. Y.; Wong, S. T.; Wilson, L. J.; Wong, K. K. Cellular Uptake and Imaging Studies of Gadolinium-Loaded Single-Walled Carbon Nanotubes as MRI Contrast Agents. *Contrast Media Mol. Imaging* **2011,** *6*, 93-9.

22. Guenoun, J.; Koning, G. A.; Doeswijk, G.; Bosman, L.; Wielopolski, P. A.; Krestin, G. P.; Bernsen, M. R. Cationic Gd-DTPA Liposomes for Highly Efficient Labeling of Mesenchymal Stem Cells and Cell Tracking with MRI. *Cell Transplant.* **2012,** *21*, 191-205.

23. Anderson, S. A.; Lee, K. K.; Frank, J. A. Gadolinium-Fullerenol as a Paramagnetic Contrast Agent for Cellular Imaging. *Invest. Radiol.* **2006,** *41*, 332-338.

24. Vuu, K.; Xie, J.; McDonald, M. A.; Bernardo, M.; Hunter, F.; Zhang, Y.; Li, K.; Bednarski, M.; Guccione, S. Gadolinium-Rhodamine Nanoparticles for Cell Labeling and Tracking via Magnetic Resonance and Optical Imaging. *Bioconjugate Chem.* **2005,** *16*, 995-999.

25. Kok, M. B.; Hak, S.; Mulder, W. J. M.; van der Schaft, D. W. J.; Strijkers, G. J.; Nicolay, K. Cellular Compartmentalization of Internalized Paramagnetic Liposomes Strongly Influences Both T_1 and T_2 Relaxivity. *Magn. Reson. Med.* **2009,** *61*, 1022-1032.

26. Smith, C. E.; Shkumatov, A.; Withers, S. G.; Yang, B.; Glockner, J. F.; Misra, S.; Roy, E. J.; Wong, C.-H.; Zimmerman, S. C.; Kong, H. A Polymeric Fastener Can Easily Functionalize Liposome Surfaces with Gadolinium for Enhanced Magnetic Resonance Imaging. *ACS Nano* **2013,** *7*, 9599-9610.

27. Smith, C. E.; Kong, H. Cross-Linkable Liposomes Stabilize a Magnetic Resonance Contrast-Enhancing Polymeric Fastener. *Langmuir* **2014,** *30*, 3697-3704.

28. Chen, S.-l.; Fang, W.-w.; Ye, F.; Liu, Y.-H.; Qian, J.; Shan, S.-j.; Zhang, J.-j.; Chunhua, R. Z.; Liao, L.-m.; Lin, S.*, et al.* Effect on Left Ventricular Function of Intracoronary Transplantation of Autologous Bone Marrow Mesenchymal Stem Cell in Patients with Acute Myocardial Infarction. *Am. J. Cardiol.* **2004,** *94*, 92-95.

29. Orlic, D. Adult Bone Marrow Stem Cells Regenerate Myocardium in Ischemic Heart Disease. *Ann. N.Y. Acad. Sci.* **2003,** *996*, 152-157.

30. Chen, J.; Li, Y.; Wang, L.; Zhang, Z.; Lu, D.; Lu, M.; Chopp, M. Therapeutic Benefit of Intravenous Administration of Bone Marrow Stromal Cells after Cerebral Ischemia in Rats. *Stroke* **2001,** *32*, 1005-1011.

31. Kojima, C.; Turkbey, B.; Ogawa, M.; Bernardo, M.; Regino, C. A.; Bryant, L. H., Jr.; Choyke, P. L.; Kono, K.; Kobayashi, H. Dendrimer-Based MRI Contrast Agents: The Effects of PEGylation on Relaxivity and Pharmacokinetics. *Nanomedicine* **2011,** *7*, 1001-1008.

32. Kainthan, R. K.; Janzen, J.; Levin, E.; Devine, D. V.; Brooks, D. E. Biocompatibility Testing of Branched and Linear Polyglycidol. *Biomacromolecules* **2006,** *7*, 703-709.

33. Imran ul-haq, M.; Lai, B. F.; Chapanian, R.; Kizhakkedathu, J. N. Influence of Architecture of High Molecular Weight Linear and Branched Polyglycerols on Their Biocompatibility and Biodistribution. *Biomaterials* **2012,** *33*, 9135-47.

34. Jeong, J. H.; Schmidt, J. J.; Kohman, R. E.; Zill, A. T.; DeVolder, R. J.; Smith, C. E.; Lai, M.-H.; Shkumatov, A.; Jensen, T. W.; Schook, L. G.*, et al.* Leukocyte-Mimicking Stem Cell Delivery via in Situ Coating of Cells with a Bioactive Hyperbranched Polyglycerol. *J. Am. Chem. Soc.* **2013,** *135*, 8770-8773.

35. Zill, A.; Rutz, A. L.; Kohman, R. E.; Alkilany, A. M.; Murphy, C. J.; Kong, H.; Zimmerman, S. C. Clickable Polyglycerol Hyperbranched Polymers and Their Application to Gold Nanoparticles and Acid-Labile Nanocarriers. *Chem. Commun.* **2011,** *47*, 1279-1281.

CHAPTER 4

HYDROPHILIC PACKAGING OF IRON OXIDE NANOCLUSTERS FOR HIGHLY SENSITIVE IMAGING

Acknowledgments

The research described in this chapter was conducted through several collaborative efforts. Polyglycerol synthesis and characterization was performed by Dawn Ernenwein and JuYeon Lee, including Figures 4.17-4.26 produced by Dawn Ernenwein. Animal studies were performed by Artem Shkumatov and Molly Melhem, and Nicholas Clay synthesized oleic acid-capped SPIONs. Additionally, the magnetization curve in Figure 4.8 was acquired with assistance from Juan Atkinson in the laboratory of Dale Van Harlingen. I would also like to thank Boris Odintsov and Ryan Larsen at the Beckman Institute for Advanced Science and Technology for assistance with MR imaging. Mass spectral and iron content analyses were provided by the School of Chemical Sciences Mass Spectrometry Laboratory and Microanalysis Laboratory respectively, and I performed TEM and DLS measurements in the Frederick Seitz Materials Research Laboratory Central Facilities at the University of Illinois. The illustrations shown in Figures 4.13a and 4.15a were provided by the School of Chemical Sciences Graphic Services.

4.1 Introduction

Magnetic resonance imaging (MRI) generates high-resolution images non-invasively and therefore is used for diagnosis of various tissue defects[1,2] as well as evaluation of fluid flows within engineered materials and devices.[3-5] The diagnostic capability of MRI has been greatly enhanced with the introduction of superparamagnetic iron oxide nanoparticles (SPIONs), which can provide negative contrast against surrounding tissues. To further enhance their utility, SPIONs that have increased relaxivity while localizing at sites of interest would be advantageous for improving the capabilities of MRI. An attractive method to accomplish this is to tailor particle size within a range for which relaxivity is maximized, known as the static dephasing regime (SDR).[6] However, SPIONs with diameters approaching such an optimal size often become permanently magnetic,[7] resulting in uncontrolled aggregation that diminishes relaxivity and substantially reduces the SPION's ability to reach target sites. Assembling SPIONs in the form of clusters has emerged as a promising strategy to yield a desired size of metallic core while maintaining superparamagnetism and colloidal stability.[8-14] A limitation of common approaches, however, lies in the SPION coating material used to induce clustering, as such materials may limit penetration of water near the metallic core or reduce hydrophilic interactions. Such factors are intrinsically detrimental since the effectiveness of an MR contrast agent is highly dependent on its ability to interact with surrounding water.[15]

In this study, we hypothesized that the globular nature of a hydrophilic, hyperbranched polymer would allow for maximal MR relaxivity of clustered SPIONs to improve the diagnostic capability of *in vivo* imaging of ischemic tissue. To test this hypothesis, SPIONs were coated by a hyperbranched polyglycerol substituted with a varying number of octadecyl chains (HPG-g-C_{18}) to form the nanoclusters (Figure 4.1). Hyperbranched polyglycerol was adopted to mimic the structure of glycogen, a natural, hyperbranched biopolymer that is able to hold 2-3 times its weight in water.[16] The critical role of the polyglycerol molecular architecture in enhancing relaxivity of SPION clusters was addressed using the analogous linear polyglycerol substituted with octadecyl chains as a control. The ability of the resultant ultrasensitive nanocluster to identify ischemic tissue vascularized with leaky blood vessels was then evaluated in a murine model of hindlimb ischemia.[17]

4.2 Results

4.2.1 Synthesis and characterization of hyperbranched and linear polyglycerols

First, hyperbranched polyglycerol (HPG) was synthesized by one-step anionic ring-opening polymerization of glycidol (Figure 4.2a). Further reaction of HPG with octadecyl bromide yielded HPG with a molecular weight of 3 kg/mol substituted with an average of 5 alkyl chains per polymer, termed HPG_{3k}-g-C_{18}(5), according to NMR and mass spectrometry (Spectroscopy data is shown at the end of the chapter). The control, linear polyglycerol (LPG) with a molecular weight of 3 kg/mol was synthesized through a three-step process in which glycidol was reacted with ethyl vinyl ether to form ethoxy ethyl glycidyl ether, which was then polymerized and finally hydrolyzed to yield LPG (Figure 4.2b). Subsequent alkylation of the resultant LPG_{3k} yielded LPG_{3k}-g-C_{18}(2), with an average of 2 octadecyl chains per polymer. Despite having similar molecular weights and chemical functionalities, the hyperbranched architecture of HPG resulted in a smaller contact angle than the LPG (Figure 4.3). The corresponding surface energy of the HPG film was more than 30% greater. The result indicates that coating of SPION clusters with HPG would be advantageous in facilitating interaction with surrounding water.

4.2.2 Comparison of nanoclusters assembled with alkylated HPG_{3k} and LPG_{3k}

Emulsification of 5 nm-diameter oleic acid-capped SPIONs initially dispersed in chloroform and polyglycerol dissolved in water resulted in spherical SPION clusters that were stable in water (Figures 4.4a and 4.4b), as confirmed with transmission electron microscopy (TEM) (Figure 4.4c). While the *Z*-average hydrodynamic diameter determined by dynamic light scattering (DLS) was 80 nm regardless of polyglycerol molecular architecture, the average core size of the HPG_{3k}-g-C_{18}(5) clusters measured with TEM was 42±9 nm, and that of the LPG_{3k}-C_{18}(2)-induced clusters was 60±13 nm. This indicates that HPG_{3k}-g-C_{18}(5) provides a thicker hydrated polymer coating layer. In both cases, SPION clusters remained dispersed for over one year. Relaxivity measurements were performed on the nanoclusters to determine effects of the hyperbranched structure on T_2 relaxation (Figure 4.4d). Despite having the same hydrodynamic size, nanoclusters coated by HPG_{3k}-g-C_{18}(5) had a relaxivity 30% higher than clusters made with LPG_{3k}-g-C_{18}(2), likely due to differences in hydrophilicity as a result of branching, as well as coating thickness.

4.2.3 Tuning cluster size

Next, the size of the nanoclusters was tuned within the SDR, commonly centered on a diameter of 120 nm.[18] Size has been shown to vary with polymer content during fabrication,[19-22] however, clusters made with HPG_{3k}-g-C_{18}(5) or LPG_{3k}-g-C_{18}(2) remained 80 nm, regardless of concentration (Figure 4.5), with core diameters of approximately 40 nm and 60 nm respectively. To strengthen potential HPG-mediated inter-droplet interactions,[23] a larger HPG with a molecular weight of 50 kg/mol, termed HPG_{50k}, was synthesized by increasing the ratio of glycidol-to-initiator in the polymerization reaction.

The resulting HPG was alkylated at two levels to yield HPG_{50k}-g-C_{18}(2) and HPG_{50k}-g-C_{18}(10), in which two and ten alkyl chains were conjugated to the HPG_{50k} respectively. For these polymers, the hydrodynamic diameter of the nanoclusters was indeed tunable with HPG content (Figure 4.6), with average diameters increasing to a critical size of approximately 145 nm. TEM images of SPION clusters also verified that the diameter of the clustered metallic core was tailored with HPG_{50k}-g-C_{18}, following the same trends as the hydrodynamic diameter measured with DLS.

4.2.4 Relaxivity characterization of HPG-SPION nanoclusters

MR relaxivity of nanoclusters coated by alkylated HPG_{50k} displayed the size-dependent behavior, characterized by an initial increase in relaxivity followed by decrease with larger sizes (Figure 4.7). Additionally, for any given size, the more highly alkylated HPG (i.e., HPG_{50k}-g-C_{18} (10)) led to reduced relaxivity (Figure 4.7a). As such, tuning the diameter of SPION nanoclusters coated with HPG_{50k}-g-C_{18}(2) led to a relaxivity of 719 $mM^{-1}s^{-1}$ (Figure 4.7b). This relaxivity was close to the theoretical maximum for the SPIONs used, which was determined to be 742 $mM^{-1}s^{-1}$ based on magnetic saturation (Figure 4.8).

According to phantom images, the HPG-SPIONs with a relaxivity of 719 $mM^{-1}s^{-1}$ provided high contrast against background at low iron levels, unlike unclustered SPIONs with measured relaxivity of 122 $mM^{-1}s^{-1}$ (Figure 4.9). The nanoclusters completely dephased the water proton signal at an iron concentration of 0.14 mM, whereas unclustered SPIONs at the same concentration provided no noticeable contrast.

4.2.5 In vitro nanocluster assays

The SPION nanoclusters minimally influenced metabolic activity of C166 endothelial cells, even at high doses of 580 μg Fe/mL (Figure 4.10). Furthermore, the ability of the clusters to penetrate an inflamed endothelium as a method of passive targeting was simulated using a transwell system (Figure 4.11). The migration of clusters through an endothelial monolayer was greatly enhanced after incubating the cells with tumor necrosis factor (TNF)-α, a proinflammatory cytokine.[24] SPION nanoclusters also remained intact during incubation in serum, thus supporting their stable structural integrity in blood circulation (Figure 4.12).

4.2.6 In vivo models of ischemia

Finally, the engineered HPG-SPIONs were used to evaluate their capacity to accumulate in and identify ischemic tissue *in vivo* following systemic injection. Ligation of the femoral artery resulted in inflammation and local tissue damage typical of ischemic wounds. HPG-SPIONs injected systemically via tail vein were able to dramatically reduce MR signal in the injured region of the hindlimb at a dose of 2 mg Fe/kg, which is 5 to 10 fold lower than those used in similar studies[25-27] (Figure 4.13). In contrast, the unclustered SPIONs provided minimal enhancement, despite a comparable amount of iron accumulated in the target tissue as verified with Prussian blue staining (Figure 4.14). Similarly, in a model of coronary ischemia induced by ligation of coronary artery, HPG-SPIONs administered through the tail vein were able to locally highlight damaged cardiac tissue, whereas unclustered SPIONs no observable contrast effect (Figure 4.15). Again, according to Prussian blue staining, no significant difference of iron accumulation in target tissue was found (Figure 4.16). Therefore, the enhanced contrast of MR images is attributed to the high relaxivity of HPG-SPION nanoclusters.

4.3 Discussion

In summary, this study demonstrates that HPG creates SPION clusters with very high relaxivity due to control of cluster size coupled with optimization of hydrophilicity at the surface. We propose that the thick, hydrophilic HPG coating layer serves to enhance relaxivity by absorbing water and reducing its diffusivity,[28] analogous to the way the multi-branched polysaccharide, glycogen, interacts with and retains water via its molecular architecture and extensive hydrogen bonding. In this way, this study presents a first time investigation into the effects of molecular architecture of the packaging material on performance of the SPIONs. Such hydrophilic coatings may also be applied to improving nanoparticles of varying size and composition, and is thus broadly applicable in contrast agent design.

4.4 Conclusion

The formulated HPG-SPION nanoclusters can identify tissue defects using MRI, and therefore have potential to diagnose a wide variety of vascular diseases, which remain the leading cause of death worldwide. For further improvement, the HPG could easily be modified with targeting moieties to actively bind nanoclusters to sites of interest. Furthermore, as the inflammation that induces leaky vasculature occurs during initial stages of diseases, the HPG-coated SPION clusters may represent an early detection system for some of the most significant diseases worldwide, not only for cardiovascular disease, but also cancer.

4.5 Materials and Methods

4.5.1 General polyglycerol characterization methods

Mass spectral analysis was performed using ESI on a Waters Micromass Q-Tof spectrometer or MALDI-TOF on an Applied Biosystems Voyager-DE STR spectrometer. Nuclear magnetic resonance (NMR) spectra were recorded on a Varian U400, UI400, U500 or

VXR500 spectrometer. Additionally, the molecular weights of HPGs were evaluated by gel permeation chromatography (GPC, Waters Breeze 2) with a Styragel HT column. 20 mM LiBr in *N,N*-dimethylformamide (DMF) was used as an eluent. Values were based on calibration against polyethylene glycol (PEG) standards. NMR, GPC, and mass spectral data for all synthesized materials are shown in Figures 4.17-4.26.

4.5.2 Synthesis of HPG

All materials were purchased from Sigma-Aldrich unless otherwise noted. The overall synthetic scheme is shown in Figure 4.2 and generally follows the methods reported by Kong, Zimmerman, and coworkers.[29] To prepare HPG, sodium hydride (NaH) was mixed with the alkyne initiator, 4-pentyn-1-ol at a 1:10 molar ratio. The mixture was stirred for 15 min followed by addition of doubly distilled glycidol by a syringe pump (1.2 mL/h) while stirring at 70 ºC. The molar ratio of glycidol to initiator was varied to achieve different molecular weights. After addition, the reaction continued for 3 h with constant stirring. For each 1 mL of glycidol used, 2 mL of methanol was added and ion exchange Amberlite IR 1200 H form prewashed resin were added to the polymer solution and stirred for 1 h at 50 °C. The resin was removed by vacuum filtration and the polymer was fractionally precipitated with cold ether and centrifuged at 4,000 rpm for 15 min at 4 °C. The supernatant was decanted and precipitation was repeated 2-3 more times. The resulting HPGs were characterized by mass spectrometry, ^{1}H NMR, and ^{13}C NMR.

4.5.3 Alkylation of HPG

HPG (40 mg, 0.005 mmol) was dissolved in anhydrous dimethylformamide (DMF, 2.5 mL) to which NaH in 60% mineral oil (7.6 mg, 0.19 mmol) was added. The solution was stirred for 15 min before addition of bromooctadecane (63.3 mg, 0.19 mmol). The average number of conjugated alkyl chains was controlled by varying the ratio of bromooctadecane to HPG. The reaction mixture was then placed in a preheated oil bath at 80 °C for 24 h. The mixture was extracted with hexane 3 times to remove unreacted bromide and the DMF was removed first by rotary evaporator and then under high vacuum. The material was characterized by MALDI-TOF, ^{1}H NMR and ^{13}C NMR.

The degree of substitution of alkyl chain (DS_{C18}) on alkylated HPG was calculated from the integrated peaks of the ^{1}H NMR spectra as follows in Eq. (4.1):

$$DS_{C18} = \frac{\left(Peak_{1.3}/30\right)}{\left(Peak_{4.0-3.4}/5\right)-\left(Peak_{1.3}/30\right)} \times 100\% \tag{4.1}$$

*4.5.4 Synthesis of the LPG intermediate, ethyl glycidol ether (EEGE) (**3** in Figure 4.2b)*

Freshly distilled glycidol was added to ethyl vinyl ether at a molar ratio of 0.8:3 and cooled to 0 °C. p-Toluene sulfonic acid monohydrate (pTSA) was added slowly while keeping the temperature below 20 °C. The mixture was then warmed to room temperature and stirred for 3 h. Saturated $NaHCO_3$ was added and the organic layer was dried over Na_2SO_4. Solvent was removed under vacuum and the product was stored with CaH and vacuum distilled at 50 °C. The product was characterized by ^{1}H NMR, ^{13}C NMR, and electrospray ionization (ESI) mass spectrometry on a Waters Micromass Q-Tof spectrometer.

*4.5.5 Synthesis of the LPG intermediate, poly(EEGE) (**5** in Figure 4.2b)*

Using a slightly modified literature procedure,[30,31] 2.1 mmol of 4-pentyn-1-ol (0.2 mL) was added to 15 mL freshly distilled diglyme, followed by 0.2 mL of a 1 M solution of potassium tert-butoxide in THF and stirred for 10 min. The flask was then cooled to -50 °C prior to dropwise addition of EEGE (92 mL, 725 mmol). The reaction continued for 48 h at 120 °C. Diglyme was removed by vacuum distillation at 80 °C, and the remaining product was dissolved in dichloromethane (DCM) and washed with water. The organic phase was dried over anhydrous sodium carbonate, and the solvent was removed using a rotary evaporator. The product was characterized by MALDI-TOF, ^{1}H NMR, and ^{13}C NMR.

4.5.6 Synthesis and alkylation of LPG

First, poly(EEGE) was dissolved in THF, followed by addition of 32% HCl aqueous solution, which resulted in precipitation of LPG. The reaction continued for 2 h before the solvent was decanted and the residue was washed twice with THF, followed by solvent removal under vacuum. Next, as in the alkylation of HPG, LPG was dissolved in anhydrous DMF and reacted with bromooctadecane in the presence of NaH to yield LGP_{3k}-g-C_{18}(2). The products were characterized by MALDI-TOF, ^{1}H NMR and ^{13}C NMR. DS_{C18} was determined with Eq. (4.1), as in the case of alkylated HPG.

4.5.7 Contact angle measurement of HPG and LPG

HPG_{3k} or LPG_{3k} was dissolved in a 1:1 water and acetone mixture and spin coated on glass cover slides to make a thin, even film using a VTC-100 vacuum spin coater (MTI Corporation). A droplet of deionized water was placed on the film, and the contact angle was measured by a contact angle goniometer (Rame-Hart). The surface energies of the polyglycerol films, W, were calculated from the contact angle, θ, using the Young-Dupre Eq. (4.2) and the surface tension of water, γ:

$$W = \gamma\left(1 + \cos\theta\right) \tag{4.2}$$

4.5.8 Synthesis of oleic acid-capped SPIONs

5 nm-diameter oleic acid-capped SPIONs were synthesized by thermal decomposition of iron acetylacetonate, as previously described.[32,33] Briefly, iron acetylacetonate (2 g), oleylamine (660 μL), oleic acid (660 μL), and 1,2 dodecanediol (0.7 g) were dissolved in 6.7 mL of benzyl ether. The mixture was heated under nitrogen to 200 °C for 2 h, followed by reflux at 300 °C for 1 h. SPIONs were purified by precipitation in ethanol, magnetic separation, and finally re-dispersion in chloroform at a concentration of 10 mg/mL.

4.5.9 Analysis of magnetization of SPIONs

The field-dependent magnetization of the SPIONs was evaluated with a vibrating sample magnetometer (MPMS, Quantum Design). Iron concentration was determined by digestion of SPIONs in concentrated nitric acid followed by analysis with inductively coupled plasma optical emission spectroscopy (ICP-OES, Perkin-Elmer Optima 2000 DV). The saturation magnetization acquired with the MPMS was used to estimate the theoretical maximum relaxivity within the static dephasing regime (SDR) using Eq. (4.3):

$$r_2 = \frac{2\pi\gamma\mu_0 v M_s}{9\sqrt{3}} \tag{4.3}$$

where γ is here defined as the proton gyromagnetic ratio, μ_0 is the permeability of free space, υ is the molar volume, and M_s is the saturation magnetization. With a saturation magnetization of 71 emu/g (Figure 4.8), the maximum relaxivity for such SPIONs yielded the value of 742 $mM^{-1}s^{-1}$.

4.5.10 Fabrication of polyglycerol-coated SPION nanoclusters

SPION clusters were fabricated by emulsification. The aqueous phase was prepared by dissolving HPG-g-C_{18} or LPG-g-C_{18} in deionized water at varying concentrations. SPIONs dispersed in chloroform were added to the PG aqueous solution, and the mixtures were immediately sonicated (Fisher Scientific Sonic Dismembrator, Model 100). Chloroform was then removed by rotary evaporation (Heidolph Hei-VAP), and excess material was removed by centrifugation. Performance of HPG-SPIONs was compared to the unclustered SPION, FeREX (BioPAL, Inc.).

4.5.11 Size determination of nanoclusters

The Z-average hydrodynamic diameters of the nanoclusters were determined by dynamic light scattering (DLS, Malvern Zetasizer Nano). TEM micrographs were obtained by JEOL 2100 cryo TEM at 200 kV, with samples dried on holey carbon-coated copper grids. To demonstrate stability in serum, HPG-SPIONs were incubated for 2 h at 37 °C in phosphate buffered saline (PBS) supplemented with 50% type AB human serum off the clot (PAA Laboratories Inc.) prior to grid preparation. For certain experiments, the cryo-TEM sample was applied to a lacey carbon-coated copper grid and prepared by cryo plunge (FEI vitrobot) into liquid ethane (~90 K) in a controlled environment at 23 ºC and 100% humidity. The images were acquired using JEOL

2100 cryo TEM with a cryogenic sample holder (Gatan 626) at 60 kV with digital imaging. Cluster core size was determined from a minimum of 50 clusters using ImageJ software.

4.5.12 T_2 relaxivity measurement of SPION contrast agents

MR phantoms of SPIONs were prepared in borosilicate culture tubes, which were immobilized in an agar gel. Imaging was performed with a 3 T Siemens Magnetom Trio scanner equipped with head coil. Images were acquired using a spin echo sequence with repetition time (TR) of 1200 ms and echo time (TE) varied from 12 to 490 ms to determine spin-spin relaxation time (T_2) by nonlinear least-squares curve fitting to Eq. (4.4):

$$S(\mathrm{TE}) = S_0\,\mathrm{e}^{-\mathrm{TE}/T_2} + b \tag{4.4}$$

where $S(\mathrm{TE})$ is the average signal intensity for echo time (TE) taken over the coronal section area of the MR phantom by ImageJ software, S_0 represents the steady state signal intensity, and b is an offset due to the background noise level. Transverse molar relaxivity (r_2) was then determined by linear regression of Eq. (4.5):

$$1/T_2 = 1/T_{2,\mathrm{water}} + r_2[\mathrm{Fe}] \tag{4.5}$$

in which $1/T_{2,\mathrm{water}}$ is the relaxation rate of water and [Fe] is the iron concentration within the phantom sample. Iron concentration was determined by ICP-OES (Perkin-Elmer Optima 2000 DV) after digestion in concentrated nitric acid.

4.5.13 MTT assay for cellular metabolic activity

C166 endothelial cells were seeded at a density of 5×10^3 cells per well in a 96-well plate. Cells were incubated for 24 h with SPION clusters coated with $\mathrm{HPG_{50k}}$-g-$\mathrm{C_{18}}$(2). MTT reagent ((3-(4,5-dimethylthiazol-2-yl)-2,5-diphenyltetrazolium bromide, ATCC) was then added, followed by addition of MTT detergent, and absorbance at 570 nm was measured with a plate reader (Tecan Infinite 200 PRO) as an indicator of metabolic activity.

4.5.14 Transwell migration assay

The setup, shown schematically in Figure 4.11, consisted of an HTS Transwell 96-well plate with 8 μm diameter pores in a polyester membrane (Corning). C166 endothelial cells were seeded on the transwell insert at a density of 1×10^5 cells per well to form an endothelial layer according to the manufacturer's protocol. To compare physiological to inflamed states, cells were incubated overnight with a 10 ng/mL solution of tumor necrosis factor alpha (TNF-α, GenScript Corporation) to induce an inflammatory condition. Cells were then incubated for 1 h with FITC-labeled HPG-SPIONs, and fluorescence intensity of the receiver well was measured with a plate reader (Tecan Infinite 200 PRO) at excitation of 458 nm and emission at 535 nm as an indication of the clusters' ability to permeate the endothelial layer.

4.5.15 Hindlimb ischemia model

Hindlimb ischemia was induced in male BALB/c mice (Jackson Laboratories, ME) in accordance with the protocol approved by the Illinois Institutional Animal Care and Use Committee. Mice were anesthetized by intraperitoneal injection of a mixture of xylazine (10 mg/kg) and ketamine hydrochloride (100 mg/kg). A small incision was made on the upper thigh of the left hindlimb and the femoral artery was ligated in two regions with 5-0 Ethilon sutures (Johnson and Johnson, NJ). The artery was then severed between the proximal and distal sutures. The ischemic injury developed over 24 h, at which point SPIONs were injected via tail vein at a dose of 2 mg Fe/kg.

4.5.16 Coronary ischemia model

Procedures to induce coronary ischemia in female C57BL/6J mice (Jackson Laboratories, ME) were performed according to the protocol approved by the Illinois Institutional Animal Care and Use Committee. Mice were first anesthetized with 5% isofluorane delivered with 1 L/min oxygen in an anesthetic chamber. Mice were then intubated with a 20G angiocath tube and exposed to 1.5% isofluorane with 1 L/min oxygen during the surgical procedure. A one-inch incision was then made vertically and two muscle layers were retracted and sutured in place. To expose the heart, an intercostal incision was then made between the 3rd and 4th ribs. To induce occlusive blood flow, the left coronary artery was ligated with an 8-0 monofilament suture (Johnson and Johnson, NJ). Finally, the incisions were closed using a 6-0 monofilament suture (Johnson and Johnson, NJ). The myocardial infarction developed over 24 h, and SPIONs were injected via tail vein at a dose of 2 mg Fe/kg as in the hindlimb ischemia study.

4.5.17 In vivo MRI

For both models of murine ischemia, mice were imaged 3 h after contrast agent injection with a Varian 14.1 T microimager consisting of a Unity/Inova 600 MHz NMR spectrometer and adjustable radiofrequency coil. Images were acquired using a spin-echo multislice (SEMS) pulse sequence with TR = 500 ms for hindlimb images or 600 ms for the heart model, TE = 20 ms, slice thickness = 0.5 mm, and matrix size = 256 x 256. Coronal images were acquired for the hindlimb model, while transverse sections were used for evaluation of the myocardial infarction model.

4.5.18 Histological analysis

Tissues of interest of the mice were fixed in 10% buffered formalin and embedded in paraffin. Tissues were cut at a 4 µm thickness using a Leica RM 2255 rotary microtome and the cross-sections were stained with Hematoxylin and Eosin or Prussian blue stain to analyze tissue morphology and locate SPIONs, respectively. Tissue sections were visualized with a NanoZoomer Slider Scanner/Digital Pathology System (Hamamatsu).

4.6 Figures

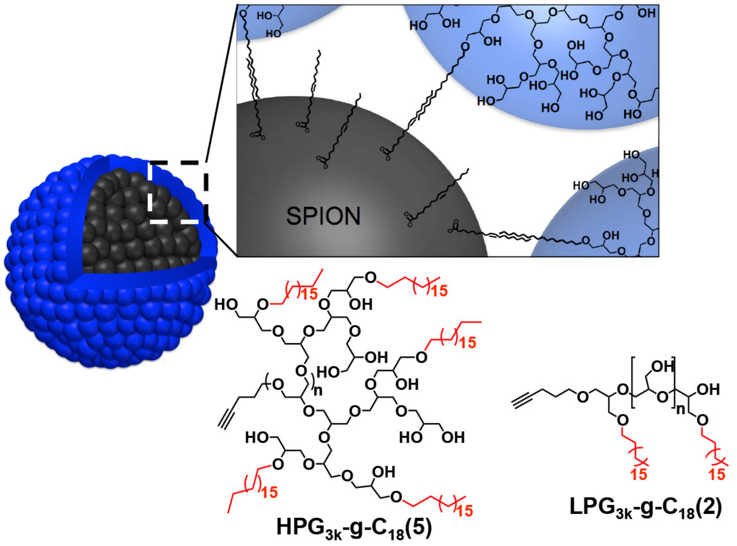

Figure 4.1 Overall scheme of hyperbranched polyglycerol-coated SPION nanoclusters and representative chemical structures of HPG_{3k}-g-C_{18}(5) and LPG_{3k}-g-C_{18}(2).

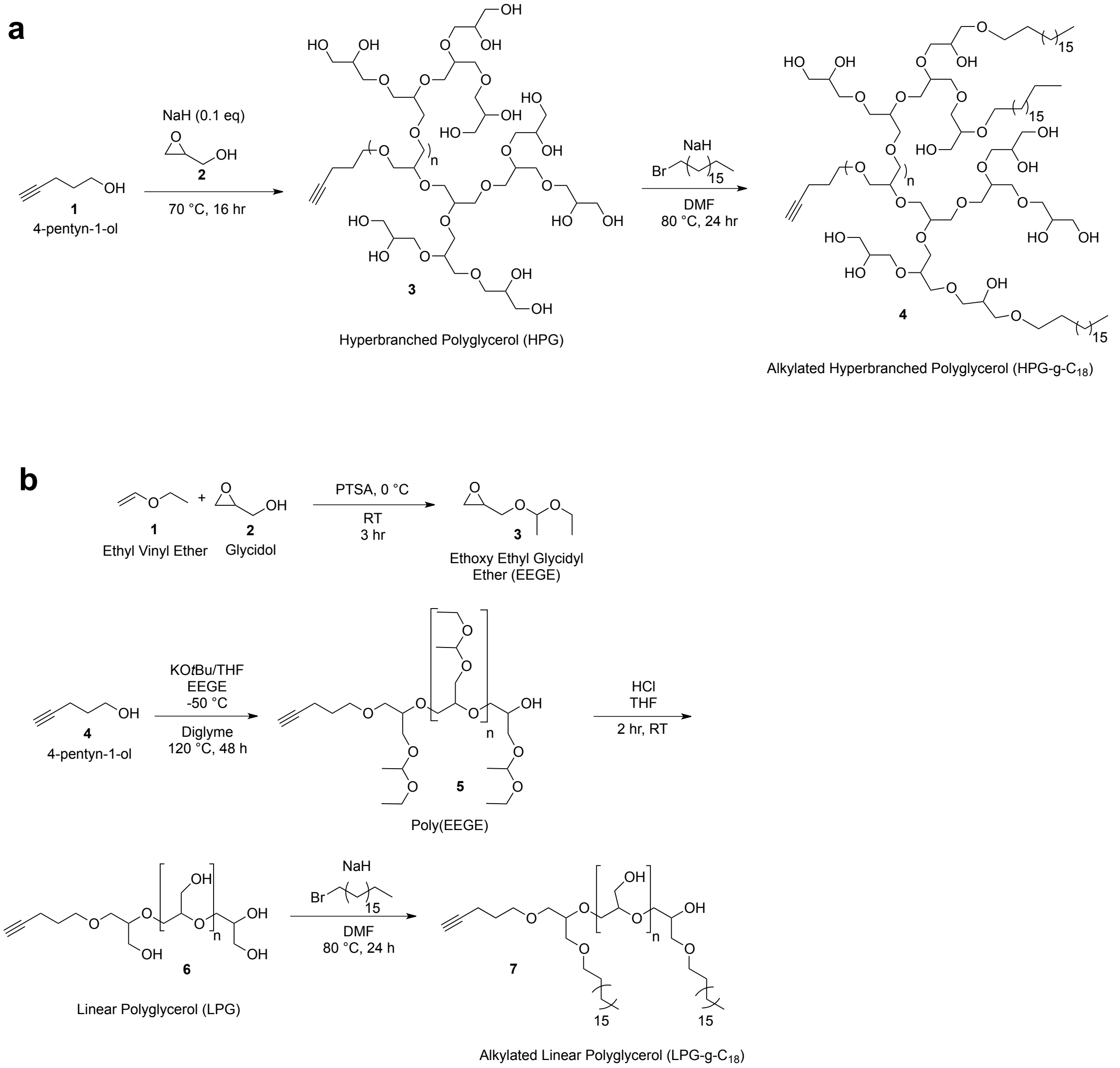

Figure 4.2 Synthesis of (a) alkylated HPG and (b) alkylated LPG.

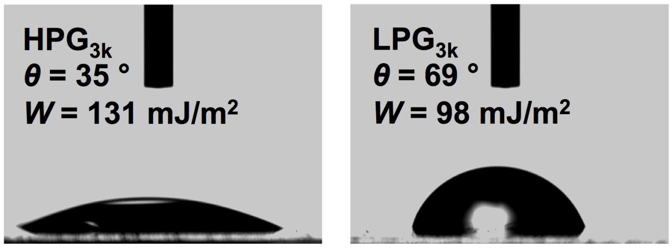

Figure 4.3 Contact angles and corresponding surface energies of water droplets on films of HPG_{3k} and LPG_{3k}.

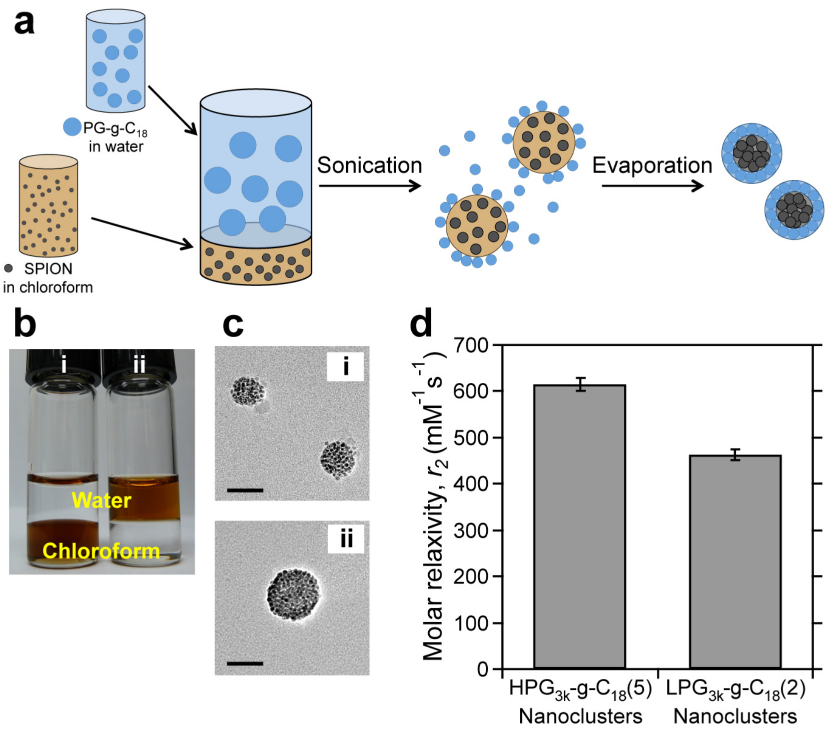

Figure 4.4 HPG-SPION clusters. (a) Schematic of the emulsification process to create polyglycerol-coated SPIONs. (b) Oleic acid-capped SPIONs were dispersed in (i) chloroform before emulsification and in (ii) water after emulsification. (c) TEM micrographs of SPIONs coated with (i) HPG_{3k}-g-C_{18}(5) and (ii) LPG_{3k}-g-C_{18}(2). Scale bars represent 50 nm. A minimum of 50 clusters were examined per condition. (d) Effect of molecular architecture on T_2 relaxivity. Error bars represent standard deviation of the fit parameter.

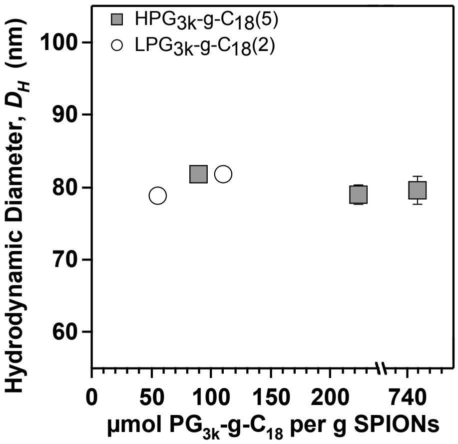

Figure 4.5 Z-average hydrodynamic diameter of SPION nanoclusters produced by various concentrations of HPG$_{3k}$-g-C$_{18}$(5) (■) and LPG$_{3k}$-g-C$_{18}$(2) (○). HPG$_{3k}$-g-C$_{18}$(5) and LPG$_{3k}$-g-C$_{18}$(2) represent HPG substituted with 5 C$_{18}$ chains and LPG substituted with 2 C$_{18}$ chains, respectively. Molecular weights of both HPG and LPG were 3,000 g/mol. Error bars, though partially obscured by data point markers, represent standard deviation of three measurements.

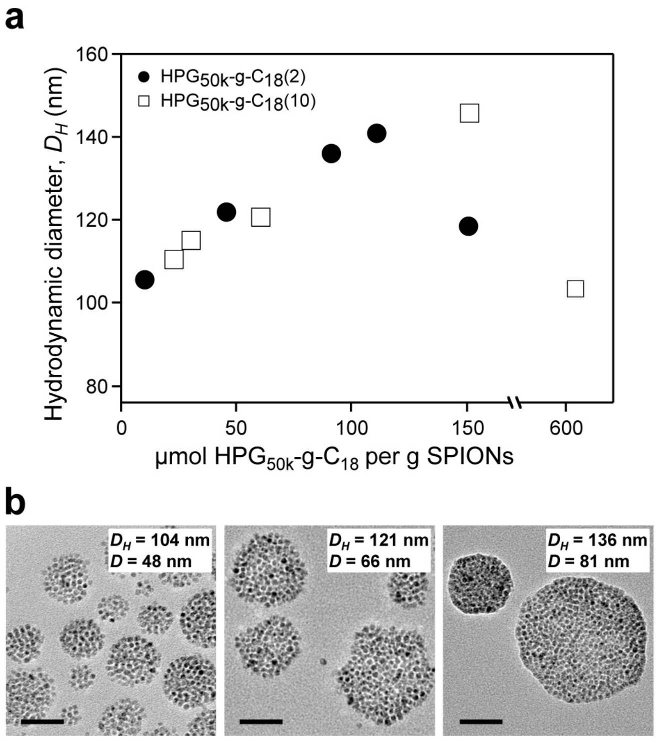

Figure 4.6 Controlling size of SPION nanoclusters with high molecular weight HPG. (a) Control of Z-average hydrodynamic diameter (D_H) by varying the concentration of HPG_{50k}-g-C_{18}(2) (●) and HPG_{50k}-g-C_{18}(10) (□) per SPION, where HPG_{50k}-g-C_{18}(2) and HPG_{50k}-g-C_{18}(10) represent HPG_{50k} substituted with 2 and 10 C_{18} chains, respectively. Data are the average of three replicate measurements, with error bars representing standard deviation obscured by data point markers. (b) Representative TEM micrographs of SPION nanoclusters with corresponding hydrodynamic diameter (D_H) determined from DLS and average core diameter (D) measured from a minimum of 50 clusters by TEM. Scale bars represent 50 nm.

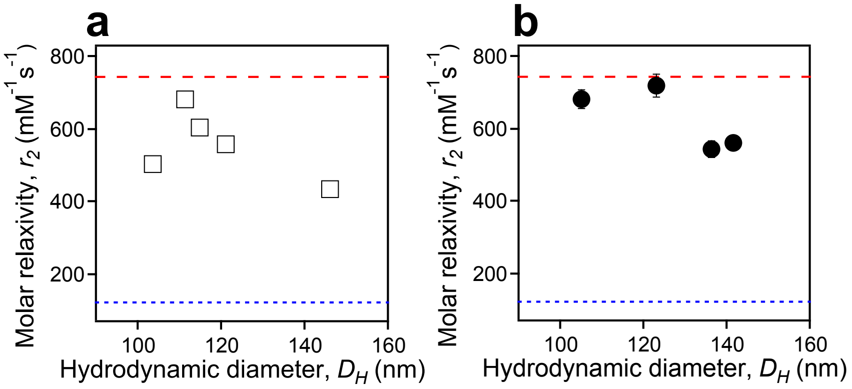

Figure 4.7 Tuning relaxivity with cluster size. Dependence of T_2 relaxivity (r_2) on the hydrodynamic diameter (D_H) of SPION clusters coated with (a) HPG_{50k}-g-C_{18}(10) and (b) HPG_{50k}-g-C_{18}(2). The upper limit red dashed line represents the maximum theoretical relaxivity of the SPIONs at 742 mM^{-1}s^{-1}, while the lower blue dotted line at 122 mM^{-1}s^{-1} is the relaxivity of unclustered, commercial SPIONs. All error bars represent standard deviation of the fit parameter and are partially obscured by data markers.

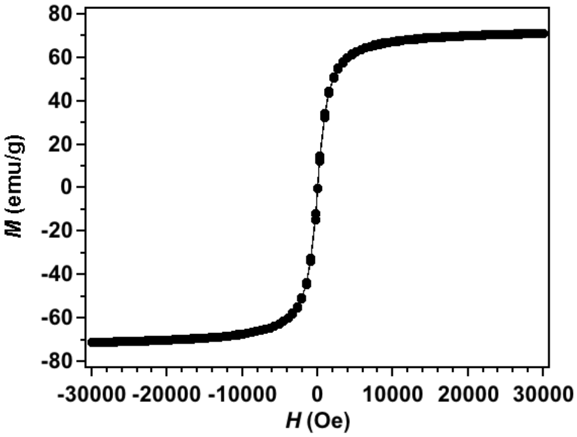

Figure 4.8 Magnetization curve of oleic acid-capped SPIONs at 300 K. A saturation magnetization, M_s, of 71 emu/g, determined from the plateau of the magnetization curve, was used to estimate theoretical maximum relaxivity in Eq. (4.3).

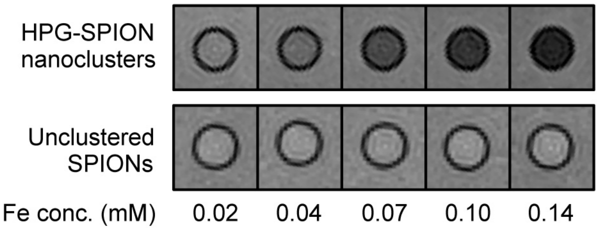

Figure 4.9 MR phantom images comparing nanoclusters with relaxivity of 719 $mM^{-1}s^{-1}$ to unclustered SPIONs with relaxivity of 122 $mM^{-1}s^{-1}$.

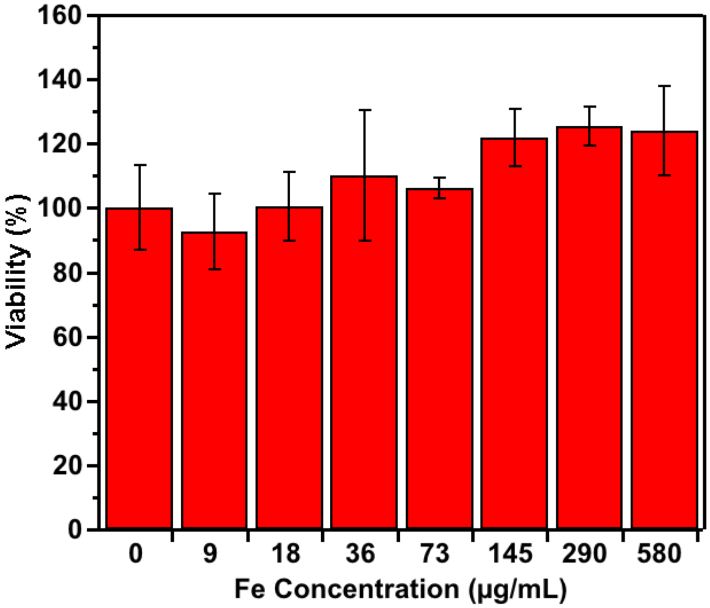

Figure 4.10 MTT assay to assess effects of HPG-SPION nanoclusters on metabolic activity of C166 endothelial cells. Percent viability was determined by normalization of absorbance values after blank subtraction to that of a control group of cells incubated without HPG-SPIONs. The concentration of Fe in the cell culture media was varied by altering the mass of SPION clusters. Values are the average of 3 replicates and error bars represent standard deviation.

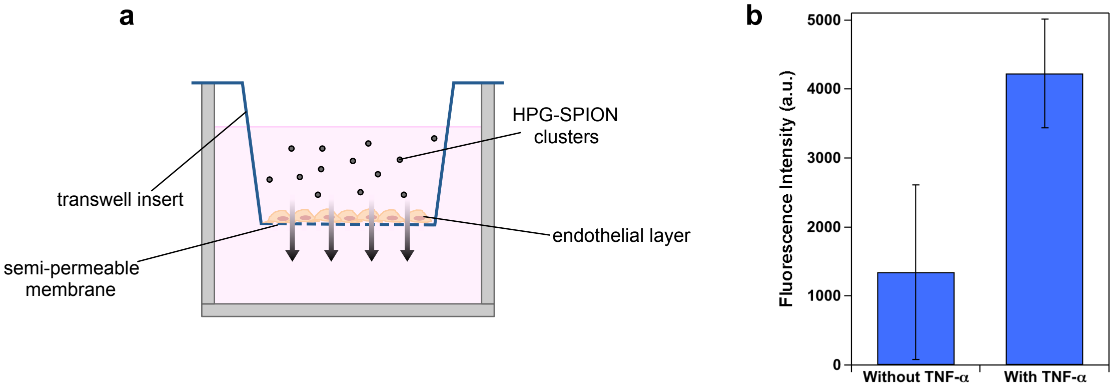

Figure 4.11 Endothelial transwell migration assay. (a) Schematic of the transwell insert. (b) Fluorescence intensity of the receiving well after incubation of FITC-labeled HPG-SPIONs and C166 cells with and without exposure to inflammation-inducing TNF-α. The diffusion of HPG-SPION nanoclusters was more than 3-fold higher through the endothelial layer exposed to TNF-α. Error bars represent standard deviation of three replicates.

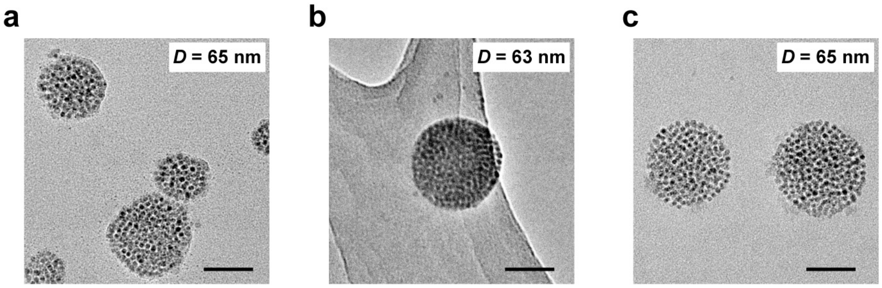

Figure 4.12 TEM micrographs of HPG-SPIONs before and after incubation with 50% human serum in PBS. The HPG-SPIONs with a hydrodynamic diameter of 122 nm and relaxivity of 719 $mM^{-1}s^{-1}$ were analyzed, and average core diameter is indicated on each figure. (a) TEM and (b) cryo-TEM images of the SPION clusters before serum incubation. (c) After incubation with 50% human serum in PBS for 2 h at 37 °C, the morphology and size remained unchanged, according to TEM micrographs. Scale bars represent 50 nm.

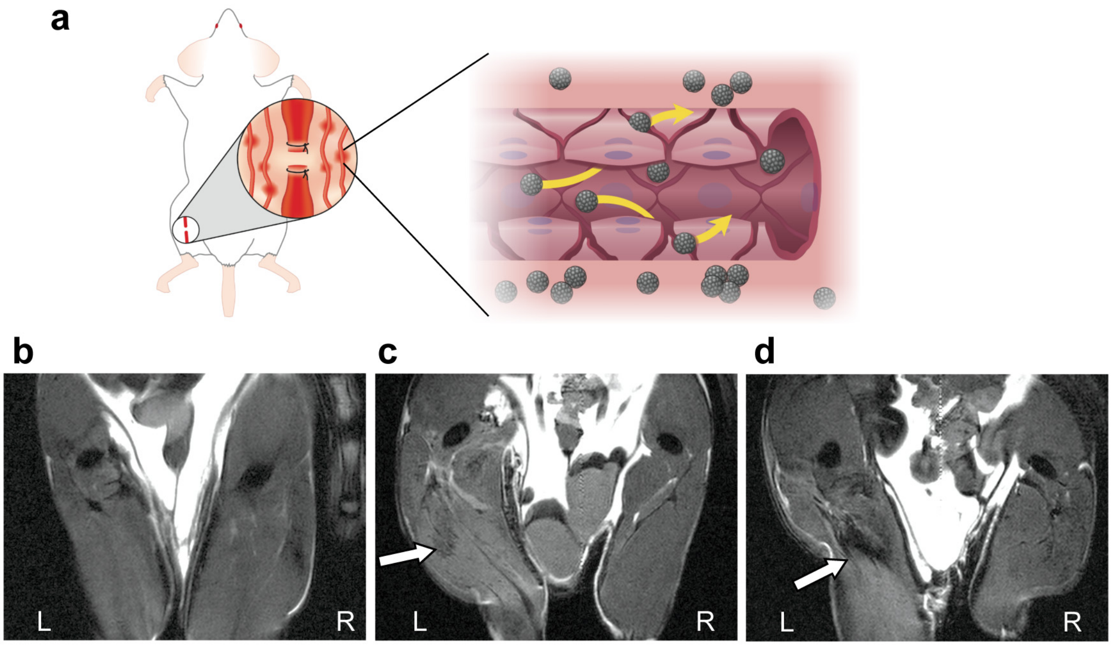

Figure 4.13 *In vivo* evaluation of the ability of SPION nanoclusters to highlight damaged tissue in MR images. (a) Hindlimb ischemia was induced by ligation of the left femoral artery. A control mouse receiving no injection of contrast agent (b) is compared to mice injected systemically with unclustered SPIONs (c) or the HPG-SPIONs with relaxivity of 719 $mM^{-1}s^{-1}$ (d). White arrows indicate negative contrast in the injured region.

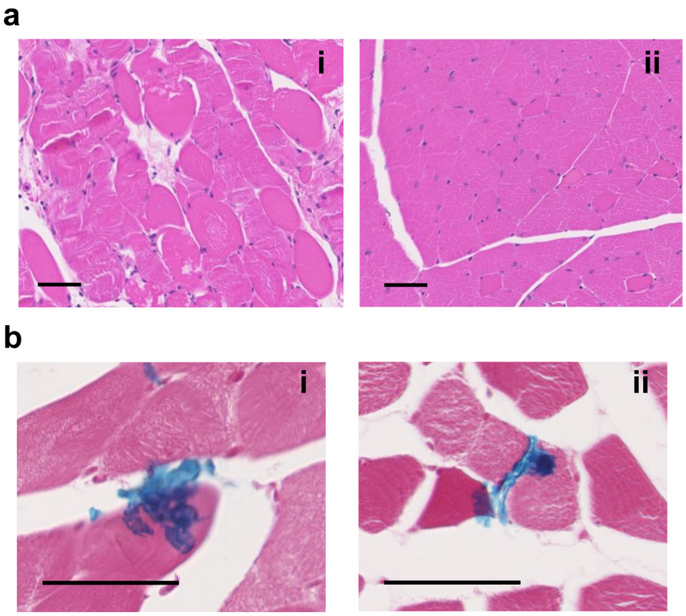

Figure 4.14 Histological analysis of the hindlimb ischemia model. (a) H&E staining of (i) the ischemic left hindlimb, indicating tissue damage as a result of ischemia and (ii) the uninjured, right hindlimb. (b) Prussian blue staining of the left, ischemic hindlimb sections containing (i) HPG-SPION nanoclusters and (ii) unclustered SPIONS, indicating the presence of contrast agent in both cases. In all figures, scale bars represent 50 μm.

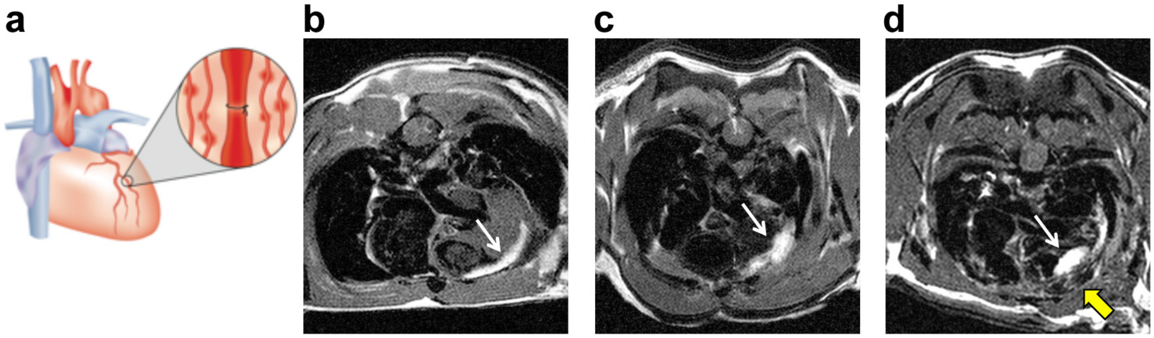

Figure 4.15 SPION nanoclusters in a model of coronary ischemia. Ligation of the coronary artery resulted in myocardial infarction (a). As with the hindlimb model, a control mouse (b) is compared to injection of the unclustered SPIONs (c) or the HPG-SPIONs (d). White arrows indicate areas of edema, which is typical of the infarcted region. The yellow arrow represents negative contrast in the region of interest.

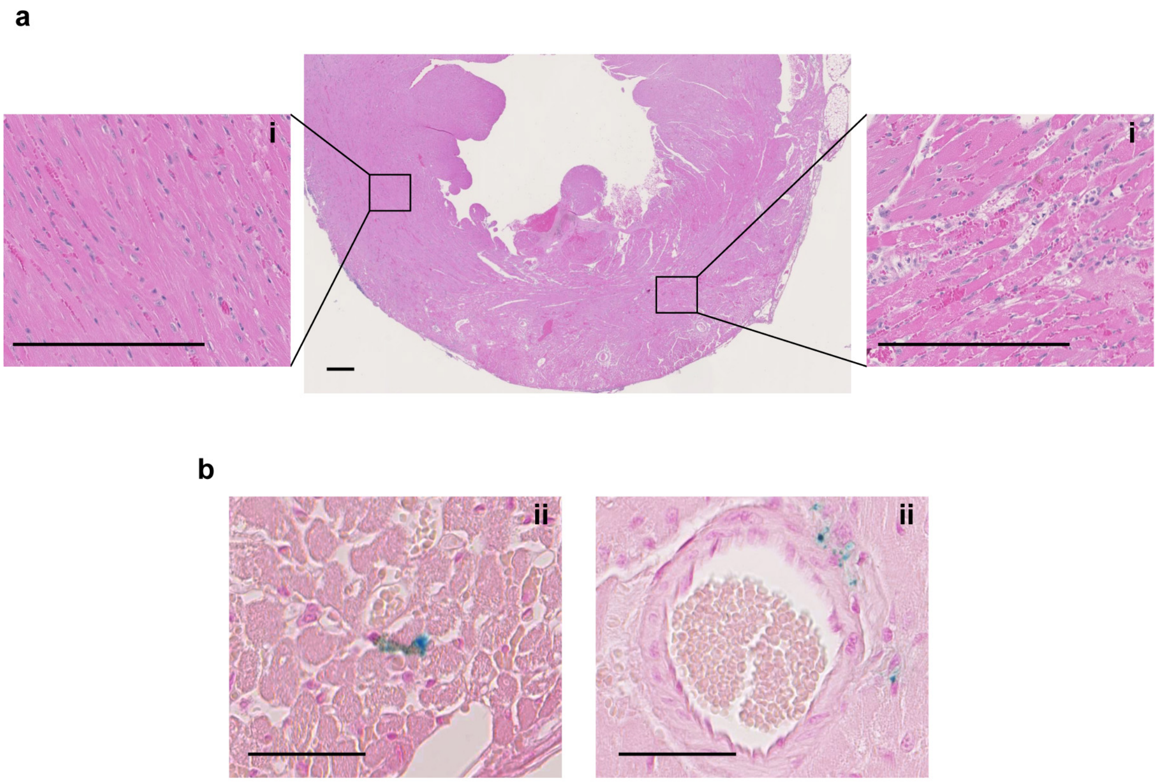

Figure 4.16 Histological analysis of the coronary ischemia model. (a) H&E staining of the heart, indicating (i) healthy and (ii) infarcted regions as a result of occluded blood flow. Scale bars represent 250 µm. (b) Prussian blue staining for iron in heart sections containing (i) unclustered SPIONs and (ii) HPG-SPION nanoclusters within the injured region. Scale bars represent 50 µm.

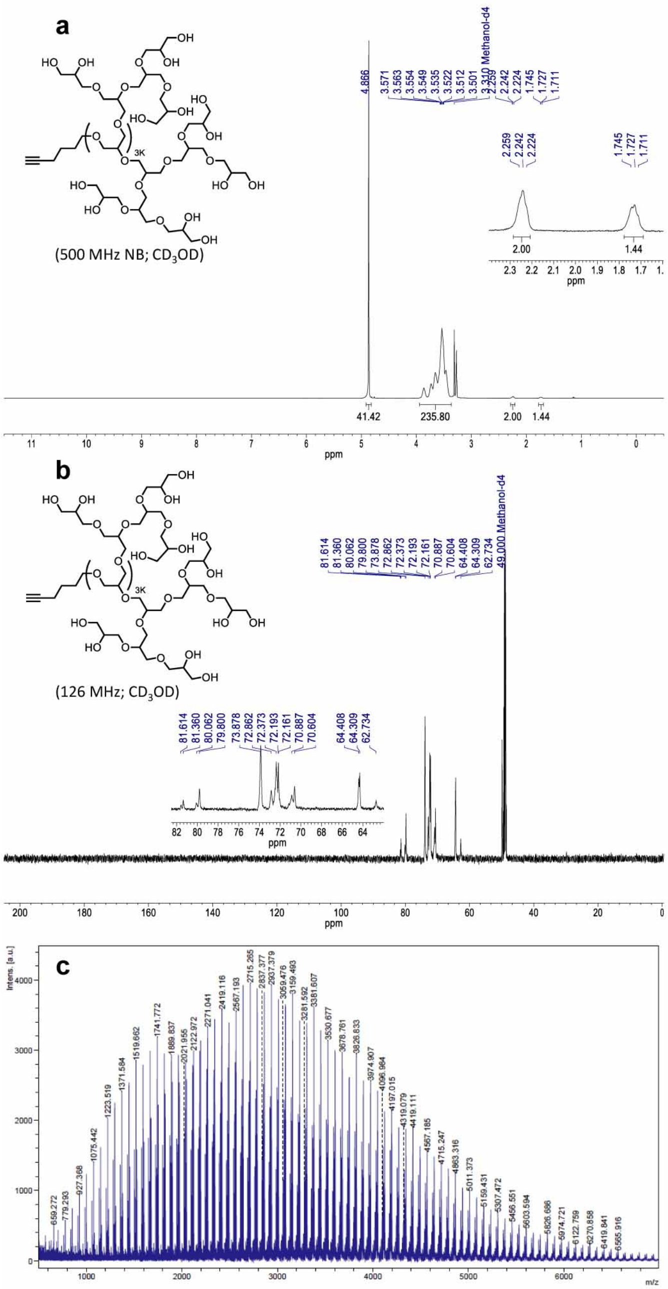

Figure 4.17 Characterization of HPG_{3k} by (a) ^1H NMR, (b) ^{13}C NMR, and (c) MALDI-TOF. HPG_{3k} represents HPG with a molecular weight (MW) of 3,000 g/mol. **^{1}H NMR** (400 MHz, methanol-*d*$_4$) δ 4.87 (s, 41H), 3.94 – 3.37 (m, 236H), 2.24 (t, *J* = 7.0 Hz, 2H), 1.78 – 1.69 (m, 1H). **^{13}C NMR** (126 MHz, methanol-*d*$_4$) δ 81.61, 81.36, 80.06, 79.80, 73.88, 72.86, 72.37, 72.19, 72.16, 70.89, 70.60, 64.41, 64.31, 62.73. **MS (MALDI)** m/z ~3000, peak separation 74 m/z units.

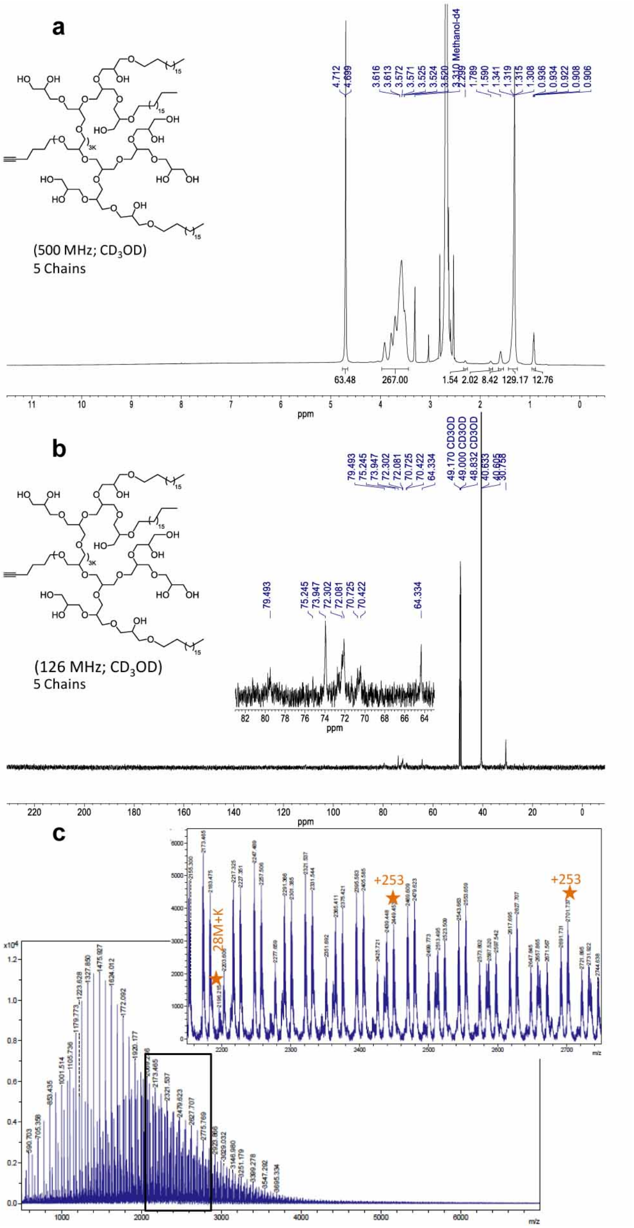

Figure 4.18 Characterization of HPG$_{3k}$-g-C$_{18}$(5) by (a) ^{1}H NMR, (b) ^{13}C NMR, and (c) MALDI-TOF. Protons of the C$_{18}$ chain are from 1-2 ppm in the ^{1}H NMR spectrum. HPG$_{3k}$-g-C$_{18}$(5) represents HPG (MW ~3,000 g/mol) substituted with 5 C$_{18}$ chains. **^{1}H NMR** (500 MHz, methanol-*d*$_4$) δ 4.71 (d, *J* = 6.6 Hz, 63H), 3.97 – 3.44 (m, 267H), 2.30 (s, 2H), 1.79 (s, 2H), 1.59 (s, 8H), 1.43 – 1.25 (m, 129H), 0.96 – 0.89 (m, 13H). **^{13}C NMR** (126 MHz, methanol-*d*$_4$) δ 79.49, 73.95, 72.30, 72.08, 70.73, 70.42, 64.33, 40.63, 40.61, 30.76. **MS (MALDI)** peak separation 253 m/z units.

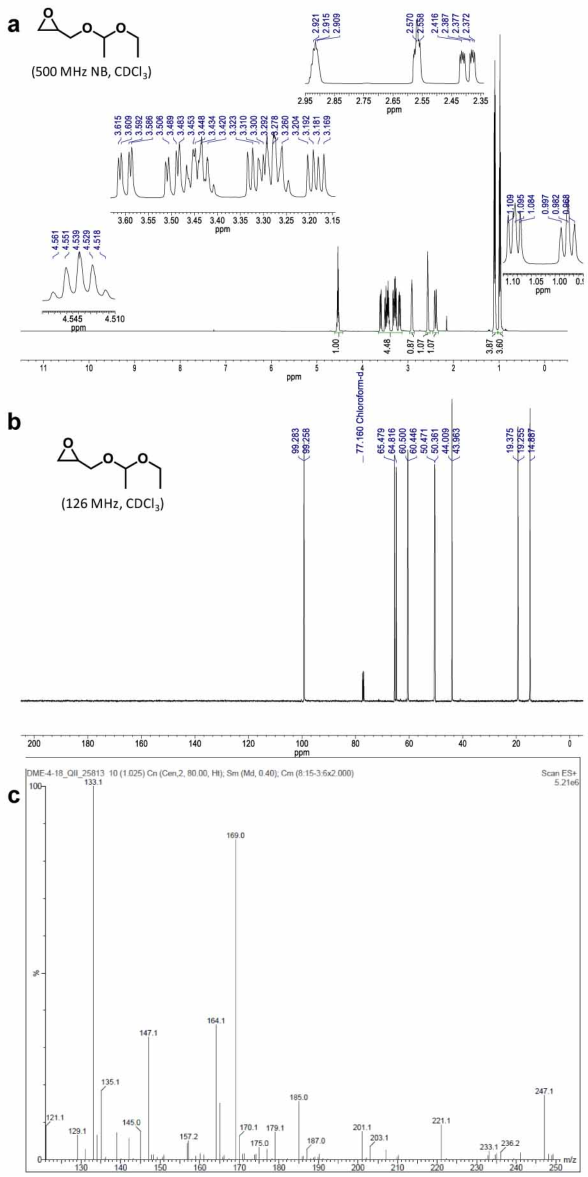

Figure 4.19 Characterization of EEGE, an LPG synthetic intermediate, by (a) ^{1}H NMR, (b) ^{13}C NMR, and (c) ESI mass spectrometry, calculated 146 m/z, experimental 147.1 (M+1), 169.0 m/z (M+Na). **^{1}H NMR** (500 MHz, chloroform-*d*) δ 4.58 – 4.49 (m, 1H), 3.64 – 3.14 (m, 5H), 2.95 – 2.88 (m, 1H), 2.57 (ddt, *J* = 5.9, 3.1, 1.5 Hz, 1H), 2.43 – 2.35 (m, 1H), 1.10 (ddd, *J* = 6.5, 5.4, 1.1 Hz, 4H), 0.98 (tt, *J* = 7.1, 1.3 Hz, 4H). **^{13}C NMR** (126 MHz, chloroform-*d*) δ 99.28, 99.26, 65.48, 64.82, 60.50, 60.45, 50.47, 50.36, 44.01, 43.96, 19.37, 19.25, 14.89.

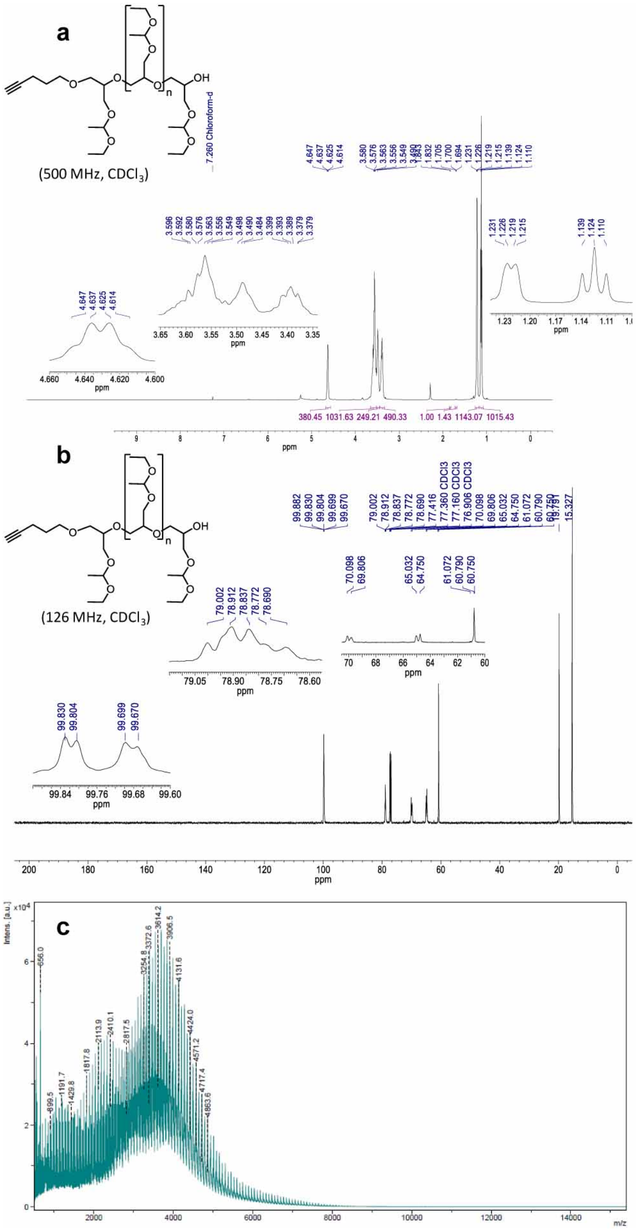

Figure 4.20 Characterization of poly(EEGE), an LPG synthetic intermediate, by (a) ^{1}H NMR, (b) ^{13}C NMR, and (c) MALDI-TOF. **^{1}H NMR** (500 MHz, chloroform-*d*) δ 4.63 (q, *J* = 5.5 Hz, 380H), 3.65 – 3.51 (m, 1032H), 3.49 (q, *J* = 4.2 Hz, 249H), 3.44 – 3.34 (m, 490H), 1.84 (d, *J* = 5.6 Hz, 1H), 1.70 (t, *J* = 2.6 Hz, 1H), 1.26 – 1.18 (m, 1143H), 1.12 (t, *J* = 7.1 Hz, 1015H). **^{13}C NMR** (126 MHz, CDCl$_3$) δ 99.88, 99.83, 99.80, 99.70, 99.67, 79.00, 78.91, 78.84, 78.77, 78.69, 77.42, 70.10, 69.81, 65.03, 64.75, 62.38, 61.07, 61.02, 60.79, 60.75, 19.79, 15.33. **MS (MALDI)** 3600 m/z, peak separation of 147 m/z units.

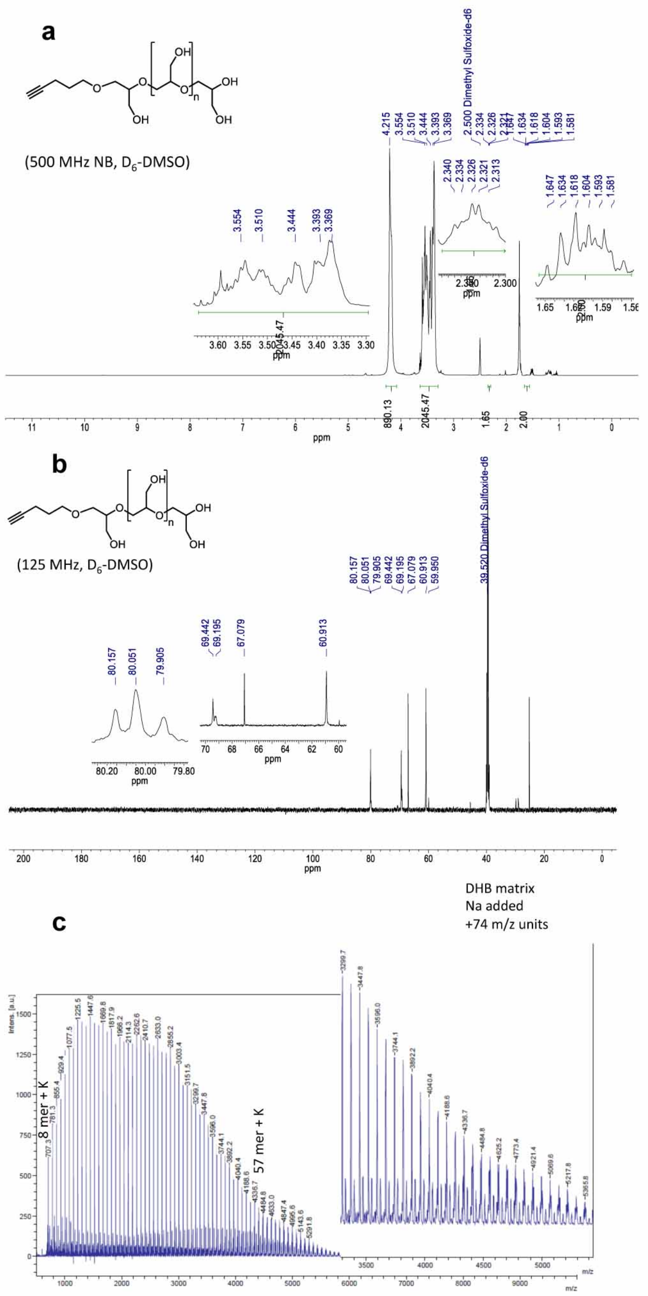

Figure 4.21 Characterization of LPG$_{3k}$ by (a) ^{1}H NMR, (b)^{13}C NMR, and (c) MALDI-TOF. LPG$_{3k}$ represents LPG with MW of ~3,000 g/mol. **^{1}H NMR** (500 MHz, DMSO-*d*$_6$) δ 4.29 – 4.11 (m, 1044H), 3.62 – 3.32 (m, 1897H), 2.32 (td, *J* = 6.9, 3.0 Hz, 1H), 1.65 – 1.58 (m, 2H). **^{13}C NMR** (126 MHz, DMSO-*d*$_6$) δ 80.16, 80.05, 79.91, 69.45, 69.29, 67.08, 60.92, 59.95, 40.02, 39.94, 39.86, 39.78, 39.69, 39.60, 39.52, 39.35, 39.27, 39.19, 39.02. **MS (MALDI)** ~3000 m/z, separation of 74 m/z units.

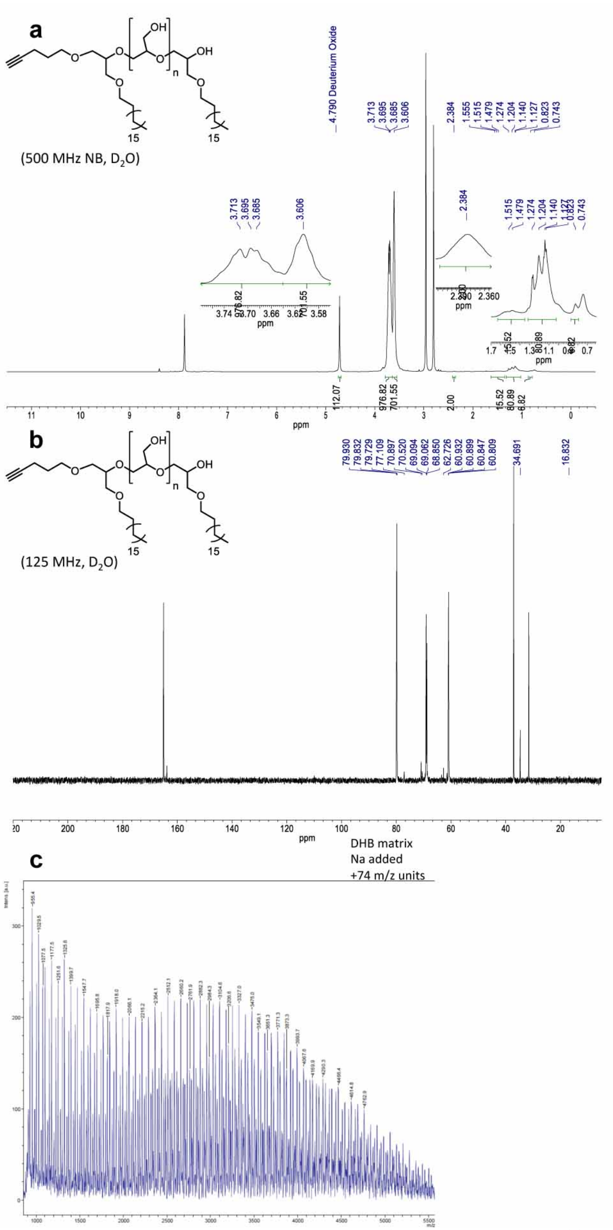

Figure 4.22 Characterization of LPG$_{3k}$-g-C$_{18}$(2) by (a) ^{1}H NMR, (b) ^{13}C NMR, and (c) MALDI-TOF. Protons of the C$_{18}$ chain are from 1-2 ppm in the ^{1}H NMR spectrum. LPG$_{3k}$-g-C$_{18}$(2) represents LPG (MW ~3,000 g/mol) substituted with 2 C$_{18}$ chains. **^{1}H NMR** (500 MHz, deuterium oxide) δ 3.70 (dd, *J* = 15.5, 9.7 Hz, 977H), 3.61 (s, 702H), 2.38 (s, 2H), 1.52 (m, 16H), 1.24 – 0.98 (m, 80H), 0.77 (s, 6H). **^{13}C NMR** (127 MHz, deuterium oxide) δ 79.93, 79.83, 79.73, 77.11, 70.90, 70.52, 69.09, 69.06, 68.85, 62.73, 60.93, 60.90, 60.85, 60.81, 37.08, 34.69, 31.57, 16.83. **MS (MALDI)** ~3500 m/z, separation of 74 m/z units.

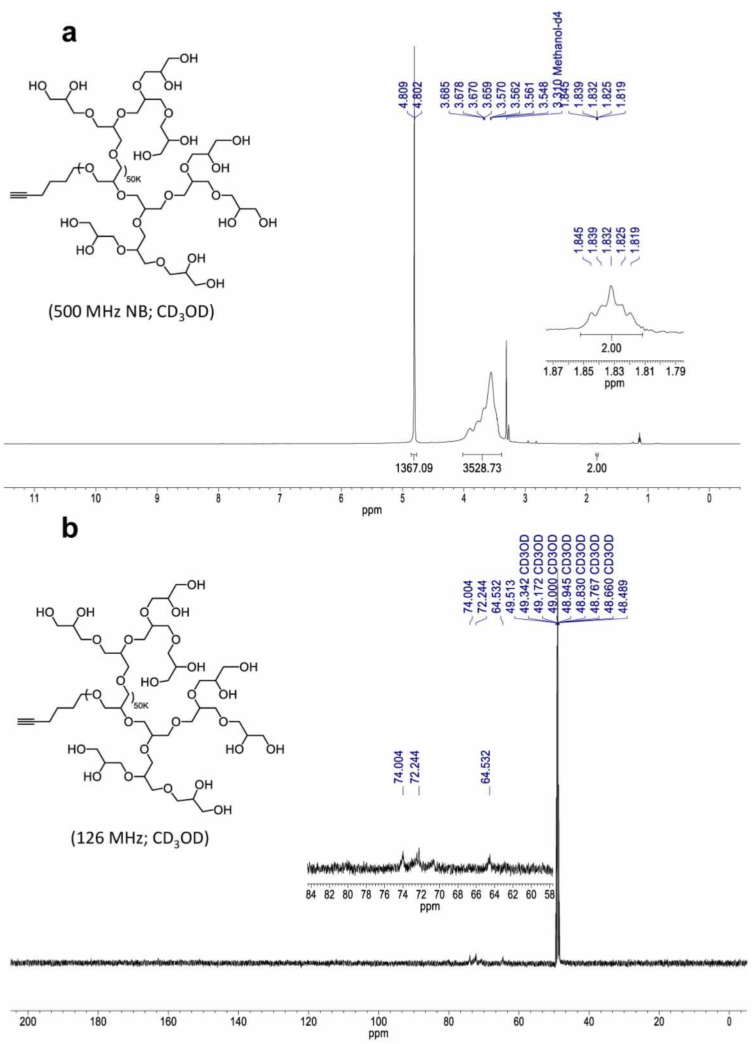

Figure 4.23 Characterization of HPG_{50k} by (a) ^{1}H NMR and (b) ^{13}C NMR. HPG_{50k} represents HPG with MW of ~50,000 g/mol. **^{1}H NMR** (500 MHz, methanol-d_4) δ 4.86 – 4.77 (m, 1367H), 4.02 – 3.39 (m, 3529H), 1.85 – 1.81 (m, 2H). **^{13}C NMR** (126 MHz, methanol-d_4) δ 74.00, 72.24, 64.53.

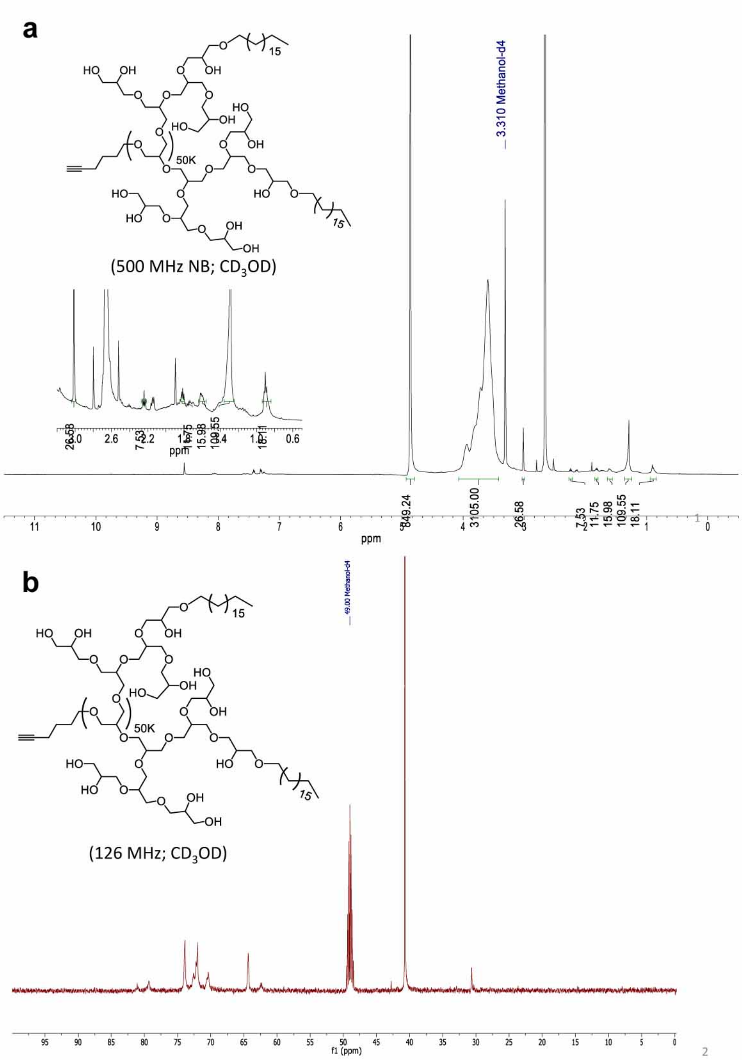

Figure 4.24 Characterization of HPG$_{50k}$-g-C$_{18}$(2) by (a) ^{1}H NMR and (b) ^{13}C NMR. Protons of the C$_{18}$ chain are from 1-2 ppm in the ^{1}H NMR spectrum. HPG$_{50k}$-g-C$_{18}$(2) represents HPG (MW ~50,000 g/mol) substituted with 2 C$_{18}$ chains. **^{1}H NMR** (500 MHz, methanol-*d*$_4$) δ 4.88 (s, 849H), 4.10 – 3.37 (m, 3105H), 3.03 (d, *J* = 3.0 Hz, 26H), 2.26 (t, *J* = 7.3 Hz, 8H), 1.88 – 1.78 (m, 12H), 1.67 – 1.56 (m, 16H), 1.32 (d, *J* = 9.5 Hz, 110H), 0.91 (dt, *J* = 10.0, 6.0 Hz, 18H). **^{13}C NMR** (126 MHz, methanol-*d*$_4$) δ 78.69, 72.84, 71.25, 71.04, 69.49, 63.36, 47.91, 47.84, 47.74, 47.56, 47.45, 47.39, 41.44, 39.28, 29.59.

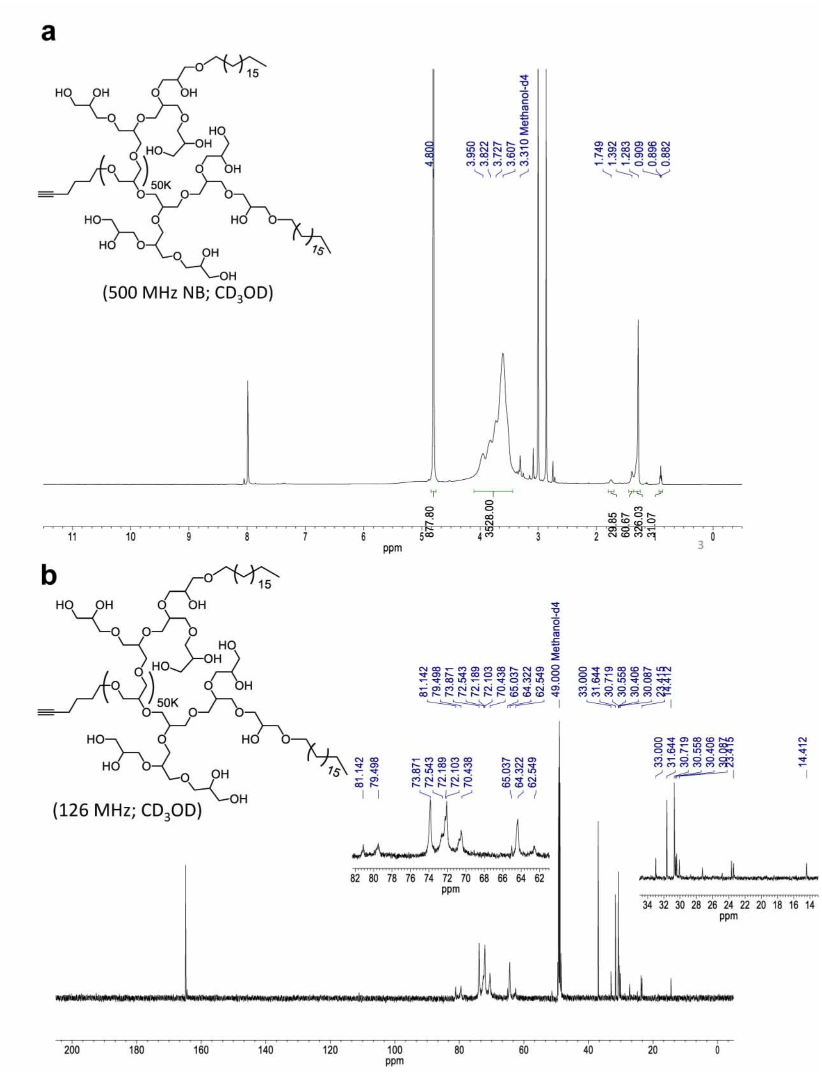

Figure 4.25 Characterization of HPG$_{50k}$-g-C$_{18}$(10) by (a) ^{1}H NMR and (b) ^{13}C NMR. Protons of the C$_{18}$ chain are from 1-2 ppm in the ^{1}H NMR spectrum. HPG$_{50k}$-g-C$_{18}$(10) represents HPG (MW ~50,000 g/mol) substituted with 10 C$_{18}$ chains. **^{1}H NMR** (500 MHz, methanol-*d$_4$*) δ 4.80 (s, 878H), 3.95 – 3.61 (m, 3528H), 1.75 (dd, *J* = 10.9, 5.9 Hz, 30H), 1.40 (d, *J* = 5.7 Hz, 60H), 1.28 (s, 326H), 0.91 (t, *J* = 6.7 Hz, 31H). **^{13}C NMR** (126 MHz, methanol-*d$_4$*) δ 81.14, 79.50, 73.87, 72.54, 72.19, 72.10, 70.44, 65.04, 64.32, 62.55, 30.00, 31.64, 30.72, 30.56, 30.41, 30.09, 23.42, 14.41.

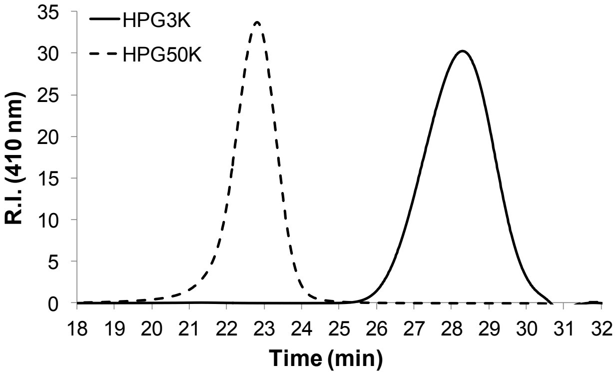

Compounds Synthesized	SEC DMF MW [a]	PDI
HPG_{3k}	28.28 min (3019 MW)	1.20
HPG_{50k}	22.80 min (46,025 MW)	1.46

[a] PEG standards

Figure 4.26 Characterization of molecular weights of HPG_{3k} and HPG_{50k} by GPC. The molecular weight of HPG_{3k} is in agreement with that determined by MALDI-TOF.

4.7 References

1. Cheon, J.; Lee, J.-H. Synergistically Integrated Nanoparticles as Multimodal Probes for Nanobiotechnology. *Acc. Chem. Res.* **2008,** *41*, 1630-1640.

2. Lee, N.; Hyeon, T. Designed Synthesis of Uniformly Sized Iron Oxide Nanoparticles for Efficient Magnetic Resonance Imaging Contrast Agents. *Chem. Soc. Rev.* **2012,** *41*, 2575-2589.

3. Tsushima, S.; Teranishi, K.; Hirai , S. Magnetic Resonance Imaging of the Water Distribution within a Polymer Electrolyte Membrane in Fuel Cells. *Electrochem. Solid-State Lett.* **2004,** *7*, A269-A272.

4. Elkins, C. J.; Markl, M.; Pelc, N.; Eaton, J. K. 4D Magnetic Resonance Velocimetry for Mean Velocity Measurements in Complex Turbulent Flows. *Exp. Fluids* **2003,** *34*, 494-503.

5. Cha, C.; Kim, S. Y.; Cao, L.; Kong, H. Decoupled Control of Stiffness and Permeability with a Cell-Encapsulating Poly(Ethylene Glycol) Dimethacrylate Hydrogel. *Biomaterials* **2010,** *31*, 4864-4871.

6. Yablonskiy, D. A.; Haacke, E. M. Theory of NMR Signal Behavior in Magnetically Inhomogeneous Tissues: The Static Dephasing Regime. *Magn. Reson. Med.* **1994,** *32*, 749-63.

7. Lee, N.; Kim, H.; Choi, S. H.; Park, M.; Kim, D.; Kim, H.-C.; Choi, Y.; Lin, S.; Kim, B. H.; Jung, H. S.*, et al.* Magnetosome-Like Ferrimagnetic Iron Oxide Nanocubes for Highly Sensitive MRI of Single Cells and Transplanted Pancreatic Islets. *Proc. Natl. Acad. Sci.* **2011,** *108*, 2662-2667.

8. Pöselt, E.; Kloust, H.; Tromsdorf, U.; Janschel, M.; Hahn, C.; Maßlo, C.; Weller, H. Relaxivity Optimization of a PEGylated Iron-Oxide-Based Negative Magnetic Resonance Contrast Agent for T_2-Weighted Spin-Echo Imaging. *ACS Nano* **2012,** *6*, 1619-1624.

9. Lee, H. J.; Jang, K.-S.; Jang, S.; Kim, J. W.; Yang, H.-M.; Jeong, Y. Y.; Kim, J.-D. Poly(Amino Acid)S Micelle-Mediated Assembly of Magnetite Nanoparticles for Ultra-Sensitive Long-Term MR Imaging of Tumors. *Chem. Commun.* **2010,** *46*, 3559-3561.

10. Ai, H.; Flask, C.; Weinberg, B.; Shuai, X. T.; Pagel, M. D.; Farrell, D.; Duerk, J.; Gao, J. Magnetite-Loaded Polymeric Micelles as Ultrasensitive Magnetic-Resonance Probes. *Adv. Mater.* **2005,** *17*, 1949-1952.

11. Taboada, E.; Solanas, R.; Rodríguez, E.; Weissleder, R.; Roig, A. Supercritical-Fluid-Assisted One-Pot Synthesis of Biocompatible Core(γ-Fe_2O_3)/Shell(SiO_2) Nanoparticles as High Relaxivity T_2-Contrast Agents for Magnetic Resonance Imaging. *Adv. Funct. Mater.* **2009,** *19*, 2319-2324.

12. Tan, H.; Xue, J. M.; Shuter, B.; Li, X.; Wang, J. Synthesis of PEOlated Fe_3O_4@SiO_2 Nanoparticles via Bioinspired Silification for Magnetic Resonance Imaging. *Adv. Funct. Mater.* **2010,** *20*, 722-731.

13. Paquet, C.; de Haan, H. W.; Leek, D. M.; Lin, H.-Y.; Xiang, B.; Tian, G.; Kell, A.; Simard, B. Clusters of Superparamagnetic Iron Oxide Nanoparticles Encapsulated in a Hydrogel: A Particle Architecture Generating a Synergistic Enhancement of the T_2 Relaxation. *ACS Nano* **2011,** *5*, 3104-3112.

14. Yoon, T.-J.; Lee, H.; Shao, H.; Hilderbrand, S. A.; Weissleder, R. Multicore Assemblies Potentiate Magnetic Properties of Biomagnetic Nanoparticles. *Adv. Mater.* **2011,** *23*, 4793-4797.

15. Smith, C. E.; Shkumatov, A.; Withers, S. G.; Yang, B.; Glockner, J. F.; Misra, S.; Roy, E. J.; Wong, C.-H.; Zimmerman, S. C.; Kong, H. A Polymeric Fastener Can Easily Functionalize Liposome Surfaces with Gadolinium for Enhanced Magnetic Resonance Imaging. *ACS Nano* **2013,** *7*, 9599-9610.

16. Geddes, R. Glycogen: A Structural Viewpoint. In *The Polysaccharides*, Aspinal, G. O., Ed. Academic Press: New York, 1985; Vol. 3, pp 283-336.

17. Limbourg, A.; Korff, T.; Napp, L. C.; Schaper, W.; Drexler, H.; Limbourg, F. P. Evaluation of Postnatal Arteriogenesis and Angiogenesis in a Mouse Model of Hind-Limb Ischemia. *Nat. Protocols* **2009,** *4*, 1737-1748.

18. Vuong, Q. L.; Berret, J.-F.; Fresnais, J.; Gossuin, Y.; Sandre, O. A Universal Scaling Law to Predict the Efficiency of Magnetic Nanoparticles as MRI T2-Contrast Agents. *Adv. Healthc. Mater.* **2012,** *1*, 502-512.

19. Dey, P.; Blakey, I.; Thurecht, K. J.; Fredericks, P. M. Self-Assembled Hyperbranched Polymer-Gold Nanoparticle Hybrids: Understanding the Effect of Polymer Coverage on Assembly Size and SERS Performance. *Langmuir* **2012,** *29*, 525-533.

20. Pöselt, E.; Fischer, S.; Foerster, S.; Weller, H. Highly Stable Biocompatible Inorganic Nanoparticles by Self-Assembly of Triblock-Copolymer Ligands. *Langmuir* **2009,** *25*, 13906-13913.

21. Murthy, A. K.; Stover, R. J.; Borwankar, A. U.; Nie, G. D.; Gourisankar, S.; Truskett, T. M.; Sokolov, K. V.; Johnston, K. P. Equilibrium Gold Nanoclusters Quenched with Biodegradable Polymers. *ACS Nano* **2012,** *7*, 239-251.

22. Paquet, C.; Pagé, L.; Kell, A.; Simard, B. Nanobeads Highly Loaded with Superparamagnetic Nanoparticles Prepared by Emulsification and Seeded-Emulsion Polymerization. *Langmuir* **2009,** *26*, 5388-5396.

23. Israelachvili, J. N. Steric (Polymer-Mediated) and Thermal Fluctuation Forces. In *Intermolecular and Surface Forces*, Israelachvili, J. N., Ed. Academic Press: San Diego, 2011; pp 381-413.

24. Burke-Gaffney, A.; Keenan, A. K. Modulation of Human Endothelial Cell Permeability by Combinations of the Cytokines Interleukin-1 Alpha/Beta, Tumor Necrosis Factor-Alpha and Interferon-Gamma. *Immunopharmacology* **1993,** *25*, 1-9.

25. Lee, J. H.; Huh, Y. M.; Jun, Y. W.; Seo, J. W.; Jang, J. T.; Song, H. T.; Kim, S.; Cho, E. J.; Yoon, H. G.; Suh, J. S.*, et al.* Artificially Engineered Magnetic Nanoparticles for Ultra-Sensitive Molecular Imaging. *Nat. Med.* **2007,** *13*, 95-99.

26. Lee, N.; Choi, Y.; Lee, Y.; Park, M.; Moon, W. K.; Choi, S. H.; Hyeon, T. Water-Dispersible Ferrimagnetic Iron Oxide Nanocubes with Extremely High R_2 Relaxivity for Highly Sensitive in Vivo MRI of Tumors. *Nano Lett.* **2012,** *12*, 3127-3131.

27. Serkova, N. J.; Renner, B.; Larsen, B. A.; Stoldt, C. R.; Hasebroock, K. M.; Bradshaw-Pierce, E. L.; Holers, V. M.; Thurman, J. M. Renal Inflammation: Targeted Iron Oxide Nanoparticles for Molecular MR Imaging in Mice. *Radiology* **2010,** *255*, 517-526.

28. LaConte, L. E.; Nitin, N.; Zurkiya, O.; Caruntu, D.; O'Connor, C. J.; Hu, X.; Bao, G. Coating Thickness of Magnetic Iron Oxide Nanoparticles Affects R_2 Relaxivity. *J. Magn. Reson. Imaging* **2007,** *26*, 1634-1641.

29. Zill, A.; Rutz, A. L.; Kohman, R. E.; Alkilany, A. M.; Murphy, C. J.; Kong, H.; Zimmerman, S. C. Clickable Polyglycerol Hyperbranched Polymers and Their Application to Gold Nanoparticles and Acid-Labile Nanocarriers. *Chem. Commun.* **2011,** *47*, 1279-1281.

30. Kainthan, R. K.; Janzen, J.; Levin, E.; Devine, D. V.; Brooks, D. E. Biocompatibility Testing of Branched and Linear Polyglycidol. *Biomacromolecules* **2006,** *7*, 703-709.

31. Stiriba, S.-E.; Kautz, H.; Frey, H. Hyperbranched Molecular Nanocapsules: Comparison of the Hyperbranched Architecture with the Perfect Linear Analogue. *J. Am. Chem. Soc.* **2002,** *124*, 9698-9699.

32. Clay, N.; Baek, K.; Shkumatov, A.; Lai, M.-H.; Smith, C. E.; Rich, M.; Kong, H. Flow-Mediated Stem Cell Labeling with Superparamagnetic Iron Oxide Nanoparticle Clusters. *ACS Appl. Mater. Interfaces* **2013,** *5*, 10266-10273.

33. Sun, S.; Zeng, H.; Robinson, D. B.; Raoux, S.; Rice, P. M.; Wang, S. X.; Li, G. Monodisperse MFe_2O_4 (M = Fe, Co, Mn) Nanoparticles. *J. Am. Chem. Soc.* **2003,** *126*, 273-279.

CHAPTER 5

MORPHOLOGICAL CONTROL OF IRON OXIDE NANOCLUSTERS BY HYPERBRANCHED POLYGLYCEROL FOR IMPROVED TISSUE TARGETING

Acknowledgments

Polyglycerol synthesis and modification was performed by Dawn Ernenwein and JuYeon Lee. SPR measurements were provided by Mei-Hsiu Lai, including the data used to make Figures 5.6c and 5.7, which resulted in the values displayed in Table 5.1. Animal studies were performed by Artem Shkumatov, and Nicholas Clay synthesized oleic acid-capped SPIONs. Additionally, Boris Odintsov and Ryan Larsen at the Beckman Institute for Advanced Science and Technology assisted with MR imaging. Iron content analysis was provided by the School of Chemical Sciences Microanalysis Laboratory, and I performed TEM measurements in the Frederick Seitz Materials Research Laboratory Central Facilities at the University of Illinois.

5.1 Introduction

Nanoparticles have been investigated for decades as carriers of various clinical diagnostic imaging agents and therapeutic molecules due to their ability to sustainably retain their cargoes and release them at controlled rates. Strategies to deliver such particles to tissues of interest, however, remain a highly active and challenging area of research.[1-5] Towards this effort, non-spherical nanoparticles are of increasing interest, predominantly due to their ability to adhere to target tissues with greater affinity than their spherical counterparts.[6,7] A common method of controlling nanoparticle shape is to increase the intermolecular packing parameter of self-assembling, amphiphilic molecules.[8,9] Attaining an appropriate packing parameter often relies on a large hydrophobic component in order to achieve a desired, elongated morphology.[10-12]

As a consequence, the resulting nanoparticles may significantly limit the functionality of their encapsulated materials due to the hydrophobic environment directly surrounding the cargo, which substantially reduces hydrophilic interactions with surrounding biological fluids. This is of particular importance in the design of magnetic resonance imaging (MRI) contrast agents, which rely mechanistically on the probe's ability to interact with water molecules of the target tissue.[13]

To this end, this study demonstrates an advanced method to direct the self-assembly of SPIONs into non-spherical clusters that maintain a hydrophilic environment in order to provide superior contrast capability and highlight leaky vascular defects in MR images. The non-spherical cluster assembly was achieved by emulsifying hydrophobic SPIONs with a binary mixture of amphiphilic hyperbranched polyglycerols (HPGs) having molecular weights that differed by an order of magnitude. HPG was previously used in Chapter 4 to facilitate the interaction between clustered SPIONs and surrounding water by mimicking the molecular architecture of glycogen, thereby dramatically increasing MR relaxivity. By varying the ratio of the low and high molecular weight HPG molecules, we were able to alter the morphology of SPION clusters from spherical to wormlike, with an average aspect ratio of 10. The resultant SPION nanoclusters were further modified with oligopeptides to bind with inflamed, leaky vasculature and displayed superior adhesion to target receptors compared to spherical clusters, according to *in vitro* studies. Finally, we assessed the ability of the bioactive, wormlike SPION nanoclusters to beacon vascular defects of an ischemic murine hindlimb after systemic injection at doses lower than we previously reported.

5.2 Results

5.2.1 Synthesis of hyperbranched polyglycerols and iron oxide nanoparticles

Alkylated HPG was synthesized as described in Chapter 4 by anionic polymerization of glycidol followed by reaction with bromooctadecane. The molecular weight was controlled from 3,000 g/mol to 50,000 g/mol by varying the ratio of glycidol to initiator. The low molecular weight HPG was found to have an average of five alkyl chains per molecule, termed HPG_{3k}-g-$C_{18}(5)$, while the high molecular weight counterpart had 10, termed HPG_{50k}-g-$C_{18}(10)$. Separately, SPIONs were fabricated using standard methods of high temperature thermal decomposition to yield an average core diameter of 5 nm.[14]

5.2.2 Fabrication of wormlike nanoclusters

Spherical clusters of SPIONs were fabricated by emulsifying SPIONs dispersed in chloroform with HPG dissolved in deionized water (Figure 5.1). In either case of HPG_{50k}-g-$C_{18}(10)$ or HPG_{3k}-g-$C_{18}(5)$, clusters had a spherical morphology. Interestingly, however, when the aqueous phase of the emulsion consisted of a binary mixture of the two HPG molecular weights, there was a notable change in morphology (Figure 5.2). Specifically, as f_{3k}, defined in Eq. (5.1), increased, the clusters became elongated.

$$f_{3k} = \frac{n_{3k}}{n_{3k} + n_{50k}} \tag{5.1}$$

Here, n_{3k} and n_{50k} are defined as the molar amount of HPG_{3k}-g-$C_{18}(5)$ and HPG_{50k}-g-$C_{18}(10)$ respectively. While short, non-spherical nanoclusters with an average aspect ratio of 4 were apparent for other mixtures, at a critical value of $f_{3k} = 0.75$, the SPION clusters were maximally extended in the form of wormlike structures. Such clusters had an average aspect ratio of 10, though some attained an aspect ratio greater than 20. We estimate that for $f_{3k} = 0.75$, approximately 50% of the SPIONs took the form of a wormlike cluster, while for the other mixtures tested, only approximately 15% of the SPIONs became incorporated into the elongated clusters.

The morphogenic properties of the system seem to arise from the molecular weight mismatch of the HPGs. While other studies have shown that wormlike micelles are possible depending on the hydrophobic content of a polymer, we found that changing the degree of alkylation, for example by using HPG_{50k} and HPG_{3k} both with two C_{18} chains per molecule, still resulted in wormlike appearance when $f_{3k} = 0.75$ (Figure 5.3a). Furthermore, mixing two types of HPG_{3k} did not result in worms, namely HPG_{3k}-g-$C_{18}(2)$ and HPG_{3k}-g-$C_{18}(5)$, nor did the high or low molecular weight HPGs produce SPION wormlike clusters when mixed with the intermediately sized HPG_{8k}-g-$C_{18}(2)$ (Figure 5.3b-d). Additionally, the SPIONs themselves served to favor the formation of wormlike structures, similar to other reports.[15] When the $f_{3k} = 0.75$ mixture of HPG_{3k}-g-$C_{18}(5)$ and HPG_{50k}-g-$C_{18}(10)$ was created without SPIONs, the vast majority of the structure produced were spherical, though a minority of wormlike structures could be seen by transmission electron microscopy (Figure 5.4). We therefore believe that the assembly of the morphology is a result of the synergistic effects of packing of low molecular weight HPG_{3k} around the high molecular weight HPG50k, and the strong hydrophobic driving force of SPIONs.

5.2.3 Nanocluster surface modification for active targeting

We next conjugated a targeting ligand to demonstrate the ability of the HPG-SPION cluster to accumulate at sites of interest. The peptide sequence VHPKQHR, which bears homology to very late antigen-4 (VLA-4) found on leukocytes, has been shown to bind to vascular cell adhesion molecule-1 (VCAM-1) overexpressed by inflamed endothelial cells.[16] In this way, conjugation of the peptide to a carrier can serve as a mechanism of immobilization. Therefore, we propose that conjugation of the peptide to alkylated HPG will allow for binding of the HPG-SPION worms to inflamed blood vessels, which are a hallmark of cardiovascular disease.[17]

The peptide was conjugated to an acrylate-modified HPG_{3k}-C_{18}(5) via the terminal cysteine residue (Figure 5.5 and 5.6a). The peptide-laden HPG was subsequently used to induce SPION clustering. The presence of the peptide did not interfere with the morphology of the clusters, as $f_{3k} = 0.75$ remained wormlike while $f_{3k} = 1$ was spherical, using peptide-modified HPG_{3k}-C_{18}(5) (Figure 5.6b).

5.2.4 Kinetic binding analysis of targeted nanoclusters

To evaluate the kinetic binding of targeted spherical and wormlike structures to sites of inflammation, surface plasmon resonance (SPR) spectroscopy was performed. VCAM-1 receptors were immobilized on an SPR chip and SPION clusters were flowed over to examine their binding under convective flow. The binding resonance unit (RU) for the wormlike clusters was dramatically higher than that of the spheres at the same iron dose (Figure 5.6c). The reason is likely do to the way in which the nanostructures are able to adhere to the binding sites. As a wormlike structure is able to extend across the inflammation-mimicking surface, it is able to interact with more binding sites compared to its spherical counterpart (Figure 5.6d). Noting that RU is indicative of mass binding to the SPR chip,[18] the wormlike clusters are better able to bring iron oxide contrast agent to the site of interest.

In consideration of binding parameters, the association rate constant, k_a, was 10-fold higher per iron dose for worms compared to spheres (Table 5.1). Additionally, the dissociation rate constant, k_d, was orders of magnitude lower, thus highlighting the superior adherent nature of the morphology. As a result, the overall binding constant was over 1000-fold greater for the wormlike clusters. In addition to morphology, the importance of the targeting peptide was evaluated in control experiments using non-targeted HPG-SPION nanoclusters, or targeted clusters flowed over VCAM pre-saturated with peptide (Figure 5.7). Without targeting peptide, the binding was significantly reduced compared to binding between VCAM-1 and the peptide-conjugated wormlike HPG-SPIONs. Similarly, by occupying the binding sites of VCAM-1 prior to administering the nanoclusters, the peptide-conjugated SPION clusters were no more advantageous to binding than their non-targeted counterpart.

5.2.5 In vivo evaluation of targeted nanoclusters

The utility of the wormlike nanoparticle clusters in targeting defective tissue *in vivo* was evaluated using a murine model of hindlimb ischemia. Vascular occlusion of the left femoral artery resulted in local tissue damage. Peptide-conjugated HPG-SPION clusters were then injected systemically via tail vain at an iron dose of 1 mg/kg to locally highlight the injured region in MR scans (Figure 5.8). In both cases of targeted spherical and wormlike clusters, signal was locally reduced in the injured region. However, in the case of the wormlike clusters, the contrast was significantly more pronounced, with a signal reduction of 70% compared to native muscle, while the spheres produced a 45% signal reduction. Both types of clusters provided very high T_2 molar relaxivity of 600 $mM^{-1}s^{-1}$, which is likely due to the compact clustering and hyperbranched, hydrophilic polymer coating as previously described in Chapter 4. While differences in contrast may be due in part to a slightly higher relaxivity for the wormlike structure (Figure 5.9), the more significant effect is likely the higher accumulation of SPIONs at the target site due to the elongated morphology, as the contrast effect appeared similar per dose of iron in either system. Furthermore, histological sections of the injured mouse hindlimb indicated 50% more iron content per area in the case of wormlike clusters, as indicated by Prussian blue staining (Figure 5.10). The *in vivo* result is supported by the SPR binding data, which demonstrate an enhanced ability of the targeted worms to adhere to the site of interest.

5.3 Discussion

The strategy presented mimics the way in which several strains of bacteria have developed rod-shaped or filamentous morphologies to maximize contact surface area with the endothelium of their host under shear forces of blood flow.[19] As such, our approach was able to bring higher amounts of iron oxide to the target site and retain it for imaging. Additionally, the elongated morphology may allow for extended circulation *in vivo*,[20] which could also promote accumulation at sites of inflammation. Furthermore, since our approach of tuning the morphology of the nanoclusters relied on size mismatch rather than hydrophobicity, we were able to maintain a high degree of hydrophilicity, which is important in the design of any MRI contrast agent. As a result of this hydrophilicity coupled with the high degree of clustering, the relaxivity of the clusters was higher than previous reports of elongated nanocarriers of SPIONs.[21-23] Taken together, the superior relaxivity and targetability allowed for *in vivo* diagnosis at doses lower than previously reported in Chapter 4.

5.4 Conclusion

In this study we have demonstrated the superior adhesive qualities of the HPG-induced wormlike micelles that ultimately allowed for greater targetability and accumulation at sites of interest *in vivo*. By varying the ratio of high and low molecular weight HPG molecules used during emulsification with hydrophobic SPIONs, we were able to tune the morphology of the resultant nanoclusters from spherical to wormlike. In future studies, the wormlike structures may be purified from their spherical counterparts to yield a uniform population with enhanced targetability. Additionally, by understanding the specific parameters that result in the wormlike clusters it may be possible to fabricate populations that are more monomodal. In this way, efforts to study this mechanism of self-assembly will be critical in further improving these targeted clusters. Overall, We believe that the assembly strategy presented here could be readily extended to other nanoparticle types, and is therefore broadly applicable to colloidal systems. By incorporating iron oxide nanoparticles in the clustered core, this work also has the potential to substantially enhance imaging-based diagnostic capabilities.

5.5 Materials and Methods

5.5.1 Synthesis of HPG

All materials were purchased from Sigma-Aldrich unless otherwise noted. Hyperbranched polyglycerol (HPG) was synthesized by anionic ring polymerization of glycidol as described previously in Chapter 4. Briefly, to the distilled initiator 4-pentyn-1-ol, NaH was added and stirred for ~15 min to allow deprotonation. Then twice-distilled glycidol was slowly added at a rate of 1.2 mL/h while stirring at 70 °C. The molar ratio of initiator to glycol was varied to attain different molecular weights. For the high molecular weight HPG, dioxane was used as a solvent and emulsifying agent before the glycidol addition. The resulting HPGs were characterized by MALDI-TOF, ^{1}H NMR and ^{13}C NMR.

5.5.2 Alkylation of HPG

HPG was prepared by drying under high vacuum overnight 1 day before the alkylation reaction. Dried HPG (390 mg, 0.133 mmol, 1eq) was dissolved in 20 mL of anhydrous DMF and NaH (0.14 g, 27 eq., 60% in mineral oil) was added to deprotonate alcohol groups in HPG. The solution was stirred for ~15 min under nitrogen, and bromooctadecane (1.19 g, 27 eq) was added to the solution. By changing the ratio of bromooctadecane to HPG, the average degree of alkylation was controlled. After the addition of reagents, the reaction solution was stirred at 80 °C for 24 h. The reaction mixture was extracted with hexane a minimum of 4 times to remove remaining bromooctadecane, and DMF layer was collected. DMF was then removed by rotary evaporation and high vacuum. The degree of alkylation was calculated the ^{1}H NMR spectra.

5.5.3 Conjugation of peptide to HPG

Alkylated HPG, HPG_{3k}-g-C_{18}(5) (107.3 mg, 1 eq.), was prepared by drying under high vacuum overnight 1 day before the reaction. Dried HPG was dissolved in anhydrous DMF (20 mL) and distilled triethylamine (467.5 μL, 312 eq.) was added to the solution. The reaction flask was placed in an ice bath before the addition of methacryloyl chloride to cool the reaction solution. Methacryloyl chloride (359 μL, 156 eq.) was then added dropwise. The reaction mixture was stirred for 24 h at 0 °C to RT. The substitution reaction of methacryloyl chloride by OH groups in HPG was monitored by crude ^{1}H NMR spectra with an aliquot of the reaction mixture. Then, the peptide solution in DMF (137.8 mg, 6 eq., NH_2-VHPKQHRGGSWGC-$CONH_2$) was added to the reaction flask, and the reaction was allowed to proceed for another 24h at 60 °C. The thiol group in cysteine reacted with the methacryloyl group on HPG via Michael addition. Afterwards, the remaining methacryloyl groups on HPG were quenched with

3-mercaptopropane-1,2-diol. The reaction solution was then dialyzed against an aqueous NaCl solution (10 g/L followed by 5 g/L) for 2 days, and then against deionized water for 1 day. The amount of peptide conjugated to HPG_{3k}-g-C_{18}(5) was determined by UV absorbance at 280 nm.

5.5.4 Formation of iron oxide nanoclusters

Oleic acid-capped iron oxide nanoparticles were fabricated by high temperature thermal decomposition and dispersed in chloroform at a concentration of 10 mg/mL. To form nanoclusters, SPIONs were sonicated with varying ratios alkylated HPG_{50k} and HPG_{3k} dissolved in water. Chloroform was then removed by rotary evaporation, and the resultant clusters were purified from unencapsulated material by centrifugation. For targeted clusters, peptide-conjugated HPG_{3k}-g-C_{18} was incorporated with either HPG_{50k}-g-C_{18} or unmodified HPG_{3k}-g-C_{18} at a 3:1 molar ratio to make wormlike and spherical clusters respectively.

5.5.5 Microscopy of nanoclusters

HPG-SPION nanoclusters were imaged with a JEOL 2100 transmission electron microscope (JEOL 2100 cryo TEM) at an accelerating voltage of 200 kV. Specimens were prepared by air-drying on a holey carbon-coated copper grid. Analysis was done with ImageJ software, and a minimum of 50 clusters were imaged per condition.

5.5.6 Determination of kinetic binding parameters

The targeted binding of peptide-conjugated nanoclusters was measured with a Biacore 3000 (GE Healthcare, USA). A gold sensor chip was modified with 11-mercapoundecanoic acid to present reactive carboxylic acid groups on the chip surface. The carboxyl groups were then activated by flowing 1-ethyl-3-(3-dimethylaminopropyl)carbodiimide (EDC) and *N*-hydroxysuccinimide (NHS) over the chip, followed by VCAM to attach the protein to the gold surface. Nanoclusters suspended in PBS at an iron concentration of 420 μM were then injected into the flow cell at a rate of 5 μL/min to measure association and dissociation rates with the VCAM-coated surface. For control experiments, free targeting peptide at a concentration of 6 mg/mL was flowed over the surface for 20 min at a rate of 2 μL/min prior to introduction of nanoclusters to saturate the binding sites. Binding parameters were determined from a 1:1 Langmuir binding model with BIAevaluation software version 4.1.

5.5.7 Relaxivity characterization

MR images were acquired with a 3 T Siemens Magnetom Trio scanner (Siemens AG, Erlangen, Germany) using a spin echo pulse sequence. The repetition time (TR) was 1200 ms and the echo time (TE) was varied from 12 to 490 ms. For each TE, signal intensity was measured using ImageJ software, and the T_2 relaxation time was determined by least squares curve fitting of signal as a function of TE. Iron content was measured by inductively couple plasma optical emission spectroscopy (ICP-OES, Perkin Elmer Optima 2000 DV, Norwalk, CT) after digesting MR phantoms in concentrated nitric acid. Relaxivity was then determined as the slope of the relaxation rate ($1/T_2$) versus iron content.

5.5.8 In vivo ischemia model

A murine model of hindlimb ischemia was used with male BALB/c mice (Jackson Laboratories, ME) in accordance with the protocol approved by the Illinois Institutional Animal Care and Use Committee. Anesthesia was induced by intraperitoneal injection of xylazine (10 mg/kg) and ketamine hydrochloride (100 mg/kg). A small incision was performed on the upper thigh of the left hindlimb to expose the femoral artery, which was ligated in two regions with 5-0 Ethilon sutures (Johnson and Johnson, NJ). The artery was then severed between the two sutures. The resulting ischemic condition developed for 24 h, followed by injection of SPIONs through the tail vein at a dose of 1 mg Fe/kg.

Mice were then imaged 3 h after administering the SPION contrast agents with a Varian 14.1 T microimager that consisted of a Unity/Inova 600 MHz NMR spectrometer and adjustable radiofrequency coil. A spin-echo multislice (SEMS) pulse sequence was used to collect coronal images with TR = 500 ms, TE = 20 ms, slice thickness = 0.5 mm, and matrix size = 256 x 256.

5.5.9 Histological analysis

The mouse hindlimbs were fixed in 10% buffered formalin and then embedded in paraffin. Sections were cut at a 4 μm thickness with a Leica RM 2255 rotary microtome. Tissues were stained with Hematoxylin and Eosin (H&E) to analyze morphology and confirm the ischemic injury, or Prussian blue stain to indicate the presents of SPIONs. The sections were analyzed using a NanoZoomer Slider Scanner/Digital Pathology System (Hamamatsu). The relative degree of SPION accumulation was determined by measuring the blue-stained area in histological images using ImageJ software. A total of 200 mm^2 of tissue was analyzed for each condition.

5.6 Figures and Tables

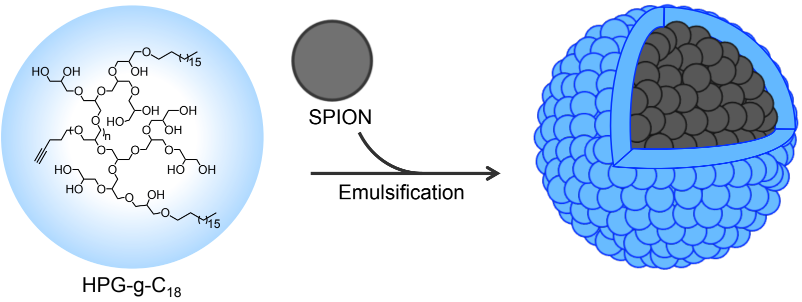

Figure 5.1 Fabrication of HPG-SPION nanoclusters by emulsification. Amphiphilic HPG stabilizes the hydrophobic SPIONs in the form of a controlled aggregate.

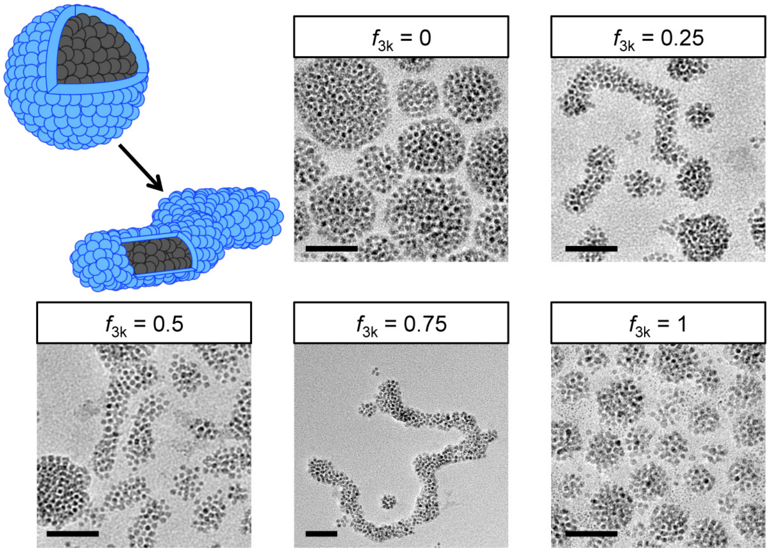

Figure 5.2 Sphere-to-worm transition. As high and low molecular weight HPGs were incorporated together during emulsification, the resultant SPION clusters became elongated, with maximal length occurring for a 3:1 HPG$_{3k}$-g-C$_{18}$(5):HPG$_{50k}$-g-C$_{18}$(10) ratio. Scale bars represent 50 nm in all cases.

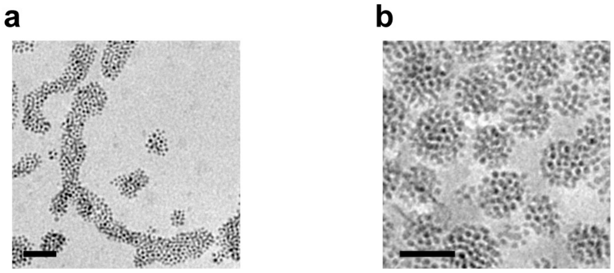

3:1
HPG$_{3k}$-g-C$_{18}$(2) : HPG$_{50k}$-g-C$_{18}$(2)

3:1
HPG$_{3k}$-g-C$_{18}$(2) : HPG$_{3k}$-g-C$_{18}$(5)

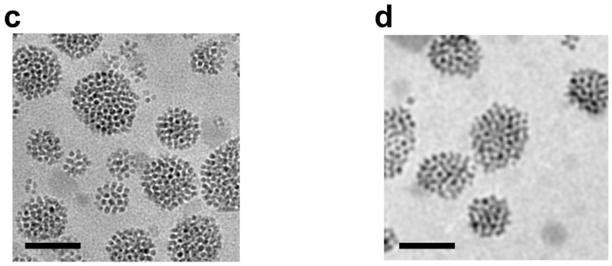

3:1
HPG$_{3k}$-g-C$_{18}$(2) : HPG$_{8k}$-g-C$_{18}$(2)

3:1
HPG$_{8k}$-g-C$_{18}$(2) : HPG$_{50k}$-g-C$_{18}$(2)

Figure 5.3 Effects of alkylation and molecular weight mismatch on cluster morphology. (a) A 3:1 ratio of low:high molecular weight HPG still resulted in wormlike clusters when both had an average of two C_{18} chains per molecule. (b) Alkylated HPG$_{3k}$ was unable to produce wormlike clusters by varying only the degree of alkylation. Similarly, using an intermediately sized HPG, HPG$_{8k}$-g-C_{18}(2), resultant only in spheres when mixed with alkylated (c) HPG$_{3k}$ and (d) HPG$_{50k}$. Scale bars represent 50 nm.

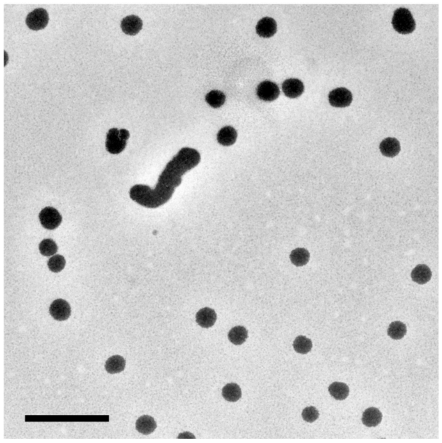

Figure 5.4 A 3:1 mixture of HPG$_{3k}$-g-C$_{18}$(5):HPG$_{50k}$-g-C$_{18}$(10) prepared from emulsification with SPION-free chloroform resulted predominantly in spherical structures. The scale bar represents 500 nm.

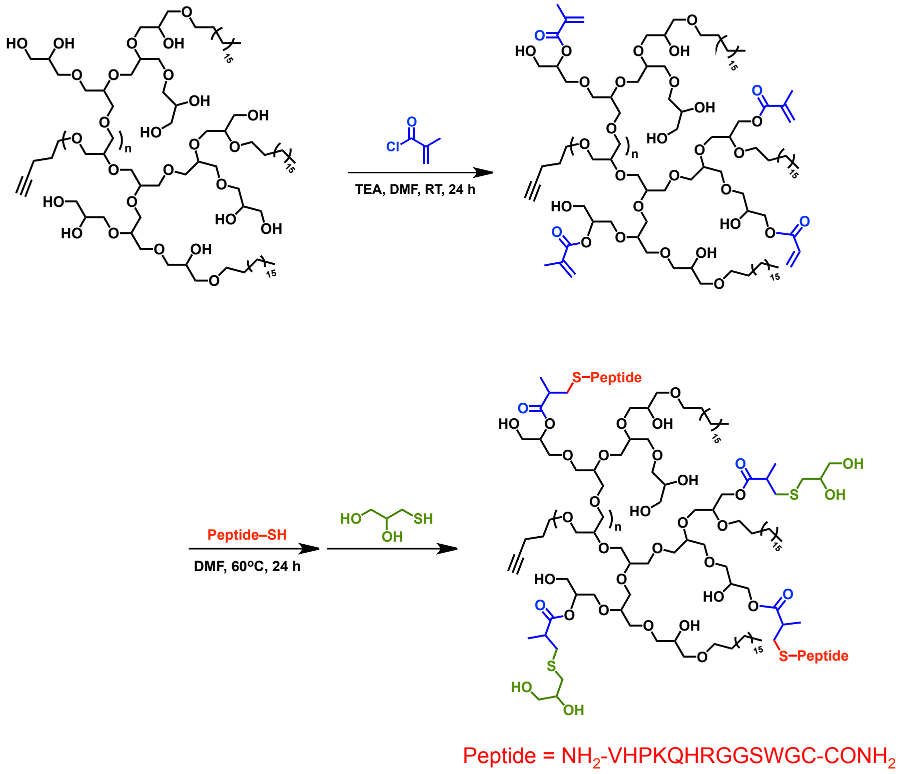

Figure 5.5 Conjugation of the VCAM-1 targeting peptide to the alkylated HPG backbone.

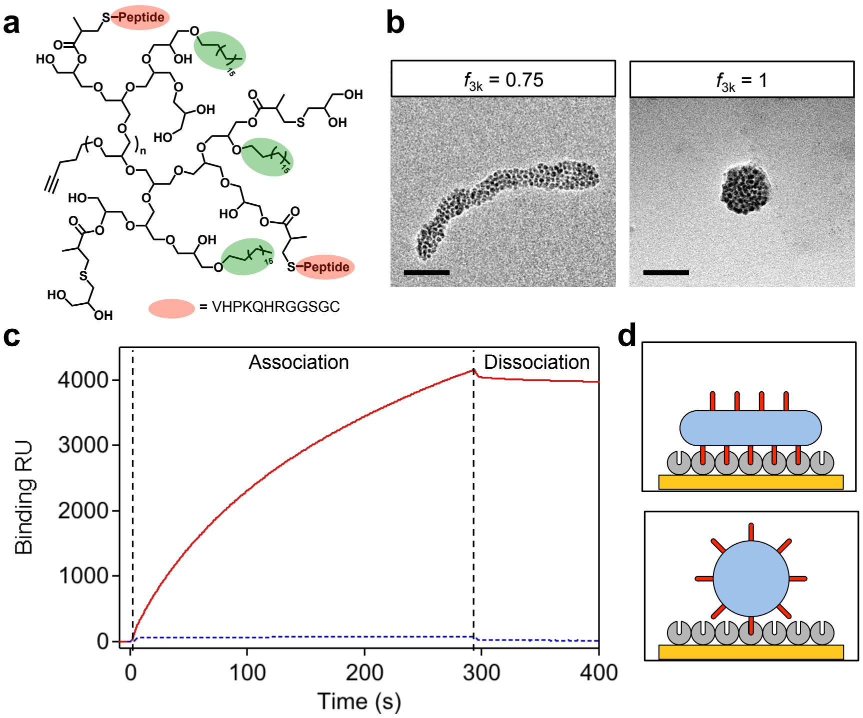

Figure 5.6 VCAM-targeting HPG-SPION clusters. (a) Example chemical structure of peptide-conjugated HPG_{3k}-g-C_{18}. (b) Addition of the peptide did not interfere with cluster formation, as $f_{3k} = 0.75$ resulted in wormlike clusters, while $f_{3k} = 1$ remained spherical. Scale bars represent 50 nm. (c) SPR kinetic binding analysis of targeted wormlike (red, solid curve) and spherical (blue, dotted curve) nanoclusters during association and dissociation with VCAM-1 receptors. (d) Schematic of differences in binding between nanocluster and substrate for wormlike and spherical clusters.

Table 5.1 Kinetic binding values for the association and dissociation between nanoclusters and VCAM-immobilized substrate as determined by SPR. Values are given per molar concentration of iron.

Morphology of targeted cluster	Association rate constant k_a ($M^{-1}s^{-1}$)	Dissociation rate constant k_d (s^{-1})	Binding constant K_A (M^{-1})
Spherical	1.02	1.32×10^{-3}	7.73×10^{2}
Wormlike	14.7	1.45×10^{-5}	1.01×10^{6}

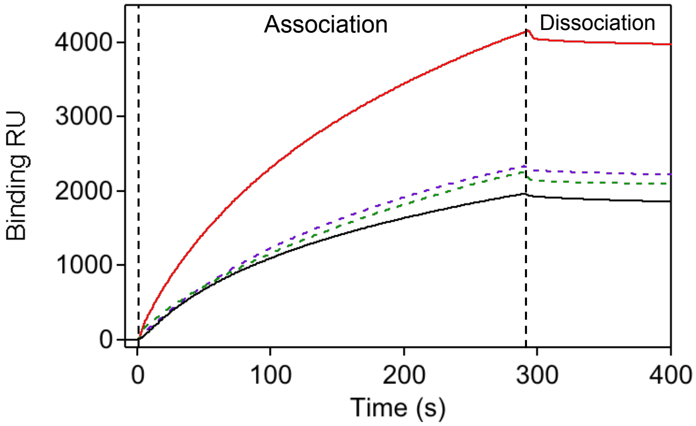

Figure 5.7 The role of targeting peptide in the binding of wormlike nanoclusters. The binding RU for targeted clusters (red, solid curve) was higher than that of non-targeted clusters (green, dotted curve). Additionally, pre-saturating VCAM-1 receptors with free peptide reduced the binding RU for targeted clusters (black, solid curve), but had minimal effect on non-targeted clusters (purple, dotted curve).

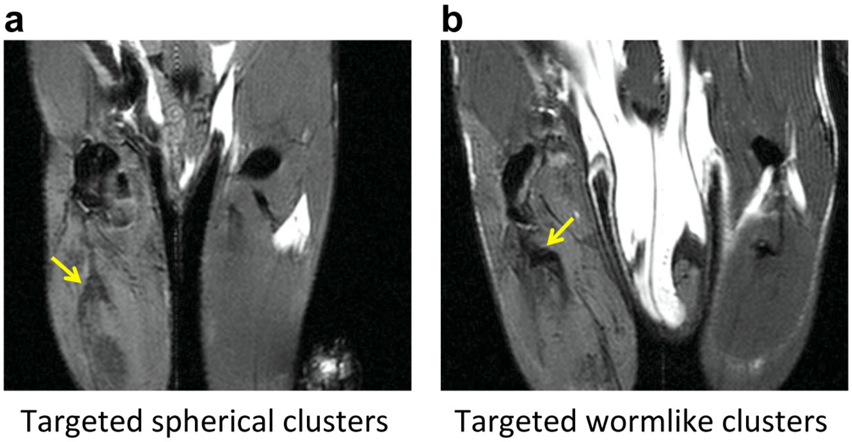

Figure 5.8 *In vivo* evaluation of targeted nanoclusters. Ischemic injury induced in the left hindlimb was highlighted with negative contrast after systemic injection of (a) targeted spherical clusters and (b) targeted wormlike clusters. The region of interest is highlighted by yellow arrows.

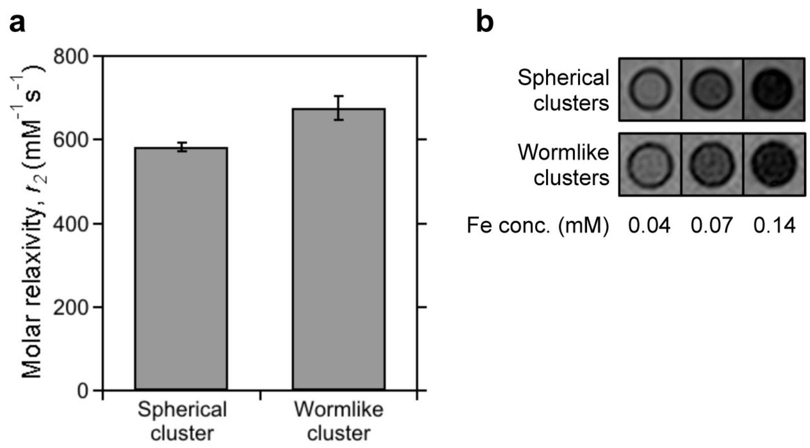

Figure 5.9 Relaxivity of SPION clusters. (a) The T_2 molar relaxivity of wormlike clusters was slightly higher than that of spherical clusters, however resultant differences in contrast capability were minimal (b). Error bars represent standard deviation of the fit parameter.

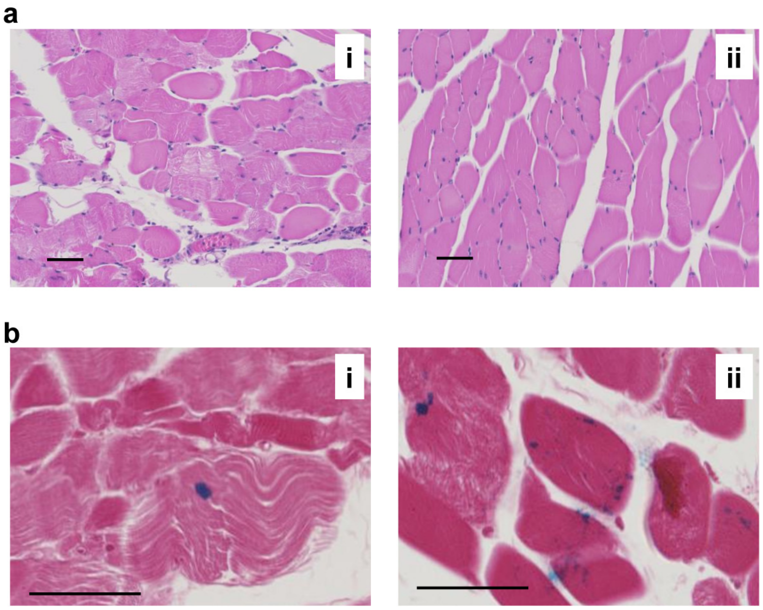

Figure 5.10 Histological analysis of the mouse hindlimb. (a) H&E staining of (i) the ischemic left hindlimb and (ii) the right hindlimb that did not receive the injury. (b) Prussian blue staining of the injured, left hindlimb for the mouse injected with (i) targeted spherical clusters and (ii) targeted wormlike clusters.

5.7 References

1. Choi, H. S.; Liu, W.; Liu, F.; Nasr, K.; Misra, P.; Bawendi, M. G.; Frangioni, J. V. Design Considerations for Tumour-Targeted Nanoparticles. *Nature Nanotech.* **2010,** *5*, 42-47.

2. Byrne, J. D.; Betancourt, T.; Brannon-Peppas, L. Active Targeting Schemes for Nanoparticle Systems in Cancer Therapeutics. *Adv. Drug Del. Rev.* **2008,** *60*, 1615-1626.

3. Yun, Y.; Cho, Y. W.; Park, K. Nanoparticles for Oral Delivery: Targeted Nanoparticles with Peptidic Ligands for Oral Protein Delivery. *Adv. Drug Del. Rev.* **2013,** *65*, 822-832.

4. Gu, F.; Zhang, L.; Teply, B. A.; Mann, N.; Wang, A.; Radovic-Moreno, A. F.; Langer, R.; Farokhzad, O. C. Precise Engineering of Targeted Nanoparticles by Using Self-Assembled Biointegrated Block Copolymers. *Proc. Natl. Acad. Sci.* **2008,** *105*, 2586-2591.

5. Davis, M. E.; Zuckerman, J. E.; Choi, C. H. J.; Seligson, D.; Tolcher, A.; Alabi, C. A.; Yen, Y.; Heidel, J. D.; Ribas, A. Evidence of RNAi in Humans from Systemically Administered siRNA via Targeted Nanoparticles. *Nature* **2010,** *464*, 1067-1070.

6. Lai, M.-H.; Jeong, J. H.; DeVolder, R. J.; Brockman, C.; Schroeder, C.; Kong, H. Ellipsoidal Polyaspartamide Polymersomes with Enhanced Cell-Targeting Ability. *Adv. Funct. Mater.* **2012,** *22*, 3239-3246.

7. Chen, J.; Clay, N. E.; Park, N.-h.; Kong, H. Non-Spherical Particles for Targeted Drug Delivery. *Chem. Eng. Sci.* **2015,** *125*, 20-24.

8. Blanazs, A.; Armes, S. P.; Ryan, A. J. Self-Assembled Block Copolymer Aggregates: From Micelles to Vesicles and Their Biological Applications. *Macromol. Rapid Commun.* **2009,** *30*, 267-277.

9. Cheng, H.; Yuan, X.; Sun, X.; Li, K.; Zhou, Y.; Yan, D. Effect of Degree of Branching on the Self-Assembly of Amphiphilic Hyperbranched Multiarm Copolymers. *Macromolecules* **2010,** *43*, 1143-1147.

10. Zhang, L.; Eisenberg, A. Multiple Morphologies of "Crew-Cut" Aggregates of Polystyrene-B-Poly(Acrylic Acid) Block Copolymers. *Science* **1995,** *268*, 1728-1731.

11. Rajagopal, K.; Mahmud, A.; Christian, D. A.; Pajerowski, J. D.; Brown, A. E. X.; Loverde, S. M.; Discher, D. E. Curvature-Coupled Hydration of Semicrystalline Polymer Amphiphiles Yields Flexible Worm Micelles but Favors Rigid Vesicles: Polycaprolactone-Based Block Copolymers. *Macromolecules* **2010,** *43*, 9736-9746.

12. Won, Y.-Y.; Davis, H. T.; Bates, F. S. Giant Wormlike Rubber Micelles. *Science* **1999,** *283*, 960-963.

13. Smith, C. E.; Shkumatov, A.; Withers, S. G.; Yang, B.; Glockner, J. F.; Misra, S.; Roy, E. J.; Wong, C.-H.; Zimmerman, S. C.; Kong, H. A Polymeric Fastener Can Easily Functionalize Liposome Surfaces with Gadolinium for Enhanced Magnetic Resonance Imaging. *ACS Nano* **2013,** *7*, 9599-9610.

14. Clay, N.; Baek, K.; Shkumatov, A.; Lai, M.-H.; Smith, C. E.; Rich, M.; Kong, H. Flow-Mediated Stem Cell Labeling with Superparamagnetic Iron Oxide Nanoparticle Clusters. *ACS Appl. Mater. Interfaces* **2013,** *5*, 10266-10273.

15. Zhu, J.; Hayward, R. C. Spontaneous Generation of Amphiphilic Block Copolymer Micelles with Multiple Morphologies through Interfacial Instabilities. *J. Am. Chem. Soc.* **2008,** *130*, 7496-7502.

16. Nahrendorf, M.; Jaffer, F. A.; Kelly, K. A.; Sosnovik, D. E.; Aikawa, E.; Libby, P.; Weissleder, R. Noninvasive Vascular Cell Adhesion Molecule-1 Imaging Identifies Inflammatory Activation of Cells in Atherosclerosis. *Circulation* **2006,** *114*, 1504-1511.

17. Ross, R. Atherosclerosis — an Inflammatory Disease. *New Engl. J. Med.* **1999,** *340*, 115-126.

18. Stenberg, E.; Persson, B.; Roos, H.; Urbaniczky, C. Quantitative Determination of Surface Concentration of Protein with Surface Plasmon Resonance Using Radiolabeled Proteins. *J. Colloid Interface Sci.* **1991,** *143*, 513-526.

19. Young, K. D. The Selective Value of Bacterial Shape. *Microbiol. Mol. Biol. Rev.* **2006,** *70*, 660-703.

20. Geng, Y.; Dalhaimer, P.; Cai, S.; Tsai, R.; Tewari, M.; Minko, T.; Discher, D. E. Shape Effects of Filaments Versus Spherical Particles in Flow and Drug Delivery. *Nature Nanotech.* **2007,** *2*, 249-255.

21. Park, J.-H.; von Maltzahn, G.; Zhang, L.; Schwartz, M. P.; Ruoslahti, E.; Bhatia, S. N.; Sailor, M. J. Magnetic Iron Oxide Nanoworms for Tumor Targeting and Imaging. *Adv. Mater.* **2008,** *20*, 1630-1635.

22. Yang, X.; Grailer, J. J.; Rowland, I. J.; Javadi, A.; Hurley, S. A.; Steeber, D. A.; Gong, S. Multifunctional SPIO/DOX-Loaded Wormlike Polymer Vesicles for Cancer Therapy and MR Imaging. *Biomaterials* **2010,** *31*, 9065-73.

23. Wang, G.; Inturi, S.; Serkova, N. J.; Merkulov, S.; McCrae, K.; Russek, S. E.; Banda, N. K.; Simberg, D. High-Relaxivity Superparamagnetic Iron Oxide Nanoworms with Decreased Immune Recognition and Long-Circulating Properties. *ACS Nano* **2014,** *8*, 12437-49.

CHAPTER 6

CONCLUSION

6.1 Summary

This thesis has described several design strategies for the improvement of MRI contrast agents. In all cases, preserving the ability of the contrast agent to interact with surrounding water molecules was imperative in enhancing molar relaxivity. For gadolinium, this was accomplished by spatially organizing the contrast agent on the surface of its nanocarrier, rather than within the interior, thus providing access to bulk water. For SPIONs, interaction with water was promoted by the hyperbranched, hydrophilic network of the polyglycerol cluster coating. Relaxivity was further enhanced through size effects. HPG was able to tune the size of SPION clusters, thus enabling relaxivity optimization within the static dephasing regime. In the case of gadolinium, conjugation to a macromolecular backbone allowed for improved contrast per dose, compared to the clinically used small molecule chelate.

The carriers described in this thesis also allowed for greater accumulation within vascular defects to further improve their diagnostic capability. Gadolinium-coated liposomes were able to highlight damaged vasculature in a murine model of hindlimb ischemia, and were retained in the renal cortex of a renal ischemia model. Similarly, HPG-SPION clusters beaconed ischemic tissue in models of hindlimb and coronary ischemia due to the EPR effect. The targetability of SPION clusters was further improved through the incorporation of targeting ligands that allowed for adhesion to sites of inflammation, and with morphogenic control to promote multivalent binding. Taken together, these efforts to enhance relaxivity and localization of MRI contrast agents have allowed for diagnostic imaging at low doses in animal models, and will contribute to sensitive imaging in the evaluation of vascular diseases.

6.2 Future Work

The materials used for the assembly of gadolinium and iron oxide could easily be extended to incorporate secondary imaging probes. For example, liposomes may be used to encapsulate an additional contrast agent, such as gold nanoparticles for computed tomography (CT), prior to coating with gadolinium. The method would allow for spatial separation of agents and orthogonal diagnosis. Similarly, HPG could easily be modified, for example with the covalent conjugation of near infrared (NIR) probes for optical imaging. Furthermore, combining gadolinium or SPIONs with radiolabels would facilitate high sensitivity PET imaging to localize areas of disease, followed by high resolution MR imaging to locally assess tissue structure. Finally, the gadolinium-coated liposomes could be used to encapsulate HPG-SPION clusters for dual T_1 and T_2 contrasted imaging.

In addition to targeted diagnosis, the probes developed in this thesis could be used for local delivery of therapeutic agents. This would allow for monitoring of accumulation and clearance of probe at target sites to non-invasively examine therapeutic outcomes and inform dosing regimens. This would also provide the opportunity for triggered delivery, in which the nanocarrier is stimulated to release its cargo locally after sufficient accumulation, as determined by diagnostic imaging. In the case of cell labeling, the fastener could be further modified to carry stimulatory factors as cargo in order to promote therapeutic secretions from the cell. Furthermore, the contrast agents themselves may have applications in treatment. Gadolinium has been investigated for its use in cancer treatment with neutron capture therapy (NCT), and the fastener-modified liposome may provide a way to target cancer cells for cellular uptake and irradiation. Similarly, iron oxide nanoparticles produce a hyperthermic effect in an alternating magnetic field to locally treat tumors, for which the targeted iron oxide clusters may be of benefit. Overall, the materials developed in this thesis are broadly applicable to many diagnostic and therapeutic applications, which remain ongoing, active areas of interest.